Physik-Department

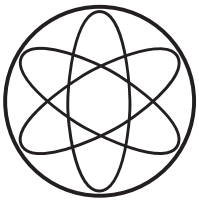

New Aspects of the MIEZE Technique and Verification of the Multi-level MIEZE Principle

Dissertation
von

Nikolas Arend

Technische Universität
München

Fakultät für Physik der Technischen Universität München
Institut E21

New Aspects of the MIEZE Technique and Verification of the Multi-level MIEZE Principle

Nikolas Arend

Vollständiger Abdruck der von der Fakultät für Physik der Technischen Universität München zur Erlangung des akademischen Grades eines

Doktors der Naturwissenschaften

genehmigten Dissertation.

Vorsitzender: Univ.-Prof. Dr. Andrzej J. Buras

Prüfer der Dissertation: 1. Univ.-Prof. Dr. Peter Böni
2. Univ.-Prof. Dr. Reiner Krücken

Die Dissertation wurde am 19. April 2007 bei der Technischen Universität München eingereicht und durch die Fakultät für Physik am 14. Juni 2007 angenommen.

Scully: „What are you going to tell him?“

Mulder: „What do you mean, what am I gonna tell him?
I'm going to tell him exactly what I saw!
What are *you* gonna tell him?“

Scully: „I'll tell him exactly what *I* saw.“

Mulder: „Now, how is that different?“

The X-files (Season 5, Episode 12)

Abstract

MIEZE (Modulation of IntEnsity by Zero Effort) and Multi-level MIEZE are variants of the Neutron Resonance Spin Echo (NRSE) technique, a neutron scattering method for the study of dynamics on an atomic scale with high energy resolution.

The objective of the dissertation was to prove the Multi-level MIEZE principle, which consists in the stacking of several single MIEZE setups to achieve a sharpening of the main peaks in the high-frequency, time-modulated signal without loss of contrast. The predicted signal form and hence the principle could be verified in measurements using a two-level Multi-MIEZE setup.

For the Multi-level MIEZE measurements at the very cold beam-line of the instrument MIRA at the research neutron source FRM-II, a complete set of NRSE instrumentation was designed and built, which will continued to be used as permanent NRSE and MIEZE measurement options. For that purpose, a new type of resonance flipper coils was conceptualized, constructed, and taken into operation.

In the theoretical part of the work, the quantum mechanical formalism of time-evolution operators was on the one hand applied to polarization theory in general, on the other hand to the MIEZE technique using a new approach, which considers the splitting in energy and momentum of the spin-up and spin-down states more consistently.

Zusammenfassung

MIEZE (Modulation of IntEnsity by Zero Effort) und Multi-level MIEZE sind Varianten der Neutronen-Resonanz-Spinecho-Technik (NRSE), eine Neutronenstreumethode zum Studium von Dynamik auf atomarer Skala mit hoher Energieauflösung.

Ziel der Dissertation war es, das Multi-level MIEZE-Prinzip zu verifizieren. Dieses besteht in der Reihenschaltung einzelner MIEZE-Stufen, um eine Verschärfung der Hauptpeaks des hochfrequenten, zeitlich modulierten Signals ohne Kontrastverlust zu erreichen. Die vorausgesagte Signalform und damit die Gültigkeit des Prinzips konnten in Messungen mittels eines zweistufigen Multi-MIEZE-Aufbaus bewiesen werden.

Für die Multi-level MIEZE-Messungen mit sehr kalten Neutronen am Instrument MIRA an der Forschungsneutronenquelle FRM-II wurde ein kompletter Satz von NRSE-Instrumentierung entwickelt und erstellt, die auch weiterhin als permanente NRSE- und MIEZE-Messoption zum Einsatz kommt. Zu diesem Zweck ist ein neuartiger Typ von Resonanz-Flip-Spulen konzeptioniert, gebaut und in Betrieb genommen worden.

Im theoretischen Teil der Arbeit wurde der quantenmechanische Formalismus der Zeitentwicklungsoperatoren zum einen angewendet auf die Theorie der Polarisation im Allgemeinen, zum anderen auf die MIEZE-Technik selbst, unter Verwendung eines neuen Ansatzes, der die Energie- und Impulsaufspaltung der Spin-up und Spin-down Zustände konsequenter berücksichtigt.

Contents

List of Figures

List of Tables

List of Abbreviations

AFM	Atomic Force Microscope
BEM	Boundary Element Method
EDM	Electrical Discharge Machining
ESR	Electron Spin Resonance
FEM	Finite Element Method
FWHM	Full Width Half Maximum
GRP	Glass-fiber Reinforced Plastic
HF	High Frequency
HV	High Voltage
MIEZE	Modulation of IntEnsity by Zero Effort
NMR	Nuclear Magnetic Resonance
NRSE	Neutron Resonance Spin Echo
NSE	Neutron Spin Echo
PVC	Polyvinyl Chloride
RF	Radio Frequency
SANS	Small Angle Neutron Scattering
SERGIS	Spin Echo Resolved Grazing Incidence Scattering
SESANS	Spin Echo Small Angle Neutron Scattering
TAS	Triple Axis Spectrometer
TOF	Time Of Flight

Preface

Neutron physics and the field of neutron scattering have established excellent tools and methods to investigate matter on an atomic scale. The unique properties of the neutron – its electrical neutrality, the spin, and the fact that its matter wavelength corresponds to inter-atomic distances – distinguish it as a microscopic probe for structure and dynamics.

One of the polarized neutron scattering techniques that is ideal to investigate inelastic or quasi-elastic interactions for processes taking place on the ns time scale is Neutron Spin Echo (NSE), introduced by Mezei in 1972 [1]. The high energy resolution it provides is typically in the μeV to neV range for slow neutrons and does not, as opposed to other types of spectrometers, depend on the spectrum of the incident beam.

In NSE, the information about the scattering process and the transferred amount of energy in the sample is coded in the spin of the neutron. By comparing the Larmor precession angles of a polarized neutron beam in strong, homogeneous magnetic fields before and after the interaction with a sample, information about the intermediary scattering function can be obtained by investigating the decrease in polarization caused by the transfer of energy. This opens the possibility to study a large range of systems with slow dynamics. Examples are chemical and biological systems, like colloids, micro-emulsions, polymers, and glass formers.

In 1987 Gähler and Golub [2] proposed Neutron Resonance Spin Echo (NRSE), the principle of which is related to techniques like Nuclear Magnetic Resonance (NMR) or Electron Spin Resonance (ESR). NRSE replaces the long constant fields of NSE by zero field regions enclosed by two short resonance spin flippers with sharp field boundaries, containing a homogeneous DC field and a perpendicular, resonantly rotating RF field. The spin encoding in this case is not achieved by Larmor precession of the neutron spins, but by the rotation of the RF fields, which work as an external clock.

Besides conventional spin echo spectrometry, NRSE opened possibilites for new measurement techniques. Thanks to the compact design of the resonance flipper coils, they can be tilted with respect to the neutron beam direction up to angles of 45° and above. This, for example, allows for measuring phonon line widths or other dispersive excitations with high energy resolution by combining a triple axis spectrometer (TAS) with spin echo. Such an instrument, TRISP, has been recently taken into operation at the neutron source FRM-II.

The work at hand is focusing on the NRSE variants MIEZE (Modulation of IntEnsity by Zero Effort) and Multi-level MIEZE [3]. MIEZE is a type of resonance spin echo instrument that uses only one arm of an NRSE spectrometer. A high frequency, time-dependent sinusoidal signal at the detector is achieved by running the two resonance flippers at different frequencies. The contrast of the sinusoidal signal can be used, analogue to the polarization in N(R)SE, for quasi-elastic spin echo measurements with high energy resolution. Besides technical restrictions that mainly concern the detector system prerequisites (thickness and time resolution of the

detector), MIEZE also provides a huge advantage: the signal modulation is achieved before the sample. That makes the measurement insensitive to depolarization effects at the sample region, which does not need to be magnetically shielded. This offers the freedom to design and configure the sample environments to include measurents with strong magnetic fields, high and low temperature, ferromagnetic samples, or long and multi-angle scattering geometries. In short: conditions that are difficult (or in some cases impossible) to realize with conventional NSE or NRSE.

A Multi-level MIEZE (or Multi-MIEZE) instrument consists of several serially stacked single MIEZE setups with a common detector position. It was predicted [3] that by doing so, the width of the main pulses in the high frequency signal can be significantly narrowed. This would make Multi-MIEZE a high resolution TOF-spectrometer with a large dynamic range. Other conceivable applications for a Multi-MIEZE signal could be in neutron interferometry and fundamental physics.

The objectives of this thesis can be divided into four parts: i) The experimental verification of the Multi-MIEZE principle (section 3.4), ii) theoretical work on the MIEZE and Multi-MIEZE techniques (chapter 1), iii) development of a novel type of resonance spin flippers as well as NRSE instrumentation for the instrument MIRA (section 2.2, chapter 2), and iv) first MIEZE measurements at the instrument MIRA demonstrating the potentials of MIEZE (section 3.5).

Although the MIEZE technique has been covered and experimentally tested in previous works and theses (e.g. [4, 5, 6]), no dedicated instrument exists. In the near future, the instruments MIRA and RESEDA at the FRM-II will be two of the very few spectrometers that are equipped with a MIEZE option, and will make use of it on a regular basis for quasi-elastic or wide-angle scattering measurements. Otherwise the acceptance of the features which MIEZE can provide seems very low, and to our knowledge the inclusion of a MIEZE option at other neutron scattering instruments (e.g. small angle scattering) was seldomly considered. We hope that with this thesis we can make a small contribution to change that situation and put the strengths as well as the limitations of the MIEZE technique in perspective.

1

Theoretical Introduction to Neutron Resonance Spin Echo and MIEZE

The Neutron Spin Echo (NSE) technique is a neutron scattering spectroscopy method and was introduced by F. Mezei in 1972 [1]. It allows for measurements with high energy resolution and investigations of large domains in time and space in condensed matter physics. The area of applications ranges from dynamics of glasses, polymers, biological macromolecules, colloids and micro-emulsions to investigations of magnetic properties and excitations, e.g. ferro- and antiferromagnetism or superconductivity.

A variant of NSE is the Neutron Resonance Spin Echo (NRSE) technique, which replaces the long constant magnetic fields used in NSE by so-called pseudo fields, created by pairs of radio frequency spin flipping coils. This technique was proposed by R. Gähler und R. Golub in 1987 [2]. Technically easier to implement, NRSE allows for high resolutions and opened new possibilities for measurement techniques.

The MIEZE (Modulation of IntEnsity by Zero Effort) spectrometer, which this work is based on, is a variant of NRSE. As we will see later, it has a close relation to interferometry.

This chapter shall introduce the underlying theory of the three above-mentioned spectrometer types. We start with a treatment of the concept of neutron polarization, since it is inextricably linked with every flavor of Neutron Spin Echo techniques. Then we present the basic working principle of NSE and NRSE, followed by MIEZE and Multi-level MIEZE (or short: Multi-MIEZE). Since the emphasis of the work at hand lies on the latter techniques, the theoretical treatment will in most cases focus on the quantum mechanical picture.

1.1 Polarization Theory

The neutron is a spin-$\frac{1}{2}$ particle with a magnetic moment $\mu = -0.96623640 \cdot 10^{-26}$ J/T, which makes it sensitive to magnetic fields and structures. Being also electrically neutral, it proved well suited as a probe on the atomic scale.
Neutron Spin Echo techniques are based on the usage and analysis of a polarized neutron beam. This section provides the definition of neutron polarization and outlines the concept as well as the needed mathematical tools. A more elaborate derivation can be found in [7] and various textbooks, here we shall only present the results crucial for the rest of the work.

Vividly speaking, a neutron beam is polarized with respect to a chosen direction, when

the neutron spins have a preferred orientation. The polarization $\boldsymbol{P}$ is a 3-dimensional vector

$$\boldsymbol{P} = (P_x, P_y, P_z) \; . \tag{1.1}$$

and reflects the direction and the degree of that orientation.

On the way to a formal representation, we find that we have to distinguish between the polarization of a pure spin state (single neutron or perfectly polarized beam) and that of a mixed state (partially polarized beam).

The above-mentioned implicates that the polarization is a beam property and hence a statistical quantity of all neutrons in the beam. In section 1.1.2 we will therefore use the density matrix, also referred to as density operator or statistical operator, to describe the incompletely prepared quantum mechanical state of a partially polarized neutron beam.

1.1.1 Spinor Notation of the Neutron Spin

In quantum mechanics the observable of the neutron spin is represented by the spin operator

$$\boldsymbol{S} = (S_x, S_y, S_z) \; . \tag{1.2}$$

With respect to an arbitrary unit vector $\boldsymbol{e}$ it possesses the eigenvalues $\pm\hbar/2$. Usually $\boldsymbol{e}_z$ is chosen as quantization axis, which results in the eigenvalue equation

$$S_z \begin{pmatrix} |\uparrow\rangle \\ |\downarrow\rangle \end{pmatrix} = \frac{\hbar}{2} \begin{pmatrix} +|\uparrow\rangle \\ -|\downarrow\rangle \end{pmatrix} \; , \tag{1.3}$$

with $|\uparrow\rangle$, $|\downarrow\rangle$ representing spin-up and spin-down.
The quantum mechanical state of a neutron can be written as a two-component spinor

$$|\boldsymbol{\psi}(\boldsymbol{r})\rangle = \begin{pmatrix} \psi_\uparrow(\boldsymbol{r}) \\ \psi_\downarrow(\boldsymbol{r}) \end{pmatrix} . \tag{1.4}$$

We write spin-up and spin-down as

$$|\uparrow\rangle = \begin{pmatrix} 1 \\ 0 \end{pmatrix} = \chi_+ \tag{1.5}$$

$$|\downarrow\rangle = \begin{pmatrix} 0 \\ 1 \end{pmatrix} = \chi_- \; , \tag{1.6}$$

their Hermitian adjoint states are

$$\langle\uparrow| = (1, 0) = \chi_+^\dagger \tag{1.7}$$

$$\langle\downarrow| = (0, 1) = \chi_-^\dagger \; . \tag{1.8}$$

With the above, a general spin state takes the form

$$\chi = c_+\chi_+ + c_-\chi_- = \begin{pmatrix} c_+ \\ c_- \end{pmatrix} \; , \tag{1.9}$$

with c_+ and c_- being complex coefficients. They must satisfy the normalization condition $|c_+|^2 + |c_-|^2 = 1$, since the neutron must be in either spin-up or spin-down state. This definition allows also for the representation of partially polarized spin states.

In order to obtain an expression for the relation between the vector $\boldsymbol{S}$ and the spinor χ, which both describe the spin – the first in Cartesian, the latter in spinor space – we use the well-known Pauli matrices

$$\boldsymbol{\sigma} = (\sigma_\mathrm{x},\, \sigma_\mathrm{y},\, \sigma_\mathrm{z}) \tag{1.10}$$

$$\sigma_\mathrm{z} = \begin{pmatrix} 1 & 0 \\ 0 & -1 \end{pmatrix},\ \sigma_\mathrm{x} = \begin{pmatrix} 0 & 1 \\ 1 & 0 \end{pmatrix},\ \sigma_\mathrm{y} = \begin{pmatrix} 0 & -i \\ i & 0 \end{pmatrix}\ , \tag{1.11}$$

which have the eigenvectors

$$\chi_+^\mathrm{z} = \chi_+ = \begin{pmatrix} 1 \\ 0 \end{pmatrix} \qquad \chi_-^\mathrm{z} = \chi_- = \begin{pmatrix} 0 \\ 1 \end{pmatrix} \tag{1.12}$$

$$\chi_+^\mathrm{x} = \frac{1}{\sqrt{2}} \begin{pmatrix} 1 \\ 1 \end{pmatrix} = \frac{1}{\sqrt{2}} (\chi_+ + \chi_-) \qquad \chi_-^\mathrm{x} = \frac{1}{\sqrt{2}} \begin{pmatrix} 1 \\ -1 \end{pmatrix} = \frac{1}{\sqrt{2}} (\chi_+ - \chi_-) \tag{1.13}$$

$$\chi_+^\mathrm{y} = \frac{1}{\sqrt{2}} \begin{pmatrix} 1 \\ i \end{pmatrix} = \frac{1}{\sqrt{2}} (\chi_+ + i\chi_-) \qquad \chi_-^\mathrm{y} = \frac{1}{\sqrt{2}} \begin{pmatrix} i \\ 1 \end{pmatrix} = \frac{1}{\sqrt{2}} (i\chi_+ + \chi_-)\ . \tag{1.14}$$

associated with the eigenvalues ± 1. The spin operator can then be written as

$$\boldsymbol{S} = \frac{\hbar}{2} \boldsymbol{\sigma}\ . \tag{1.15}$$

The expectation value of a general spin state with respect to the three quantization axes reflects its polarization:

$$\begin{aligned} \boldsymbol{P} \equiv \langle \boldsymbol{\sigma} \rangle &= \left(\langle \chi | \, \sigma_\mathrm{x} \, | \chi \rangle \, , \langle \chi | \, \sigma_\mathrm{y} \, | \chi \rangle \, , \langle \chi | \, \sigma_\mathrm{z} \, | \chi \rangle \right) \\ &= (\chi^\dagger \sigma_\mathrm{x} \chi, \chi^\dagger \sigma_\mathrm{y} \chi, \chi^\dagger \sigma_\mathrm{z} \chi) \\ &= \frac{2}{\hbar} \langle \boldsymbol{S} \rangle\ . \end{aligned} \tag{1.16}$$

We now introduce spherical coordinates φ and ϑ as shown in Fig. 1.1. The spinor χ, expressed by φ and ϑ, takes the form

$$\chi = \begin{pmatrix} \cos\frac{\vartheta}{2}\, \mathrm{e}^{-i\frac{\varphi}{2}} \\ \sin\frac{\vartheta}{2}\, \mathrm{e}^{i\frac{\varphi}{2}} \end{pmatrix}\ . \tag{1.17}$$

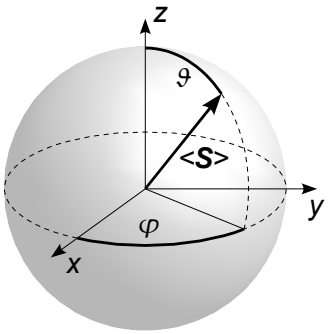

Figure 1.1: Definition of spherical coordinates of the spin direction.

By applying it to Eq. (1.16) we obtain for the polarization

$$\boldsymbol{P} = \left(\langle \sigma_\mathrm{x} \rangle \, , \langle \sigma_\mathrm{y} \rangle \, , \langle \sigma_\mathrm{z} \rangle \right) = (\cos\varphi \sin\vartheta, \sin\varphi \sin\vartheta, \cos\vartheta)\ .$$

This link between spinor space and the three-dimensional spin vector in spherical and Cartesian coordinates will enable us later to describe the classical view of the precession of a spin in a magnetic field in a rather demonstrative way.

Please note that Eqs. (1.16) and (1.18) represent the polarization of a pure spin state, which becomes obvious when we calculate the absolute value

$$|\boldsymbol{P}|^2 = \cos^2\varphi \sin^2\vartheta + \sin^2\varphi \sin^2\vartheta + \cos^2\vartheta = 1\ . \tag{1.18}$$

1.1.2 The Density Matrix Formalism

Since all polarization devices will only be able to produce a partially polarized beam in practice, we need to have means to describe an incomplete polarization. The spin state of the beam is a mixed state and we have to find an expression for $\boldsymbol{P}$ to reflect that.
A powerful tool to describe the expectation value of an operator $\boldsymbol{A}$ in a mixed state – and hence a statistical physical system such as a neutron beam – is the density matrix ϱ. The description of pure states is then a special case in the density matrix formalism.

We assume a physical system that consists of an ensemble of elements in different states. The probability to find an element i in state $|\psi_i\rangle$ shall be p_i. An observable A then has the average value

$$\langle A\rangle = \sum_i p_i \langle\psi_i| A |\psi_i\rangle \ . \tag{1.19}$$

This can also be expressed by the density matrix

$$\varrho = \sum_i p_i |\psi_i\rangle \langle\psi_i| \ , \tag{1.20}$$

and for the average value we find

$$\langle A\rangle = \mathrm{Tr}(\varrho A) \ . \tag{1.21}$$

Here it becomes obvious why the density matrix is such a convenient tool. The Trace Tr() does not depend on the basis representing the system, which can be chosen according to the problem.

For a pure ensemble all its elements are in the same state. The properties of the density matrix depend on which kind of system (pure or mixed) it describes:

Pure states		Mixed states	
$\mathrm{Tr}\varrho = 1$	(1.22)	$\mathrm{Tr}\varrho = 1$	(1.25)
$\varrho^2 = \varrho$	(1.23)	$\varrho^2 \neq \varrho$	(1.26)
$\varrho^\dagger = \varrho$	(1.24)	$\mathrm{Tr}\varrho^2 < 1$ (if $p_i \neq 0$ for more than one i)	(1.27)
		$\varrho^\dagger = \varrho$.	(1.28)

For low-dimensional state spaces like spin-$\frac{1}{2}$ systems such as a neutron beam, things tend to be relatively simple. In that case, ϱ is the dyadic product of the general spin state Eq. (1.9)

$$\varrho = |\chi\rangle\langle\chi| = \chi\chi^\dagger \tag{1.29}$$

$$= \begin{pmatrix} c_+ \\ c_- \end{pmatrix} (c_+^*, c_-^*) = \begin{pmatrix} |c_+|^2 & c_-^* c_+ \\ c_+^* c_- & |c_-|^2 \end{pmatrix} \tag{1.30}$$

$$= \frac{1}{2}\left(\mathbb{1} + \boldsymbol{P}\cdot\boldsymbol{\sigma}\right) \ . \tag{1.31}$$

Eq. (1.31) is the most general form for ϱ in spin space. Using Eqs. (1.11) and (1.18) we can

further write

$$\varrho = \frac{1}{2}\begin{pmatrix} 1+P_z & P_x - iP_y \\ P_x + iP_y & 1-P_z \end{pmatrix} \tag{1.32}$$

$$= \frac{1}{2}\left(\mathbb{1} + \begin{pmatrix} \cos\vartheta & \sin\vartheta\, e^{-i\varphi} \\ \sin\vartheta\, e^{i\varphi} & -\cos\vartheta \end{pmatrix}\right) . \tag{1.33}$$

Eqs. (1.26) and (1.27) let us decide whether a given ϱ represents a pure or a mixed state:

$$\varrho^2 = \frac{1}{2}\left(\frac{1+P^2}{2}\,\mathbb{1} + \boldsymbol{\sigma}\cdot\boldsymbol{P}\right) . \tag{1.34}$$

So we have a pure state for $|\boldsymbol{P}| = 1$. As mentioned above, a neutron beam in practice will always be an ensemble of mixed states, which means $|\boldsymbol{P}|$ will be < 1.

If we further let $\boldsymbol{P}$ point in z-direction, P_z reflects the degree of polarization of the beam and we have $0 \leq |P_z| < 1$.

1.1.3 Rotation of the Polarization Vector in Space

In order to be able to describe the interaction of the polarization vector with magnetic fields, we will now sketch the mathematical rotation of $\boldsymbol{P}$ around an arbitrary axis.

We will rotate a general spin state χ in spinor space and derive $\boldsymbol{P}$ from that by applying Eq. (1.16). Let $\boldsymbol{n}$ be a unitary vector defining the rotation axis and ω the rotation angle. Naturally, we use spherical coordinates as defined in Fig. 1.1:

$$\boldsymbol{n} = (\cos\varphi\sin\vartheta,\ \sin\varphi\sin\vartheta,\ \cos\vartheta) . \tag{1.35}$$

The rotation matrix, which turns χ into $\tilde{\chi}$, reads

$$\exp\left(i\,\frac{\omega}{2}\,\boldsymbol{n}\cdot\boldsymbol{\sigma}\right) = \mathbb{1}\cos\frac{\omega}{2} + i\sin\frac{\omega}{2}\,\boldsymbol{n}\cdot\boldsymbol{\sigma} \tag{1.36}$$

$$= \mathbb{1}\cos\frac{\omega}{2} + i\sin\frac{\omega}{2}\begin{pmatrix} \cos\vartheta & \sin\vartheta\, e^{-i\varphi} \\ \sin\vartheta\, e^{i\varphi} & -\cos\vartheta \end{pmatrix} . \tag{1.37}$$

For the polarization vector, using Eq. (1.16), one obtains

$$\tilde{\boldsymbol{P}} = \begin{pmatrix} \tilde{P}_x \\ \tilde{P}_y \\ \tilde{P}_z \end{pmatrix}$$

$$= \begin{pmatrix} \sin^2\frac{\omega}{2}\,\sin^2\vartheta\,\cos 2\varphi - \\ \sin^2\frac{\omega}{2}\,\cos^2\vartheta + \cos^2\frac{\omega}{2} \end{pmatrix} \quad \begin{pmatrix} \sin^2\frac{\omega}{2}\,\sin^2\vartheta\,\sin 2\varphi + \\ \sin^2\omega\,\cos\vartheta \end{pmatrix} \quad \begin{pmatrix} \sin^2\frac{\omega}{2}\,\sin 2\vartheta\,\cos\varphi - \\ \sin\omega\,\sin\vartheta\,\sin\varphi \end{pmatrix}$$

$$\begin{pmatrix} \sin^2\frac{\omega}{2}\,\sin^2\vartheta\,\sin 2\varphi - \\ \sin\omega\,\cos\vartheta \end{pmatrix} \quad \begin{pmatrix} -\sin^2\frac{\omega}{2}\,\sin^2\vartheta\,\cos 2\varphi + \\ \cos^2\frac{\omega}{2} - \sin^2\frac{\omega}{2}\,\cos^2\vartheta \end{pmatrix} \quad \begin{pmatrix} \sin^2\frac{\omega}{2}\,\sin 2\vartheta\,\sin\varphi + \\ \sin\omega\,\sin\vartheta\,\cos\varphi \end{pmatrix}$$

$$\begin{pmatrix} \sin^2\frac{\omega}{2}\,\sin 2\vartheta\,\cos\varphi + \\ \sin\omega\,\sin\vartheta\,\sin\varphi \end{pmatrix} \quad \begin{pmatrix} \sin^2\frac{\omega}{2}\,\sin 2\vartheta\,\sin\varphi - \\ \sin\omega\,\sin\vartheta\,\cos\varphi \end{pmatrix} \quad \begin{pmatrix} \sin^2\frac{\omega}{2}\,\cos 2\vartheta + \\ \cos^2\frac{\omega}{2} \end{pmatrix} \begin{pmatrix} P_x \\ P_y \\ P_z \end{pmatrix} . \tag{1.38}$$

The most commonly used special cases will be rotations around the axes of the coordinate system. Spin state and polarization vector after a rotation around the x axis $\boldsymbol{n} = (1, 0, 0)$ with

$\varphi = 0$ and $\vartheta = \pi/2$ become

$$\tilde{\chi} = \begin{pmatrix} \cos\frac{\omega}{2} & i\sin\frac{\omega}{2} \\ i\sin\frac{\omega}{2} & \cos\frac{\omega}{2} \end{pmatrix} \chi \,, \tag{1.39}$$

$$\tilde{\boldsymbol{P}} = \begin{pmatrix} 1 & 0 & 0 \\ 0 & \cos\omega & \sin\omega \\ 0 & -\sin\omega & \cos\omega \end{pmatrix} \boldsymbol{P} \tag{1.40}$$

For the y axis ($\varphi = \vartheta = \pi/2$) we have

$$\tilde{\chi} = \begin{pmatrix} \cos\frac{\omega}{2} & \sin\frac{\omega}{2} \\ -\sin\frac{\omega}{2} & \cos\frac{\omega}{2} \end{pmatrix} \chi \,, \tag{1.41}$$

$$\tilde{\boldsymbol{P}} = \begin{pmatrix} \cos\omega & 0 & -\sin\omega \\ 0 & 1 & 0 \\ \sin\omega & 0 & \cos\omega \end{pmatrix} \boldsymbol{P} \,, \tag{1.42}$$

and a rotation around z ($\vartheta = 0$) gives

$$\tilde{\chi} = \begin{pmatrix} \mathrm{e}^{i\frac{\omega}{2}} & 0 \\ 0 & \mathrm{e}^{-i\frac{\omega}{2}} \end{pmatrix} \chi \,, \tag{1.43}$$

$$\tilde{\boldsymbol{P}} = \begin{pmatrix} \cos\omega & \sin\omega & 0 \\ -\sin\omega & \cos\omega & 0 \\ 0 & 0 & 1 \end{pmatrix} \boldsymbol{P} \,. \tag{1.44}$$

1.1.4 Time Dependence of the Polarization in Magnetic Fields

MIEZE and NRSE experiments utilize several kinds of magnetic fields, created by different types of coils, in order to control, preserve or modify the beam polarization. Some of the fields are homogeneous and static (e.g. B_0 field inside an NRSE coil or guide fields), some static but inhomogeneous (coupling coils) and others time-dependent (rotating RF field inside NRSE coils). That means we need mathematical tools to describe the evolution of the polarization in each of those fields.

The most general case is the description of a polychromatic beam represented by a mixed spin state (i.e. $|\boldsymbol{P}|^2 < 1$) that travels through a time-dependent, inhomogeneous field region.

The time evolution of an ensemble of spin states entering a potential (in our case a magnetic field region) is described by the equation of motion of the density operator

$$i\hbar \frac{\partial \varrho}{\partial t} = [\mathcal{H}, \varrho] \,, \tag{1.45}$$

where $\mathcal{H}$ is the Hamilton operator of the system. We will describe the time-dependence of the density operator $\varrho(t)$ (representing either a pure or mixed state) using a time-evolution operator $U(t, t_0)$:

$$\varrho(t) = U(t, t_0)\, \varrho(t_0)\, U^\dagger(t, t_0) \,. \tag{1.46}$$

This operator satisfies the Schrödinger equation

$$i\hbar \frac{\partial U(t, t_0)}{\partial t} = \mathcal{H}\, U(t, t_0) \,, \tag{1.47}$$

with the boundary condition $U(t = t_0) = \mathbb{1}$. We will first sketch a solution for Eqs. (1.45), (1.46) and (1.47) and then dicuss the relevant special cases in the following sections.

The Hamiltonian for a neutron beam in a magnetic field reads

$$\begin{aligned}\mathcal{H} &= -\frac{\hbar^2}{2m}\nabla^2 - \mu\boldsymbol{\sigma}\boldsymbol{B}(\boldsymbol{r},t) \\ &= -\frac{\hbar^2}{2m}\nabla^2 + \frac{\hbar}{2}\gamma\,\boldsymbol{\sigma}\boldsymbol{B}(\boldsymbol{r},t)\ .\end{aligned} \tag{1.48}$$

with $\mu = -0.96623640 \cdot 10^{-26}$ J/T being the magnetic moment and $\gamma = 1.8325 \cdot 10^{8}$ $\mathrm{s^{-1}T^{-1}}$ the gyromagnetic ratio of the neutron.

The magnetic fields we will investigate – and which in principle cover all field configurations we have in the experiment – are of the form

$$\begin{aligned}\boldsymbol{B}(\boldsymbol{r},t) &= \boldsymbol{B}_0 + \boldsymbol{B}_1(t) \\ &= \begin{pmatrix}0\\0\\B_0\end{pmatrix} + \begin{pmatrix}B_{1\mathrm{R}}\cos(\omega t-\varphi) + B_{1\mathrm{O}}\cos(\omega t-\varphi)\\ B_{1\mathrm{R}}\sin(\omega t-\varphi) - B_{1\mathrm{O}}\sin(\omega t-\varphi)\\ 0\end{pmatrix}\end{aligned} \tag{1.49}$$

$$\boldsymbol{B}_2(\boldsymbol{r}) = \begin{pmatrix}0\\ B_2\sin\alpha(\boldsymbol{r},\boldsymbol{r}_0)\\ B_2\cos\alpha(\boldsymbol{r},\boldsymbol{r}_0)\end{pmatrix} \tag{1.50}$$

$\boldsymbol{B_0}$ is static and homogeneous, pointing in z-direction. $\boldsymbol{B_1}$ is time-dependent and rotating (or oscillating) in the x-y-plane. $B_{1\mathrm{R}}$ and $B_{1\mathrm{O}}$ (the indices stand for „Resonance“ and „Off-resonance“, respectively) denote the components of two counter-rotating fields. Since a rotating magnetic field is implementable only with considerable effort, oscillating fields are used in NRSE flippers. Those can be split into two counter-rotating components. For $B_{1\mathrm{R}} = B_{1\mathrm{O}}$, $\boldsymbol{B_1}$ describes a linearly oscillating, for $B_{1\mathrm{O}} = 0$ a rotating field. φ determines the initial phase of the field vector at $t = 0$ with respect to the direction of motion.

Together, $\boldsymbol{B_0}$ and $\boldsymbol{B_1}$ represent a magnetic field the way it is implemented in an NRSE π-flipper.

$\boldsymbol{B_2}$ finally is time-independent but spatially rotating in the y-z-plane, like fields produced by coupling coils (s. section 2.4). For the position-dependent tilting angle $\alpha(\boldsymbol{r},\boldsymbol{r_0})$ we choose the form

$$\alpha(\boldsymbol{r},\boldsymbol{r}_0) = \alpha(x,x_0) = \begin{cases}\alpha_0,\ \forall\ x \text{ with } 0 \le x < x_0\\ \dfrac{\alpha_{\mathrm{L_{cc}}}\cdot(x-x_0)}{L_{\mathrm{cc}}} + \alpha_0,\ \forall\ x \text{ with } x_0 \le x \le x_0 + L_{\mathrm{cc}}\end{cases}, \tag{1.51}$$

for x values in [0, $x_0 + L_{\mathrm{cc}}$]. L_{cc} is a characteristic length over which the field is spatially rotated (or actually spans) and $\alpha_{\mathrm{L_{cc}}}$ the corresponding desired rotation angle. Both are device-specific constants, the abbreviation “cc” stands for “coupling coil”. α shall be measured between the field vector and the z-axis, α_0 defines the initial orientation.

Eq. (1.47) can be formally integrated, yielding a general solution for the time-evolution operator and an explicitely time-dependent Hamilton operator:

$$U(t,t_0) = \mathcal{T}\exp\left(-\frac{i}{\hbar}\int_{t_0}^{t}\mathcal{H}(t')\,dt'\right) \quad . \tag{1.52}$$

$\mathcal{T}$ is the Dyson time-ordering operator (s. various textbooks, e.g. [8, 9, 10]), which is required since the Hamiltonians $\mathcal{H}(t')$ do not neccessarily commute with each other for different times.

If the Hamiltonian is not explicitely time-dependent, Eq. (1.52) takes on a much simpler form

$$U_0(t,t_0) = \exp\left(-\frac{i}{\hbar}\,\mathcal{H}_0\,(t-t_0)\right) \quad . \tag{1.53}$$

We will discuss three different cases, i.e. three magnetic field configurations:

1.1.4.1 The Polarization in a Resonance Flipper

The case $\boldsymbol{B} = \boldsymbol{B}_0 + \boldsymbol{B}_1$ reflects the situation in a resonance flipper coil. The structure of the Hamiltonian representing the system is such that it has a free part and a time-dependent perturbation. Thus, changing into the Dirac or interaction picture will be convenient to obtain a solution.

In this picture, indicated by the index 'D', the time-dependence is distributed on both operators and states and they have – with respect to the Schrödinger picture – the representation

$$|\psi_\mathsf{D},t\rangle = U_0(t_0,t)\,|\psi,t\rangle = \mathrm{e}^{\frac{i}{\hbar}\mathcal{H}_0(t-t_0)}\;|\psi,t\rangle \tag{1.54}$$

$$= U_\mathsf{D}(t,t')\,|\psi_\mathsf{D},t'\rangle \tag{1.55}$$

$$U_\mathsf{D}(t,t') = U_0^+(t,t_0)\,U(t,t')U_0(t',t_0) \tag{1.56}$$

$$= \mathrm{e}^{\frac{i}{\hbar}\mathcal{H}_0(t-t_0)}\;U(t,t')\;\mathrm{e}^{-\frac{i}{\hbar}\mathcal{H}_0(t'-t_0)} \tag{1.57}$$

$$\mathcal{H}_\mathsf{D}(t) = \mathrm{e}^{\frac{i}{\hbar}\mathcal{H}_0(t-t_0)}\;\mathcal{H}(t)\;\mathrm{e}^{-\frac{i}{\hbar}\mathcal{H}_0(t-t_0)}\;. \tag{1.58}$$

At time t_0 we define Schrödinger and Heisenberg states to be equal, t' and t are the points in time between which the time-evolution of the respective state is considered.

The approach to solve the Schrödinger equation (1.47) of the time-evolution operator is to find a representation for the Hamiltonian Eq. (1.48) in which its explicit time-dependence is gone, then find a solution and transform it back into the laboratory system.

For the time being we will assume $\boldsymbol{B_1}(t)$ to be a rotating field, i.e. $B_{1\mathsf{O}} = 0$ and $B_{1\mathsf{R}} = B_1$. The results for the slightly more complicated case of an arbitrarily polarized field $\boldsymbol{B_1}$ will follow later.

As mentioned above, we split up the Hamiltonian $\mathcal{H}$ from Eq. (1.48) into a free and a

time-dependent part, the latter representing the perturbation:

$$\begin{aligned}\mathcal{H} &= \mathcal{H}_0 + \mathcal{H}_1(t) \\ &= \underbrace{-\frac{\hbar^2}{2m}\nabla^2 + \frac{\hbar}{2}\begin{pmatrix}\omega & 0\\ 0 & -\omega\end{pmatrix}}_{\mathcal{H}_0^{\text{rot}}} + \underbrace{\frac{\hbar}{2}\begin{pmatrix}\gamma B_0 - \omega & \gamma B_1\, \mathrm{e}^{-i(\omega t-\varphi)}\\ \gamma B_1\, \mathrm{e}^{i(\omega t-\varphi)} & -(\gamma B_0 - \omega)\end{pmatrix}}_{\mathcal{H}_1^{\text{rot}}(t)} \\ &\equiv \mathcal{H}_0^{\text{rot}} + \mathcal{H}_1^{\text{rot}}(t)\ .\end{aligned} \tag{1.59}$$

Here we inserted the addition

$$\frac{\hbar}{2}\begin{pmatrix}\omega & 0\\ 0 & -\omega\end{pmatrix} + \frac{\hbar}{2}\begin{pmatrix}-\omega & 0\\ 0 & \omega\end{pmatrix}\ .$$

By doing so, we effectively transferred the problem into a coordinate system rotating with the frequency ω, hence the new Hamiltonians are now labeled with an extra index 'rot'. As we will see, that causes the explicit time-dependence of the Hamiltonian to vanish.

We now apply the Hamiltonian as defined by Eq. (1.59) to Eq. (1.58),

$$\begin{aligned}\mathcal{H}_{\text{D}}^{\text{rot}} &= \mathcal{H}_{0\text{D}}^{\text{rot}} + \mathcal{H}_{1\text{D}}^{\text{rot}} \\ &= \mathrm{e}^{i\mathcal{H}_0^{\text{rot}}t/\hbar}\ [\mathcal{H}_0^{\text{rot}} + \mathcal{H}_1^{\text{rot}}(t)]\ \mathrm{e}^{-i\mathcal{H}_0^{\text{rot}}t/\hbar}\ .\end{aligned} \tag{1.60}$$

The free Hamiltonian in the Dirac picture is identical to the one in the Schrödinger picture,

$$\mathcal{H}_{0\text{D}}^{\text{rot}} \equiv \mathcal{H}_0^{\text{rot}}\ , \tag{1.61}$$

so we obtain

$$\begin{aligned}\mathcal{H}_{\text{D}}^{\text{rot}} &= \mathcal{H}_0^{\text{rot}} + \mathrm{e}^{i\mathcal{H}_0\frac{t}{\hbar}}\begin{pmatrix}\mathrm{e}^{i\frac{\omega}{2}t} & 0\\ 0 & \mathrm{e}^{-i\frac{\omega}{2}t}\end{pmatrix}\mathcal{H}_1^{\text{rot}}(t)\,\mathrm{e}^{-i\mathcal{H}_0\frac{t}{\hbar}}\begin{pmatrix}\mathrm{e}^{-i\frac{\omega}{2}t} & 0\\ 0 & \mathrm{e}^{i\frac{\omega}{2}t}\end{pmatrix} \\ &= \mathcal{H}_0^{\text{rot}} + \frac{\hbar}{2}\begin{pmatrix}\gamma B_0 - \omega & \gamma B_1\mathrm{e}^{i\varphi}\\ \gamma B_1\mathrm{e}^{-i\varphi} & -(\gamma B_0 - \omega)\end{pmatrix} \\ &= \mathcal{H}_0^{\text{rot}} + \mathcal{H}_{1\text{D}}^{\text{rot}}\ .\end{aligned} \tag{1.62}$$

As mentioned above, we are now dealing with the problem in a coordinate system that rotates with the frequency ω and a not explicitly time-dependent Hamiltonian $\mathcal{H}_{1\text{D}}^{\text{rot}}$.

By differentiating the Dirac-state Eq. (1.55) with respect to time, the Schrödinger equations for states and the time-evolution operator in the Dirac picture can be derived to be

$$i\hbar\frac{\partial}{\partial t}\,|\psi_D\rangle = \mathcal{H}_{1\text{D}}^{\text{rot}}\ |\psi_D\rangle \tag{1.63}$$

$$\begin{aligned}i\hbar\,\frac{\partial}{\partial t}U_{\text{D}}(t,t') &= \mathcal{H}_{1\text{D}}^{\text{rot}}\,U_{\text{D}}(t,t') \\ &= \frac{\hbar}{2}\begin{pmatrix}\gamma B_0 - \omega & \gamma B_1\mathrm{e}^{i\varphi}\\ \gamma B_1\mathrm{e}^{-i\varphi} & -(\gamma B_0 - \omega)\end{pmatrix}U_{\text{D}}(t,t')\end{aligned} \tag{1.64}$$

Since $\mathcal{H}_{1D}^{rot}$ is not explicitely time-dependent, the time-ordering operator in Eq. (1.52) becomes the identity. But to be able to actually evaluate Eq. (1.52), we have to diagonalize $\mathcal{H}_{1D}^{rot}$, which means we must find a transformation T transforming it onto its eigenvectors:

$$\widetilde{\mathcal{H}}_{1D}^{rot} = T^{-1}\,\mathcal{H}_{1D}^{rot}\,T\ , \tag{1.65}$$

with $\widetilde{\mathcal{H}}_{1D}^{rot}$ being the diagonalized Hamiltonian. T must be not explicitly time-dependent and invertible, i.e. $T\,T^{-1} = T^{-1}T = \mathbb{1}$.

With such a transformation matrix, the time-evolution operator can now be calculated according to

$$\begin{aligned} U_D(t,t_0) &= T\ \exp\left(\frac{i}{\hbar}\int_{t_0}^{t} T^{-1}\,\mathcal{H}_{1D}^{rot}\,T\,\mathrm{d}t'\right)T^{-1} \\ &= T\ \exp\left(\frac{i}{\hbar}\int_{t_0}^{t} \widetilde{\mathcal{H}}_{1D}^{rot}\,\mathrm{d}t'\right)T^{-1}\ , \end{aligned} \tag{1.66}$$

The validity of this expression becomes obvious when writing the exponential function as its representation as a power series and remembering that $T\,T^{-1} = \mathbb{1}$.

For the eigenvalues $E_{1/2}$ and eigenvectors $\boldsymbol{h}_{1/2}$ of $\mathcal{H}_{1D}^{rot}$ we find

$$E_{1/2} = \pm\frac{\hbar}{2}\sqrt{(\gamma B_0-\omega)^2+(\gamma B_1)^2} \equiv \pm\frac{\hbar}{2}\sqrt{r^2+(\gamma B_1)^2} \equiv \pm\frac{\hbar}{2}\omega_R \tag{1.67}$$

$$\boldsymbol{h}_1 = \begin{pmatrix} \gamma B_1 e^{i\varphi} \\ \sqrt{(\gamma B_0-\omega)^2+(\gamma B_1)^2}-(\gamma B_0-\omega) \end{pmatrix} \equiv \begin{pmatrix} \gamma B_1 e^{i\varphi} \\ \omega_R - r \end{pmatrix} \tag{1.68}$$

$$\boldsymbol{h}_2 = \begin{pmatrix} 1 \\ \dfrac{-(\omega_R+r)}{\gamma B_1 e^{i\varphi}} \end{pmatrix}\ , \tag{1.69}$$

where we introduced two new parameters,

$$r = \gamma B_0 - \omega \equiv \omega_L - \omega \tag{1.70}$$

$$\omega_R = \sqrt{r^2+(\gamma B_1)^2}\ . \tag{1.71}$$

r is the difference between the Larmor frequency $\omega_L \equiv \gamma B_0$ of the static field and the frequency of the rotating field. The so-called Rabi frequency ω_R describes the rotation of the spin in the RF field.

The matrix T which satisfies said properties can be created from the normalized eigenvectors, forming the matrix columns:

$$T = (\boldsymbol{h}_1\ \boldsymbol{h}_2) = \begin{pmatrix} \gamma B_1 e^{i\varphi} & 1 \\ \omega_R - r & -\dfrac{\omega_R+r}{\gamma B_1 e^{i\varphi}} \end{pmatrix}\ , \tag{1.72}$$

the inverted matrix is

$$T^{-1} = \frac{1}{2\,\omega_\mathsf{R}} \begin{pmatrix} \dfrac{\omega_\mathsf{R}+r}{\gamma B_1 \mathsf{e}^{i\varphi}} & 1 \\ \omega_\mathsf{R}-r & -\gamma B_1 \mathsf{e}^{i\varphi} \end{pmatrix} . \tag{1.73}$$

Now we are able to determine the diagonalized Hamiltonian (with the eigenvalues on the diagonal) as well as the time-evolution operator in the Dirac picture. Without loss of generality we will henceforth set $t_0 = t' = 0$ and obtain

$$\widetilde{\mathcal{H}}_{1\mathsf{D}}^{\mathsf{rot}} = \frac{\hbar}{2} \begin{pmatrix} \omega_\mathsf{R} & 0 \\ 0 & -\omega_\mathsf{R} \end{pmatrix} \tag{1.74}$$

$$U_D(t,0) = T \begin{pmatrix} \mathsf{e}^{-i\frac{\omega_\mathsf{R}}{2}t} & 0 \\ 0 & \mathsf{e}^{+i\frac{\omega_\mathsf{R}}{2}t} \end{pmatrix} T^{-1} \tag{1.75}$$

$$\begin{aligned} &= \frac{1}{2\,\omega_\mathsf{R}} \begin{pmatrix} (\omega_\mathsf{R}+r)\cdot \mathsf{e}^{-i\frac{\omega_\mathsf{R}}{2}t} + & \gamma B_1 \mathsf{e}^{i\varphi}\left(\mathsf{e}^{-i\frac{\omega_\mathsf{R}}{2}t} - \mathsf{e}^{+i\frac{\omega_\mathsf{R}}{2}t}\right) \\ (\omega_\mathsf{R}-r)\cdot \mathsf{e}^{+i\frac{\omega_\mathsf{R}}{2}t} & \\ \gamma B_1 \mathsf{e}^{i\varphi}\left(\mathsf{e}^{-i\frac{\omega_\mathsf{R}}{2}t} - \mathsf{e}^{+i\frac{\omega_\mathsf{R}}{2}t}\right) & (\omega_\mathsf{R}-r)\cdot \mathsf{e}^{-i\frac{\omega_\mathsf{R}}{2}t} + \\ & (\omega_\mathsf{R}+r)\cdot \mathsf{e}^{+i\frac{\omega_\mathsf{R}}{2}t} \end{pmatrix} \\ &= \begin{pmatrix} \cos\left(\dfrac{\omega_\mathsf{R}}{2}t\right) - i\,\dfrac{r}{\omega_\mathsf{R}}\,\sin\left(\dfrac{\omega_\mathsf{R}}{2}t\right) & -i\,\dfrac{\gamma B_1}{\omega_\mathsf{R}}\sin\left(\dfrac{\omega_\mathsf{R}}{2}t\right)\mathsf{e}^{i\varphi} \\ -i\,\dfrac{\gamma B_1}{\omega_\mathsf{R}}\sin\left(\dfrac{\omega_\mathsf{R}}{2}t\right)\mathsf{e}^{-i\varphi} & \cos\left(\dfrac{\omega_\mathsf{R}}{2}t\right) + i\,\dfrac{r}{\omega_\mathsf{R}}\,\sin\left(\dfrac{\omega_\mathsf{R}}{2}t\right) \end{pmatrix} . \end{aligned} \tag{1.76}$$

With Eq. (1.57), the time-evolution operator in the laboratory system we find is

$$U(t,0) = \mathsf{e}^{-\frac{i}{\hbar}\mathcal{H}_0^{\mathsf{rot}}t}\, U_\mathsf{D}(t,0) \tag{1.77}$$

$$\begin{aligned} &= \mathsf{e}^{-\frac{i}{\hbar}\mathcal{H}_0^{\mathsf{rot}}t} \begin{pmatrix} \cos\left(\dfrac{\omega_\mathsf{R}}{2}t\right) - i\,\dfrac{r}{\omega_\mathsf{R}}\,\sin\left(\dfrac{\omega_\mathsf{R}}{2}t\right) & -i\,\dfrac{\gamma B_1}{\omega_\mathsf{R}}\sin\left(\dfrac{\omega_\mathsf{R}}{2}t\right)\mathsf{e}^{i\varphi} \\ -i\,\dfrac{\gamma B_1}{\omega_\mathsf{R}}\sin\left(\dfrac{\omega_\mathsf{R}}{2}t\right)\mathsf{e}^{-i\varphi} & \cos\left(\dfrac{\omega_\mathsf{R}}{2}t\right) + i\,\dfrac{r}{\omega_\mathsf{R}}\,\sin\left(\dfrac{\omega_\mathsf{R}}{2}t\right) \end{pmatrix} \\ &= \mathsf{e}^{-\frac{i}{\hbar}\mathcal{H}_0 t} \begin{pmatrix} \left[\cos\left(\dfrac{\omega_\mathsf{R}}{2}t\right) - i\,\dfrac{r}{\omega_\mathsf{R}}\,\sin\left(\dfrac{\omega_\mathsf{R}}{2}t\right)\right]\mathsf{e}^{-i\frac{\omega}{2}t} & -i\,\dfrac{\gamma B_1}{\omega_\mathsf{R}}\sin\left(\dfrac{\omega_\mathsf{R}}{2}t\right)\mathsf{e}^{-i\left(\frac{\omega}{2}t-\varphi\right)} \\ -i\,\dfrac{\gamma B_1}{\omega_\mathsf{R}}\sin\left(\dfrac{\omega_\mathsf{R}}{2}t\right)\mathsf{e}^{i\left(\frac{\omega}{2}t-\varphi\right)} & \left[\cos\left(\dfrac{\omega_\mathsf{R}}{2}t\right) + i\,\dfrac{r}{\omega_\mathsf{R}}\,\sin\left(\dfrac{\omega_\mathsf{R}}{2}t\right)\right]\mathsf{e}^{i\frac{\omega}{2}t} \end{pmatrix} \end{aligned} \tag{1.78}$$

We are now able to calculate the density matrix and with it the polarization $\boldsymbol{P}(t)$ at time t. The former can be derived from Eq. (1.46); however, knowing the exact extensive expression is not crucial in this context, it can be found in Appendix A.1.

Of more interest is the polarization $\boldsymbol{P}(t)$ itself, which can conveniently be calculated from the density matrix like

$$\boldsymbol{P}(t) = \begin{pmatrix} P_\mathsf{x}(t) \\ P_\mathsf{y}(t) \\ P_\mathsf{z}(t) \end{pmatrix} = \begin{pmatrix} \langle\sigma_\mathsf{x}\rangle \\ \langle\sigma_\mathsf{y}\rangle \\ \langle\sigma_\mathsf{z}\rangle \end{pmatrix} = \begin{pmatrix} \mathsf{Tr}(\varrho\,\sigma_\mathsf{x}) \\ \mathsf{Tr}(\varrho\,\sigma_\mathsf{y}) \\ \mathsf{Tr}(\varrho\,\sigma_\mathsf{z}) \end{pmatrix} . \tag{1.79}$$

This finally yields for the polarization vector

$$\boldsymbol{P}(t) = \begin{pmatrix} P_{0x}\left[\frac{1}{2}\cos\omega t\left(1+\cos\omega_R t - \frac{r^2}{\omega_R^2}\left(1-\cos\omega_R t\right)\right) - \right. \\ \left. \frac{r}{\omega_R}\sin\omega t\sin\omega_R t + \frac{\omega_1^2}{\omega_R^2}\cos(\omega t - 2\varphi)\sin^2\frac{\omega_R t}{2}\right] - \\ P_{0y}\left[\frac{1}{2}\sin\omega t\left(1+\cos\omega_R t - \frac{r^2}{\omega_R^2}\left(1-\cos\omega_R t\right)\right) + \right. \\ \left. \frac{r}{\omega_R}\cos\omega t\sin\omega_R t - \frac{\omega_1^2}{\omega_R^2}\sin(\omega t - 2\varphi)\sin^2\frac{\omega_R t}{2}\right] + \\ P_{0z}\frac{\omega_1}{\omega_R}\left[\frac{r}{\omega_R}\cos(\omega t-\varphi)(1-\cos\omega_R t) + \sin(\omega t-\varphi)\sin\omega_R t\right] \\ \\ P_{0x}\left[\frac{1}{2}\sin\omega t\left(1+\cos\omega_R t - \frac{r^2}{\omega_R^2}\left(1-\cos\omega_R t\right)\right) + \right. \\ \left. \frac{r}{\omega_R}\cos\omega t\sin\omega_R t + \frac{\omega_1^2}{\omega_R^2}\sin(\omega t - 2\varphi)\sin^2\frac{\omega_R t}{2}\right] + \\ P_{0y}\left[\frac{1}{2}\cos\omega t\left(1+\cos\omega_R t - \frac{r^2}{\omega_R^2}\left(1-\cos\omega_R t\right)\right) - \right. \\ \left. \frac{r}{\omega_R}\sin\omega t\sin\omega_R t - \frac{\omega_1^2}{\omega_R^2}\cos(\omega t - 2\varphi)\sin^2\frac{\omega_R t}{2}\right] + \\ P_{0z}\frac{\omega_1}{\omega_R}\left[\frac{r}{\omega_R}\sin(\omega t-\varphi)(1-\cos\omega_R t) - \cos(\omega t-\varphi)\sin\omega_R t\right] \\ \\ P_{0x}\frac{\omega_1}{\omega_R}\left[\sin\omega_R t\sin\varphi + \frac{r}{\omega_R}(1-\cos\omega_R t)\cos\varphi\right] + \\ P_{0y}\frac{\omega_1}{\omega_R}\left[\sin\omega_R t\cos\varphi - \frac{r}{\omega_R}(1-\cos\omega_R t)\sin\varphi\right] + \\ P_{0z}\left[1-\frac{\omega_1^2}{\omega_R^2}\left(1-\cos\omega_R t\right)\right] \end{pmatrix}, \tag{1.80}$$

where we introduced the initial polarization vector as $\boldsymbol{P}_0 = (P_{0x}, P_{0y}, P_{0z}) \equiv \boldsymbol{P}(t=0)$ and the Larmor frequency of the rotation field $\omega_1 \equiv \gamma B_1$.

In section 1.2.1 we will elaborate on the NRSE principle, which requires the flipper coil fields to be tuned in such a way that two conditions are met:

1. Static and rotating field must be in resonance, i.e. the Larmor frequency of the static field must match the RF frequency

$$\omega_L = \gamma B_0 \stackrel{!}{=} \omega\ , \tag{1.81}$$

which means in the rotating coordinate system the static field vanishes. In that case the parameter r equals 0 and Eq. (1.80) will take on a much simpler form.

2. The Rabi oscillation must lead in the resonance case to a π-flip around the RF field:

$$\gamma B_1 \cdot \frac{D}{v_0} = \omega_1 \cdot \frac{D}{v_0} \stackrel{!}{=} \pi\ , \tag{1.82}$$

where D is the length of the RF field region.

Corrections for Oscillating RF Fields

As already mentioned above, rotating magnetic fields are implementable only with considerable effort, therefore the RF fields used in NRSE coils are normally realized as linearly oszillating fields. Those fields, like any HF field with arbitrary polarization and fixed frequency, can be represented as two counter-rotating components $B_{1\mathsf{R}}$ and $B_{1\mathsf{O}}$ like in Eq. (1.49). The effects of an additional field component rotating in the inverse sense are elobarately described in [11] and [12], whose description we will follow here.

For a linearly polarized RF field, the two counter-rotating components are of equal strength, $B_{1\mathsf{R}} = B_{1\mathsf{O}} = B_1$. In the rotating coordinate system, the first field component is static, the second rotates with twice the frequency. Its vectorial addition to the static field $\boldsymbol{B}_0$ results in an effective field $\boldsymbol{B}_{0\mathsf{eff}}$, which precesses around the z-axis with 2ω.

The first effect, referred to as the Bloch-Siegert shift, becomes manifest in a small shift of the resonance frequency due to the new effective field

$$B_{0\mathsf{eff}} \approx B_0 \left(1 + \frac{B_1^2}{4B_0^2}\right) \tag{1.83}$$

The second effect concerns the influence on the Rabi frequency, i.e. the „right“ RF component is also slightly altered:

$$B_{1\mathsf{eff}} \approx \frac{(\omega_\mathsf{L} + \omega)^2 + (\gamma B_1)^2}{(\omega_\mathsf{L} + \omega)^2 + (\gamma B_1)^2/2} B_1 \tag{1.84}$$

Depending on the neutron wavelengths and fields used for the experiment, those effects will be more or less noticable. Low frequencies mean small static fields, in which case B_1 becomes comparable to B_0 and will distincly alter the static field.

1.1.4.2 The Polarization in a Spatially Rotating Field

The field $\boldsymbol{B}_2$ corresponds to the situation in an adiabatic spin turning device, such as a coupling coil, where the field vector rotates slowly over a certain distance. The Hamiltonian reads

$$\mathcal{H} = \mathcal{H}_0 + \frac{\hbar}{2}\gamma B_2 \begin{pmatrix} \cos\alpha(x, x_0) & -i\sin\alpha(x, x_0) \\ i\sin\alpha(x, x_0) & -\cos\alpha(x, x_0) \end{pmatrix}. \tag{1.85}$$

We will first examine the situation where the field actually doesn't rotate, i.e. $\alpha = \alpha_0 = \text{const}$. From the results obtained we can also easily derive the case of a guide field, discussed in the following section 1.1.4.3.

$\mathcal{H}$ is not explicitely time-dependent, but we have to diagonalize it to find the time-evolution operator. The procedure is the same as presented in the previous section and leads to the eigenvalues

$$E_{1/2} = \pm\frac{\hbar}{2}\gamma B_2 \equiv \pm\frac{\hbar}{2}\omega_2 \tag{1.86}$$

and a transformation matrix

$$T = \begin{pmatrix} i\sin\alpha_0 & i\sin\alpha_0 \\ \cos\alpha_0 - 1 & \cos\alpha_0 + 1 \end{pmatrix}. \tag{1.87}$$

Applying it (and its inverse matrix) to the Hamiltonian in the same fashion as in Eq. (1.75), we obtain

$$\begin{aligned} U(t,0) &= \mathrm{e}^{\frac{i}{\hbar}\mathcal{H}_0 t}\cdot T \begin{pmatrix} \mathrm{e}^{-\frac{i}{2}\omega_2 t} & 0 \\ 0 & \mathrm{e}^{\frac{i}{2}\omega_2 t} \end{pmatrix} T^{-1} \\ &= \mathrm{e}^{\frac{i}{\hbar}\mathcal{H}_0 t} \begin{pmatrix} \cos\left(\frac{\omega_2}{2}t\right) - i\sin\left(\frac{\omega_2}{2}t\right)\cos\alpha_0 & -\sin\left(\frac{\omega_2}{2}t\right)\sin\alpha_0 \\ \sin\left(\frac{\omega_2}{2}t\right)\sin\alpha_0 & \cos\left(\frac{\omega_2}{2}t\right) + i\sin\left(\frac{\omega_2}{2}t\right)\cos\alpha_0 \end{pmatrix} \end{aligned} \tag{1.88}$$

as the time-evolution operator.

Like above, Eqs. (1.46) and (1.31) let us calculate the density matrix as well as the corresponding polarization vector:

$$\begin{aligned} \varrho(t) = \frac{1}{2}\times \\ \begin{pmatrix} 1 + P_{0\mathrm{z}}[\cos\omega_2 t\sin^2\alpha_0 + \cos^2\alpha_0] - & P_{0\mathrm{x}}[\cos\omega_2 t - i\sin\omega_2 t\cos\alpha_0] - \\ P_{0\mathrm{x}}\sin\omega_2 t\sin\alpha_0 + & iP_{0\mathrm{y}}[\sin^2\alpha_0 + \cos\omega_2 t\cos^2\alpha_0 - \\ P_{0\mathrm{y}}(1-\cos\omega_2 t)\sin\alpha_0\cos\alpha_0 & \quad i\sin\omega_2 t\cos\alpha_0] + \\ & P_{0\mathrm{z}}\sin\alpha_0[\sin\omega_2 t - i(1-\cos\omega_2 t)\cos\alpha_0] \\ P_{0\mathrm{x}}[\cos\omega_2 t + i\sin\omega_2 t\cos\alpha_0] + & \\ iP_{0\mathrm{y}}[\sin^2\alpha_0 + \cos\omega_2 t\cos^2\alpha_0 + & 1 - P_{0\mathrm{z}}[\cos\omega_2 t\sin^2\alpha_0 + \cos^2\alpha_0] + \\ \quad i\sin\omega_2 t\cos\alpha_0] + & P_{0\mathrm{x}}\sin\omega_2 t\sin\alpha_0 - \\ P_{0\mathrm{z}}\sin\alpha_0(\sin\omega_2 t + i(1-\cos\omega_2 t)\cos\alpha_0) & P_{0\mathrm{y}}(1-\cos\omega_2 t)\sin\alpha_0\cos\alpha_0 \end{pmatrix} \end{aligned} \tag{1.89}$$

$$\begin{aligned} \boldsymbol{P}(t) = \\ \begin{pmatrix} P_{0\mathrm{x}}\cos\omega_2 t - P_{0\mathrm{y}}\sin\omega_2 t\cos\alpha_0 + P_{0\mathrm{z}}\sin\omega_2 t\sin\alpha_0 \\ P_{0\mathrm{x}}\sin\omega_2 t\cos\alpha_0 + P_{0\mathrm{y}}(\cos\omega_2 t\cos^2\alpha_0 + \sin^2\alpha_0) + P_{0\mathrm{z}}(1-\cos\omega_2 t)\sin\alpha_0\cos\alpha_0 \\ P_{0\mathrm{z}}(\cos\omega_2 t\sin^2\alpha_0 + \cos^2\alpha_0) - P_{0\mathrm{x}}\sin\omega_2 t\sin\alpha_0 + P_{0\mathrm{y}}(1-\cos\omega_2 t)\sin\alpha_0\cos\alpha_0 \end{pmatrix} \end{aligned} \tag{1.90}$$

We shall now come to the case where $\boldsymbol{B}_2$ is rotating around the x-axis. In order to obtain a solution, we will make use of the results of the previous section.

The spatial field rotation is described by the angle $\alpha(x)$, defined in Eq. (1.51). Now we express it with the average neutron velocity v_0

$$\alpha = \frac{\alpha_{\mathrm{L_{cc}}}\cdot v_0\, t}{L_{\mathrm{cc}}} \equiv \omega_{\mathrm{cc}}\, t\ , \tag{1.91}$$

introducing the new parameter ω_{cc}, which represents the field rotation frequency. For simplicity we chose $x_0 = 0$, i.e. $\bar{v}_n t_0 = 0$. Thus, the magnetic field reads

$$\widetilde{\boldsymbol{B}}_2(t) = \begin{pmatrix} 0 \\ B_2\,\sin\omega_{\mathrm{cc}} t \\ B_2\,\cos\omega_{\mathrm{cc}} t \end{pmatrix}\ . \tag{1.92}$$

and the Hamiltonian becomes (formally) explicitely time-dependent.

If we omit the static component in the NRSE flipper field Eq. (1.49), i.e. $\boldsymbol{B}_0 = 0$, only the rotating component $\boldsymbol{B}_1(t)$ remains and we have a similiar situation as in Eq. (1.92). The obvious difference is that in Eq. (1.50), we introduced the field $\boldsymbol{B}_2$ as turning in the y-z-plane, whereas $\boldsymbol{B}_1$ is rotating in the x-y-plane. The reason for defining $\boldsymbol{B}_2$ like we did in Eq. (1.50) is the fact that in the actual experiment the polarizers and analyzers operate in z-direction.

Comparing the Hamiltonians (1.59) and (1.85), we recognize that the solution strategy we used in the previous section does not apply here due to the time-dependence of the diagonal elements in Eq. (1.85).

The fact that in spin-space the z-axis is a preferential direction is due to our choice of the basis $|\uparrow\rangle, |\downarrow\rangle$, resulting in σ_z being diagonal. But we could just as well choose another basis that prefers a different quantization axis without changing physics. Knowing this, we will solve the problem for the field turning in the x-y plane. As mentioned above, the trace Tr() does not depend on the basis.

Setting $\boldsymbol{B}_0 = 0$, the relevant quantities which we defined before become

$$r = -\omega_{cc} \tag{1.93}$$

$$\omega_R = \sqrt{\omega_{cc}^2 + \omega_{1,2}^2}\,. \tag{1.94}$$

Furthermore, to resemble the situation in a coupling coil, we need to have a defined initial phase φ when neutrons enter the field region. The phase φ corresponds to the parameter α_0 from Eq. (1.51), so in order to have the field initially pointing in $+x$-direction, we have to choose

$$\varphi = 0\,. \tag{1.95}$$

With the preferences Eqs. (1.93)-(1.95), we can directly derive ϱ_{B_1} and $\boldsymbol{P}_{B_1}$ from Eqs. (A.1) and (1.80). Here we will only specify the expression for the polarization, the corresponding density matrix can by found in the Appendix, Eq. (A.2).

$$\boldsymbol{P}_{B_1}(t) = \begin{pmatrix} P_{B_10x}\left[\dfrac{\omega_1^2 + \omega_{cc}^2\cos\omega_R t}{\omega_R^2}\cos\omega_{cc}t - \dfrac{\omega_{cc}}{\omega_R}\sin\omega_{cc}t\sin\omega_R t\right] - \\ P_{B_10y}\left[\sin\omega_{cc}t\cos\omega_R t - \dfrac{\omega_{cc}}{\omega_R}\cos\omega_{cc}t\sin\omega_R t\right] - \\ P_{B_10z}\dfrac{\omega_1}{\omega_R}\left[\dfrac{\omega_{cc}}{\omega_R}\cos\omega_{cc}t\,(1-\cos\omega_R t) - \sin\omega_{cc}t\sin\omega_R t\right] \\ P_{B_10x}\left[\dfrac{\omega_1^2 + \omega_{cc}^2\cos\omega_R t}{\omega_R^2}\sin\omega_{cc}t - \dfrac{\omega_{cc}}{\omega_R}\cos\omega_{cc}t\sin\omega_R t\right] + \\ P_{B_10y}\left[\cos\omega_{cc}t\cos\omega_R t + \dfrac{\omega_{cc}}{\omega_R}\sin\omega_{cc}t\sin\omega_R t\right] - \\ P_{B_10z}\dfrac{\omega_1}{\omega_R}\left[\dfrac{\omega_{cc}}{\omega_R}\sin\omega_{cc}t\,(1-\cos\omega_R t) + \cos\omega_{cc}t\sin\omega_R t\right] \\ -P_{B_10x}\dfrac{\omega_{cc}\,\omega_1}{\omega_R^2}(1-\cos\omega_R t) + P_{B_10y}\dfrac{\omega_1}{\omega_R}\sin\omega_R t - \\ P_{B_10z}\left[1 - \dfrac{\omega_1^2}{\omega_R^2}(1-\cos\omega_R t)\right] \end{pmatrix}, \tag{1.96}$$

The index 'B_1' shall indicate that this result refers to field $\boldsymbol{B}_1$.

To obtain a representation for our actual problem where $\boldsymbol{B}_2$ rotates in the y-z-plane, we can make use of the rotation matrices Eqs. (1.38)-(1.44) derived in section 1.1.3. To transform a field that is rotating around z into one rotating around x in the same sense, we have to apply a rotation around y about an angle $\pi/2$. That leads to a polarization

$$\boldsymbol{P}(t) = \begin{pmatrix} 0 & 0 & -1 \\ 0 & 1 & 0 \\ 1 & 0 & 0 \end{pmatrix} \boldsymbol{P}_{\mathrm{B}_1}(t) = \begin{pmatrix} -P_{\mathrm{B}_1\mathrm{z}} \\ P_{\mathrm{B}_1\mathrm{y}} \\ P_{\mathrm{B}_1\mathrm{x}} \end{pmatrix} \tag{1.97}$$

$$= \begin{pmatrix} -P_{0\mathrm{x}}\left[1 - \frac{\omega_2^2}{\omega_\mathrm{R}^2}\left(1 - \cos\omega_\mathrm{R} t\right)\right] - P_{0\mathrm{y}}\frac{\omega_2}{\omega_\mathrm{R}}\sin\omega_\mathrm{R} t + \\ P_{0\mathrm{z}}\frac{\omega_\mathrm{cc}\,\omega_2}{\omega_\mathrm{R}^2}(1 - \cos\omega_\mathrm{R} t) \\ \\ P_{0\mathrm{x}}\frac{\omega_2}{\omega_\mathrm{R}}\left[\frac{\omega_\mathrm{cc}}{\omega_\mathrm{R}}\sin\omega_\mathrm{cc} t\left(1 - \cos\omega_\mathrm{R} t\right) + \cos\omega_\mathrm{cc} t\sin\omega_\mathrm{R} t\right] + \\ P_{0\mathrm{y}}\left[\cos\omega_\mathrm{cc} t\cos\omega_\mathrm{R} t + \frac{\omega_\mathrm{cc}}{\omega_\mathrm{R}}\sin\omega_\mathrm{cc} t\sin\omega_\mathrm{R} t\right] + \\ P_{0\mathrm{z}}\left[\frac{\omega_2^2 + \omega_\mathrm{cc}^2\cos\omega_\mathrm{R} t}{\omega_\mathrm{R}^2}\sin\omega_\mathrm{cc} t - \frac{\omega_\mathrm{cc}}{\omega_\mathrm{R}}\cos\omega_\mathrm{cc} t\sin\omega_\mathrm{R} t\right] \\ \\ P_{0\mathrm{x}}\frac{\omega_2}{\omega_\mathrm{R}}\left[\frac{\omega_\mathrm{cc}}{\omega_\mathrm{R}}\cos\omega_\mathrm{cc} t\left(1 - \cos\omega_\mathrm{R} t\right) - \sin\omega_\mathrm{cc} t\sin\omega_\mathrm{R} t\right] - \\ P_{0\mathrm{y}}\left[\sin\omega_\mathrm{cc} t\cos\omega_\mathrm{R} t - \frac{\omega_\mathrm{cc}}{\omega_\mathrm{R}}\cos\omega_\mathrm{cc} t\sin\omega_\mathrm{R} t\right] + \\ P_{0\mathrm{z}}\left[\frac{\omega_2^2 + \omega_\mathrm{cc}^2\cos\omega_\mathrm{R} t}{\omega_\mathrm{R}^2}\cos\omega_\mathrm{cc} t - \frac{\omega_\mathrm{cc}}{\omega_\mathrm{R}}\sin\omega_\mathrm{cc} t\sin\omega_\mathrm{R} t\right] \end{pmatrix}, \tag{1.98}$$

where we replaced ω_1 by ω_2 and the initial polarization $\boldsymbol{P}_{\mathrm{B}_1 0}$ by $\boldsymbol{P}_0 = (P_{0\mathrm{x}}, P_{0\mathrm{y}}, P_{0\mathrm{z}}) = (-P_{\mathrm{B}_1 0\mathrm{z}}, P_{\mathrm{B}_1 0\mathrm{y}}, P_{\mathrm{B}_1 0\mathrm{x}})$, which of course had to be rotated as well.

In coupling coils the field needs to turn slowly, i.e. adiabatically. How that is defined, what it actually means for the geometry of a coupling coil and what happens in this case with the polarization vector will be discussed in sections 1.1.4.5 and 2.4.

1.1.4.3 The Polarization in a Static Field

The case $\boldsymbol{B} = \boldsymbol{B}_0$ is the most simple one and with Eq. (1.98) we already deduced a general solution for a static, homogeneous field that is arbitrarily tilted in the x-z-plane by an angle α_0. In order to have the field pointing in $+z$-direction, we need to set $\alpha_0 = 0$ in Eqs. (1.98) and (1.89), which yields a density matrix and polarization

$$\varrho(t) = \frac{1}{2}\begin{pmatrix} 1 + P_{0\mathrm{z}} & \left(P_{0\mathrm{x}} - iP_{0\mathrm{y}}\right)\mathrm{e}^{-i\omega_\mathrm{L} t} \\ \left(P_{0\mathrm{x}} + iP_{0\mathrm{y}}\right)\mathrm{e}^{i\omega_\mathrm{L} t} & 1 - P_{0\mathrm{z}} \end{pmatrix} \tag{1.99}$$

$$\boldsymbol{P}(t) = \begin{pmatrix} P_{0\mathrm{x}}\cos\omega_\mathrm{L} t - P_{0\mathrm{y}}\sin\omega_\mathrm{L} t \\ P_{0\mathrm{x}}\sin\omega_\mathrm{L} t + P_{0\mathrm{y}}\cos\omega_\mathrm{L} t \\ P_{0\mathrm{z}} \end{pmatrix}, \tag{1.100}$$

where $\omega_L \equiv \gamma B_0$ is the Larmor frequency of the static field.

1.1.4.4 Larmor Precession and Guide Fields

Eq. (1.100) describes the time evolution of the polarization in a static and homogeneous field. As we see, the vector $\boldsymbol{P}(t)$ describes a gyroscopic motion, precessing around the static field with an angular frequency ω_L, the Larmor frequency.

Furthermore, the polarization component pointing in field direction (z-direction in our case) is always preserved, which is why such fields are called guide fields.

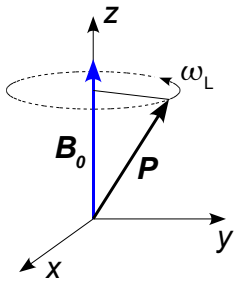

Figure 1.2: Larmor precession of the polarization vector around a static homogenous field.

In practice there will always be other magnetic fields in the experimental area, superimposing the field $\boldsymbol{B}_0$. If the guide field strength is much higher than that of any other magnetic stray field in its region, the resulting field vector will change its direction a) not significantly and b) slowly. In that case, the neutron spins (and hence the polarization vector) will adiabatically follow any field change, as we will show in the next section. Since the change is negligible, the polarization component in field direction is preserved.

1.1.4.5 Adiabatic and Non-adiabatic Transitions – Coupling Coils

In polarized neutron scattering experiments it is important to have the means to modify the polarization vector (i.e. turn its direction) but also preserve its value at the same time. One of such devices is a coupling coil, which implements a slowly (i.e. adiabatically) turning field from z- to y-direction on one side, and an abrupt, non-adiabatic field transition on the other (see section 2.4).

The field rotation is described by α, in Eq. (1.91) we expressed it with the average neutron velocity and introduced the rotation frequency ω_{cc}. For the field transition to be adiabatic, the rotation of the field vector must be slow compared to the rotation of the polarization vector,

$$\omega_{cc} \ll \omega_2 \ , \tag{1.101}$$

which means that the field vector changes insignificantly during on full precession of the polarization vector.

For the adiabatic case where Eq. (1.101) is satisfied, the polarization becomes in second

approximation

$$\boldsymbol{P}_{\mathrm{ad}}(t) \approx \begin{pmatrix} -P_{0\mathrm{x}}\cos\omega_2 t - P_{0\mathrm{y}}\sin\omega_2 t + P_{0\mathrm{z}}\,\dfrac{\omega_{\mathrm{cc}}}{\omega_2}(1-\cos\omega_2 t) \\ P_{0\mathrm{x}}\left[\dfrac{\omega_{\mathrm{cc}}}{\omega_2}\sin\omega_{\mathrm{cc}}t\,(1-\cos\omega_2 t)+\cos\omega_{\mathrm{cc}}t\sin\omega_2 t\right] + \\ P_{0\mathrm{y}}\left[\cos\omega_{\mathrm{cc}}t\cos\omega_2 t+\dfrac{\omega_{\mathrm{cc}}}{\omega_2}\sin\omega_{\mathrm{cc}}t\sin\omega_2 t\right] + \\ P_{0\mathrm{z}}\left[\sin\omega_{\mathrm{cc}}t-\dfrac{\omega_{\mathrm{cc}}}{\omega_2}\cos\omega_{\mathrm{cc}}t\sin\omega_2 t\right] \\ P_{0\mathrm{x}}\left[\dfrac{\omega_{\mathrm{cc}}}{\omega_2}\cos\omega_{\mathrm{cc}}t\,(1-\cos\omega_2 t)-\sin\omega_{\mathrm{cc}}t\sin\omega_2 t\right] - \\ P_{0\mathrm{y}}\left[\sin\omega_{\mathrm{cc}}t\cos\omega_2 t-\dfrac{\omega_{\mathrm{cc}}}{\omega_2}\cos\omega_{\mathrm{cc}}t\sin\omega_2 t\right] + \\ P_{0\mathrm{z}}\left[\cos\omega_{\mathrm{cc}}t-\dfrac{\omega_{\mathrm{cc}}}{\omega_2}\sin\omega_{\mathrm{cc}}t\sin\omega_2 t\right] \end{pmatrix} . \tag{1.102}$$

If we let the initial polarization vector at $t = 0$ point in the initial direction of the field, i.e. $\boldsymbol{P}_0 = (0, 0, P_{0\mathrm{z}})$, we can easily see that it follows the motion of the field vector:

$$\boldsymbol{P}_{\mathrm{ad}}(t) \approx \underbrace{\begin{pmatrix} P_{0\mathrm{z}}\,\dfrac{\omega_{\mathrm{cc}}}{\omega_2}(1-\cos\omega_2 t) \\ P_{0\mathrm{z}}\left[\sin\omega_{\mathrm{cc}}t-\dfrac{\omega_{\mathrm{cc}}}{\omega_2}\cos\omega_{\mathrm{cc}}t\sin\omega_2 t\right] \\ P_{0\mathrm{z}}\left[\cos\omega_{\mathrm{cc}}t-\dfrac{\omega_{\mathrm{cc}}}{\omega_2}\sin\omega_{\mathrm{cc}}t\sin\omega_2 t\right] \end{pmatrix}}_{2^{\mathrm{nd}}\text{ order}} \approx \underbrace{\begin{pmatrix} 0 \\ P_{0\mathrm{z}}\sin\omega_{\mathrm{cc}}t \\ P_{0\mathrm{z}}\cos\omega_{\mathrm{cc}}t \end{pmatrix}}_{1^{\mathrm{st}}\text{ order}} . \tag{1.103}$$

This becomes even more obvious when investigating the time-derivation of the projection of $\boldsymbol{P}_{\mathrm{ad}}$ onto $\boldsymbol{B}_2$ in first order approximation,

$$\frac{\mathrm{d}}{\mathrm{d}t}\,\langle \boldsymbol{B}_2, \boldsymbol{P}\rangle = \frac{\mathrm{d}}{\mathrm{d}t}\left(B_2 P_{0\mathrm{z}}(\sin^2\omega_{\mathrm{cc}}t + \cos^2\omega_{\mathrm{cc}}t)\right) = \frac{\mathrm{d}}{\mathrm{d}t}\,B_2 P_{0\mathrm{z}} = 0\ , \tag{1.104}$$

where $\langle\,,\rangle$ is the scalar product. In second order approximation, we can also observe the superposed precession around the turning field vector with frequency ω_2 (see enlarged box in Fig. 1.3).
To illustrate the situation practically, we assume a coupling field of length $L_{\mathrm{cc}} = 0.2$ m and strength $|\boldsymbol{B}_2| = 10^{-2}$ T, and a neutron velocity of $v_0 = 300$ m/s, which yields $\omega_{\mathrm{cc}} \approx 2.4 \cdot 10^3\ \mathrm{s}^{-1} \ll \omega_{\mathrm{L}} \approx 1.8 \cdot 10^6\ \mathrm{s}^{-1}$. After $t \approx 0.65$ µs the field has turned about $\pi/2$ from z- to y-direction, Fig. 1.3 shows the respective motion of the polarization vector components.

On the other hand, when the field transition is quite sudden, i.e. non-adiabatic, like in the case of a current sheet, the polarization vector cannot follow the field change. For a transition from field region to zero-field, the polarization will therefore remain unchanged.

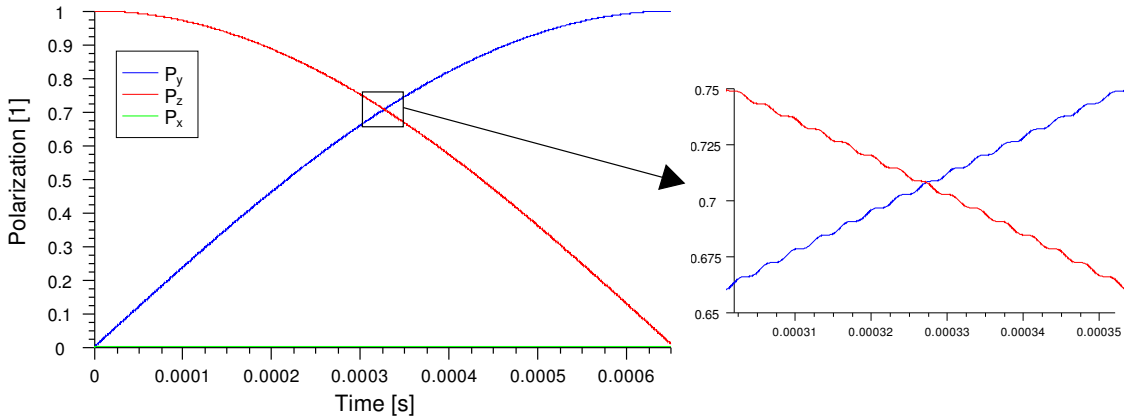

Figure 1.3: Temporal evolution of the polarization vector components in a coupling coil (left), which for adiabatic transitions adapt to the motion of the magnetic field. Superposed in second order approximation is a precession around the field vector (right).

1.1.4.6 Polychromatic Beams

The resonance condition Eq. (1.81) does not depend on the neutron wavelength, whereas the π-flip condition does and was defined in Eq. (1.82) using the average neutron velocity v_0. In practice, neutron beams feature a wavelength distribution $f(\lambda)$ around a maximum average wavelength $\overline{\lambda} = h/(m \cdot v_0)$ with a characteristic width $\Delta\lambda$. Hence, the aforementioned condition cannot be fulfilled for all neutrons, which will result in a decrease in polarization (depolarization).

To obtain an estimation of the effect, we investigate the polarization in z-direction for a flipper coil which fields are tuned to meet the resonance as well as the π-flip condition. We let the incoming polarization point in z-direction, which, according to Eq. (1.80), yields a velocity/wavelength-dependent polarization at the exit of the field region

$$P(v_\mathrm{n}) = P_{0\mathrm{z}} \cos\left(\omega_1 \frac{D}{v_\mathrm{n}}\right) = P_{0\mathrm{z}} \cos\left(\omega_1 \frac{D\, m\, \lambda}{h}\right) = P(\lambda)\ . \tag{1.105}$$

Here h is Planck's constant and m the neutron mass.

For simplicity, we further assume the wavelengths to be equally distributed around $\overline{\lambda}$, i.e. the normalized distribution function is

$$f(\lambda) = \begin{cases} \dfrac{1}{\Delta\lambda}\ ,\ \forall\ \lambda \text{ with } (\overline{\lambda} - \dfrac{\Delta\lambda}{2}) \leq \lambda \leq (\overline{\lambda} + \dfrac{\Delta\lambda}{2}) \\ 0 \quad \text{otherwise} \end{cases}\ . \tag{1.106}$$

Depending on various parameters, like the neutron source or the guide layout, such distributions in practice tend to rather have Maxwellian- or Gaussian-shaped distributions.

By expanding the cosine function in a Taylor series around $\overline{\lambda}$ and integrating over all wave-

lenghts, we obtain for the polarization at the end of the field region

$$P_z = \int_0^\infty f(\lambda) P(\lambda)\, \mathrm{d}\lambda \tag{1.107}$$

$$\approx \frac{1}{\Delta\lambda} P_{0z} \int_{\overline{\lambda}-\frac{\Delta\lambda}{2}}^{\overline{\lambda}+\frac{\Delta\lambda}{2}} -1 + \frac{\omega_1^2 D^2 m^2}{h^2}(\lambda-\overline{\lambda})^2\, \mathrm{d}\lambda$$

$$= P_{0z}\left(-1 + \frac{\omega_1^2 D^2 m^2 \Delta\lambda^2}{24h^2}\right) = P_{0z}\left(-1 + \frac{\pi^2}{24}\left(\frac{\Delta\lambda}{\overline{\lambda}}\right)^2\right), \tag{1.108}$$

where we considered the π-flip condition Eq. (1.82).

With N coils in the beam, the polarization will decrease as

$$P_{z,N} = P_{0z}\left(-1 + \frac{\pi^2}{24}\left(\frac{\Delta\lambda}{\overline{\lambda}}\right)^2\right)^N. \tag{1.109}$$

That means for a neutron beam with $\Delta\lambda/\overline{\lambda} = 10$ %, the expected depolarization of the beam after one NRSE flipper coil is $(|P_{0z}| - |P_z|)/|P_{0z}| \approx 0.4$ %, after 8 coils ≈ 3.2 %.

1.1.5 Polarization Analysis in Practice

For the rest of this work, we choose the z-direction for polarization analysis (compare Figs. 1.1 and 1.4). So when we speak of a polarized beam in practice (i.e. having it prepared or analyzed by means of a polarization device, such as a supermirror) we mean that $P_z \neq 0$.

Within the supermirror polarizers used in our experiments (see section 2.5) the neutron beam is targeted on magnetized layers. Inside the layer, the spin component parallel to the magnetization possesses a higher, the antiparallel component a lower potential energy. If the magnetic potential is of the same height as the nuclear potential, only the parallel spin state will experience a potential well. If that well exceeds the total energy of the spin state, those neutrons will be reflected. The other spin component will be either transmitted or absorbed, depending on the substrate material.

In NRSE or MIEZE experiments the detectors measure counts. How can we convert those into an expression for the polarization of the beam? From Eqs. (1.30) and (1.32) we can derive the following relations for the coefficients of a general spin state

$$P_x = 2\,\Re(c_-^* c_+) \tag{1.110}$$

$$P_y = -2\,\Im(c_-^* c_+) \tag{1.111}$$

$$P_z = |c_+|^2 - |c_-|^2 \tag{1.112}$$

Eq. (1.112) contains the probabilities for the spins being in up or down state, $|c_+|^2$ and $|c_-|^2$. When we align a polarizer in $+z$-direction and measure the count rate, we measure the fraction of neutrons I_+ being in spin-up state (with respect to the z-axis). The same applies to the polarizer aligned in $-z$-direction, in that case we determine I_-. When $(I_+ + I_-)$ is the total

count rate, the probabilities for either case are then

$$|c_+|^2 = \frac{I_+}{I_+ + I_-} \tag{1.113}$$

$$|c_-|^2 = \frac{I_-}{I_+ + I_-} \,. \tag{1.114}$$

That lets us calculate the following expression for the polarization

$$P_z = \frac{I_+ - I_-}{I_+ + I_-} \,. \tag{1.115}$$

In actual experiments the polarization devices are normally not rotated for practical reasons. Instead we use a supermirror for analysis and a device which allows us to inverse spin-up and spin-down, like a π-flipper or adiabatic spin rotator. In two measurements, both with the same supermirror orientation, we determine $I_+ = I_{+\uparrow}$ and $I_- = I_{+\downarrow}$. The notations "$+\uparrow$" and "$+\downarrow$" shall indicate that we measure spin-up in both cases, but with the polarization flipped.

The Polarization of a MIEZE Signal

In MIEZE experiments the polarization analyzer turns the rotating polarization vector into a time-dependend, intensity-modulated signal (see section 1.3) and we measure the intensity $I(t_\mathrm{D})$. A maximum or minimum count rate at the detector at time t_D corresponds to the neutrons being in spin-up or spin-down state, respectively.

The exact expression for the polarization at the detector at an arbitrary time $\boldsymbol{P}(t_\mathrm{D})$ will be derived in section 1.3. The absolute maximum polarization value achieved by the MIEZE setup is determinable by the extremal values in the oscillating signal. Since the signal is time-dependent, the contrast C is introduced and replaces the polarization P. It is defined equivalently to Eq. (1.115):

$$C = \frac{I_\mathrm{max} - I_\mathrm{min}}{I_\mathrm{max} + I_\mathrm{min}} \,. \tag{1.116}$$

with I_max and I_min being the maximum and minimum count rates observed.

If the MIEZE signal was completely depolarized, i.e. $P_\mathrm{z}(t_\mathrm{D}) = 0$, we would measure an average constant count rate of

$$I(t_\mathrm{D}) = \frac{I_\mathrm{max} + I_\mathrm{min}}{2} = \frac{I_0}{2} \,, \tag{1.117}$$

with I_0 being the count rate before entering the analyser.

1.2 NSE and NRSE

Speaking in semi-classical terms, the idea behind N(R)SE is to investigate the inelastic or quasi-elastic scattering properties of a sample by coding the information about them in the precession angle of the neutron spins in magnetic fields. In other words, the change of the neutron energy or energy distribution caused by scattering is determined by comparing the Larmor precession angles in two well-known magnetic fields before and after the scattering. As opposed to other spectrometer types, the resolution of an NSE instrument does not depend on the wavelength distribution of the incident neutron beam, which we will see in the following.

The corresponding quantum mechanical view explains Neutron Spin Echo by the different kinetic energies the spin-up and spin-down states have in magnetic fields. The detectable decrease in polarization is caused by a change in kinetic energy of both spin states and the decrease of the propability for coherent superposition after the second field region.

We will elaborate on the quantum mechanical picture in more detail in section 1.2.1, for demonstrating the common working principle of NSE and NRSE we will for now use the semi-classical formalism.

The experimental principle of NSE is depicted in Fig. 1.4: A fairly monochromatic (typically $\Delta\lambda/\overline{\lambda} \approx 10\ \%$) and polarized neutron beam enters a homogeneous, static magnetic field region with strength B_1, where the neutron spins start to precess. After the first field region of length L_1 the polarization in z-direction P_z is destroyed due to the wavelength distribution of the beam. The neutrons have accumulated a precession angle

$$\varphi_1 = \frac{\gamma\, m\, \lambda_1}{h} \int\limits_{L_1} B_1 \,\mathrm{d}l \equiv \frac{\gamma\, m\, \lambda_1}{h}\, J_1 \,, \tag{1.118}$$

when they enter the sample region. Within the sample, the kinetic energy and thus the neutron wavelength changes if the scattering is inelastic. After the sample, the second field region B_2 is entered, where the precession angle

$$\varphi_2 = \frac{\gamma\, m\, \lambda_2}{h} \int\limits_{L_2} B_2 \,\mathrm{d}l \equiv \frac{\gamma\, m\, \lambda_2}{h}\, J_2 \,, \tag{1.119}$$

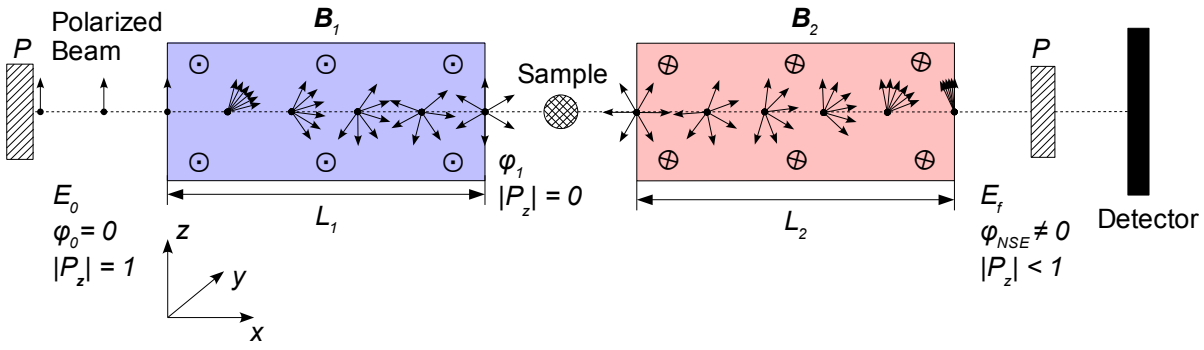

Figure 1.4: Working principle of an NSE instrument (P: Polarization device, $B_{1,2}$: Static, homogeneous magnetic fields). The rotating arrows indicate the Larmor precession. In practice, NSE spectrometers are implemented with fields along the x-direction, the spin then precesses in the y-z plane.

is added. When the direction of the fields is anti-parallel, the total precession angle reads

$$\varphi_{\mathsf{NSE}} = \frac{\gamma\, m}{h}(J_1\lambda_1 - J_2\lambda_2)\ . \tag{1.120}$$

Without a sample or if the scattering would have been elastic, the wavelength does not change after the sample region ($\lambda_1 = \lambda_2 = \lambda$).

In the symmetric case where the path integrals J_1 and J_2 are equal, the precession angle gained in the first field is simply canceled in the second. Hence, full polarization is restored, even for a non-monchromatic beam („Spin Echo"). Behind the second field region, the beam is analyzed in a polarizer (e.g. supermirror bender), after which any further precession will have no effect on the measurement.

In the case of elastic scattering, the polarization in analysis direction as a function of the path integrals for a polychromatic beam is given by Eqs. (1.100) and (1.108),

$$P_{\mathsf{NSE}} = \int_0^\infty f(\lambda)\cos\varphi_{\mathsf{NSE}}\,\mathrm{d}\lambda = \int_0^\infty f(\lambda)\cos\left(\frac{\gamma\, m\,\lambda}{h}\,(J_1 - J_2)\right)\,\mathrm{d}\lambda\,, \tag{1.121}$$

where $f(\lambda)$ is again the normalized wavelength distribution.

For inelastic or quasielastic scattering however, an energy transfer (non-relativistic)

$$E_{\mathsf{s}} = \frac{h^2}{2m}\left(\frac{1}{\lambda_1^2} - \frac{1}{\lambda_2^2}\right) = \hbar\,\omega_{\mathsf{s}} \tag{1.122}$$

takes place, whose distribution – depending on the scattering process itself – has a characteristic shape and width. It is this information that holds special interest as it provides insight into the respective inner physical processes involved. The amount of energy $\hbar\Delta\omega_{\mathsf{s}}$ transferred to each neutron depends on the aforementioned distribution and results in an altered velocity (or k-vector). This causes the neutrons to accumulate different precession angles in the second field and hence leads to a decrease in polarization.

To obtain a representation for the precession angle φ_{NSE} as a function of ω_{s}, one has to expand Eq. (1.122) around the average scattering energy $\overline{E}_{\mathsf{s}}$ and calculate the deviation $\mathrm{d}\omega_{\mathsf{s}}$ (see [11]).

The resulting deviation of the precession angle reads

$$\mathrm{d}\varphi_{\mathsf{NSE}} = \underbrace{\frac{\gamma\, m^2}{2\pi h^2}\,\overline{\lambda}_1^3\, J_1}_{\tau_{\mathsf{NSE}}}\,\mathrm{d}\omega_{\mathsf{s}} + \frac{\gamma\, m}{h}\left(J_1\,\frac{\overline{\lambda}_1^3}{\overline{\lambda}_2^3} - J_2\right)\mathrm{d}\lambda_2\ . \tag{1.123}$$

We see that in order to make the precession angle variation independent from the wavelength change $\mathrm{d}\lambda_2$, the following so-called spin echo condition must be fulfilled

$$\frac{J_1}{J_2} \overset{\substack{\text{homog.}\\ \text{fields}}}{=} \frac{B_1 L_1}{B_2 L_2} \overset{!}{=} \frac{\overline{\lambda}_1^3}{\overline{\lambda}_2^3} = \frac{\overline{v}_{\mathsf{n}2}^3}{\overline{v}_{\mathsf{n}1}^3}\ . \tag{1.124}$$

The parameter from Eq. (1.123)

$$\tau_{\mathsf{NSE}} = \frac{\gamma\, m^2}{2\pi h^2}\,\overline{\lambda}_1^3\, J_1 = \frac{\gamma\,\hbar}{m}\,\frac{J_1}{\overline{v}_{\mathsf{n}1}^3} \tag{1.125}$$

is called spin echo time. It is instrument-dependent and is a measure for the achievable resolution.

The scattering process is described by the scattering function $S(\boldsymbol{Q}, \omega_\mathsf{s})$, which is characteristic for the sample. We should mention that in general, the dependence of the energy transfer $\hbar\omega_\mathsf{s}$ from momentum transfer $\boldsymbol{Q}$ (dispersion), which we neglected here, must be taken into account for inelastic scattering. Since this is not important in our context, we refer to e.g. [4] for further reading and a general solution.

The polarization of the scattered neutron beam at the point where the spin echo condition Eq. (1.124) is fulfilled (spin echo point) reads

$$P_\mathsf{NSE} = \int_0^\infty f(\lambda) \int_0^\infty S(\boldsymbol{Q}, \omega_\mathsf{s}) \cos(\omega_\mathsf{s}\tau_\mathsf{NSE} - \overline{\omega}_\mathsf{s}\tau_\mathsf{NSE})\, \mathrm{d}\omega_\mathsf{s}\, \mathrm{d}\lambda \ . \tag{1.126}$$

That means the polarization is proportional to the cosine Fourier transformation of the scattering function. The intermediary scattering function $S(\boldsymbol{Q}, \tau_\mathsf{s})$ is the full Fourier transformation of $S(\boldsymbol{Q}, \omega_\mathsf{s})$. For very small quasi-elastic energy transfers $S(\boldsymbol{Q}, \omega_\mathsf{s})$ is symmetric (Boltzmann distribution) and the cosine Fourier transformation equals the Fourier transformation. So the polarization is proportional to the intermediary scattering function

$$P_\mathsf{NSE} \sim \int_0^\infty S(\boldsymbol{Q}, \omega_\mathsf{s}) \cos(\omega_\mathsf{s}\tau_\mathsf{NSE} - \overline{\omega}_\mathsf{s}\tau_\mathsf{NSE})\, \mathrm{d}\omega_\mathsf{s} = S(\boldsymbol{Q}, \tau_\mathsf{NSE}) \ , \tag{1.127}$$

which represents the underlying scattering process. Information about the latter can therefore by obtained by investigating the decrease in polarization at the spin echo point for various τ_NSE.

1.2.1 NRSE

The NSE technique produces the required neutron spin precession by two large, constant magnetic fields. In 1987, Golub and Gähler proposed the Neutron Resonance Spin Echo (NRSE) variant, which replaces the long constant fields by zero field regions enclosed by two RF spin flippers, creating so-called pseudo-fields. The principle setup is depicted in Fig. 1.5.

The neutron precession in the constant NSE fields corresponds to the rotation of the RF field in the flipper coils, which are phase-locked. Simply put, in NRSE we let the fields rotate instead of the neutrons. In the next sections we will show that the two methods are equivalent.

1.2.1.1 Quantum Mechanical Picture

NRSE and the MIEZE technique utilize the same hardware components, but a MIEZE spectrometer is more closely connected to interferometry. This becomes apparent especially in the quantum mechanical picture, which is sketched in the following for NRSE. We will go into some additional aspects of the quantum mechanical viewpoint in the next section about MIEZE.

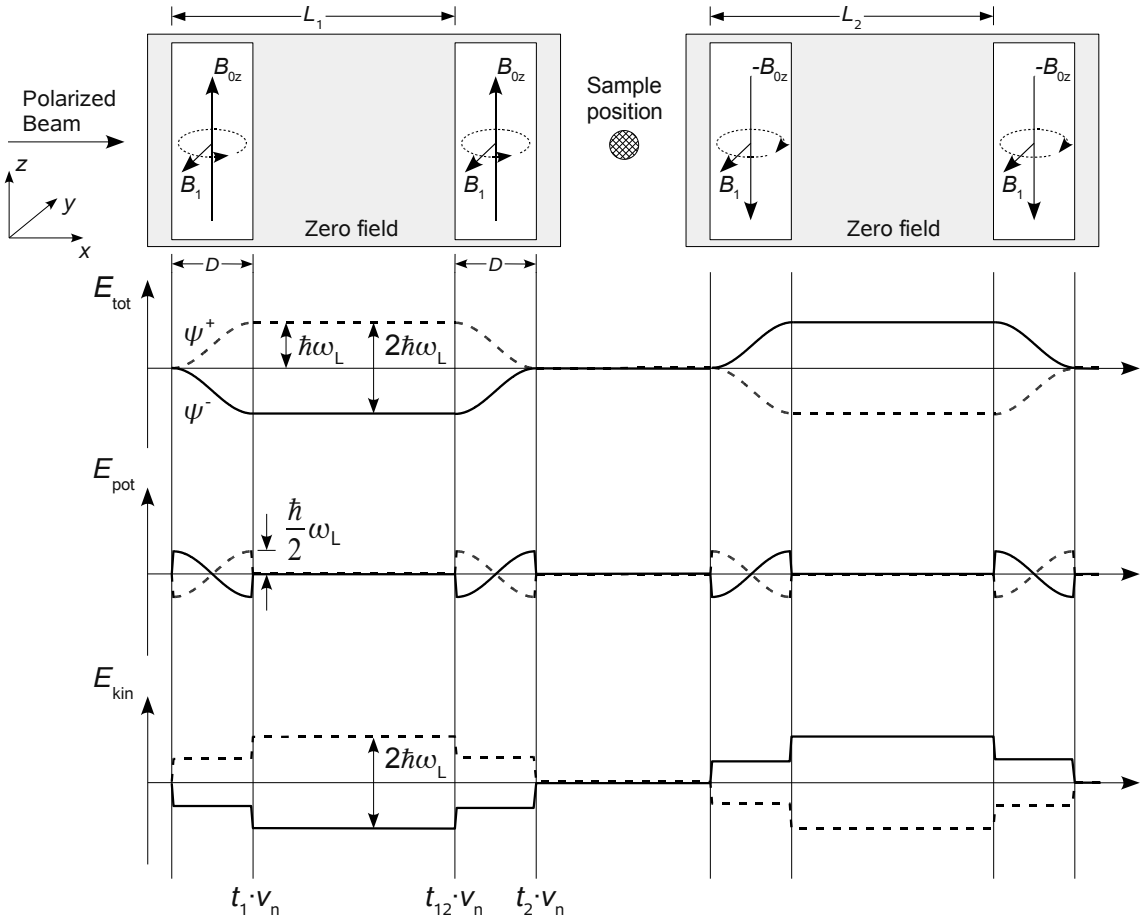

Figure 1.5: Working principle of an NRSE instrument (polarization devices and detector have been omitted). The Resonance Flipper Coils are contained in zero-field regions. Shown below the sketched setup are the levels of potential, kinetic, and total energy for the neutron wavefunctions $\psi^{\pm}$ of the two spin directions for a symmetric field configuration. The splitting in energy is twice that of a conventional NSE instrument for static fields of equal magnitude.

We have chosen to define the static fields in our NRSE flippers to point along the z-axis. The three components of the spin are complementary variables, hence they are not all simultaneously well-defined. By performing a measurement, one disturbs the system „neutron spin“. Applying a magnetic field to a neutron beam is equivalent to a measurement, since by doing so we define a quantization direction, which also means we determine the basis in which to describe the beam polarization. The incoming polarization in an NRSE setup must be perpendicular to the static field. In our case, we defined that to be the y-direction. If the beam is polarized in $+y$-direction when entering the magnetic field region, the spin-up and spin-down states ψ^+ and ψ^- are distributed with equal probabilities with respect to the z-direction.

With Eq. (1.78) we have already deduced the time-evolution operator for the field configuration of NRSE coils. The operator for the field-free region is that of a free particle. The spin-up and spin-down states after the first arm of an NRSE instrument can then be calculated as

$$U_2(t_2, t_{12})\, U_0(t_{12}, t_1)\, U_1(t_1)\, \psi_0 \;, \tag{1.128}$$

where t_1, $t_{12} = t_1 + \frac{L-D}{v_0}$, and t_2 are the points in time after the first, at the beginning of the second and after the second coil, respectively (see also Table 1.1).

If the coils are tuned to match both resonance and π-flip condition (Eqs. (1.81) and (1.82)), the spin state in the first field region reads

$$\begin{aligned}\psi_1 = \begin{bmatrix}\psi_1^+\\ \psi_1^-\end{bmatrix} &= \mathrm{e}^{-\frac{i}{\hbar}\mathcal{H}_0 t}\begin{pmatrix}\cos\left(\frac{\omega_1}{2}t\right)\mathrm{e}^{-i\frac{\omega}{2}t} & -i\sin\left(\frac{\omega_1}{2}t\right)\mathrm{e}^{-i\left(\frac{\omega}{2}t-\varphi_1\right)}\\ -i\sin\left(\frac{\omega_1}{2}t\right)\mathrm{e}^{i\left(\frac{\omega}{2}t-\varphi_1\right)} & \cos\left(\frac{\omega_1}{2}t\right)\mathrm{e}^{i\frac{\omega}{2}t}\end{pmatrix}\begin{bmatrix}\psi_0^+\\ \psi_0^-\end{bmatrix}\\ &= \mathrm{e}^{-\frac{i}{\hbar}\mathcal{H}_0 t}\begin{pmatrix}\cos\left(\frac{\omega_1}{2}t\right)\mathrm{e}^{-\frac{i}{\hbar}\frac{\hbar}{2}\gamma B_0 t} & -i\sin\left(\frac{\omega_1}{2}t\right)\mathrm{e}^{-\frac{i}{\hbar}\frac{\hbar}{2}\gamma B_0 t}\,\mathrm{e}^{i\varphi_1}\\ -i\sin\left(\frac{\omega_1}{2}t\right)\mathrm{e}^{-\frac{i}{\hbar}\left(-\frac{\hbar}{2}\gamma B_0 t\right)}\,\mathrm{e}^{-i\varphi_1} & \cos\left(\frac{\omega_1}{2}t\right)\mathrm{e}^{-\frac{i}{\hbar}\left(-\frac{\hbar}{2}\gamma B_0 t\right)}\end{pmatrix}\begin{bmatrix}\psi_0^+\\ \psi_0^-\end{bmatrix}\end{aligned} \tag{1.129}$$

$\psi^{\pm}$ are the initial incoming spin states in z-direction, ψ_1 and φ_1 were labelled with the index '1' to indicate that this is the situation in the first coil.

At the end of the first coil, i.e. at time $t = t_1 = \frac{D}{v_0}$, we find

$$\begin{aligned}\psi_1(t_1) &= \begin{pmatrix}-i\mathrm{e}^{-\frac{i}{\hbar}\left(\mathcal{H}_0+\frac{\hbar}{2}\gamma B_0\right)t_1}\,\mathrm{e}^{i\varphi_1} & 0\\ 0 & -i\mathrm{e}^{-\frac{i}{\hbar}\left(\mathcal{H}_0-\frac{\hbar}{2}\gamma B_0\right)t_1}\,\mathrm{e}^{-i\varphi_1}\end{pmatrix}\begin{pmatrix}0 & 1\\ 1 & 0\end{pmatrix}\begin{bmatrix}\psi^+\\ \psi^-\end{bmatrix}\\ &= \begin{pmatrix}-i\mathrm{e}^{-\frac{i}{\hbar}\left(\mathcal{H}_0+\frac{\hbar}{2}\gamma B_0\right)t_1}\,\mathrm{e}^{i\varphi_1} & 0\\ 0 & -i\mathrm{e}^{-\frac{i}{\hbar}\left(\mathcal{H}_0-\frac{\hbar}{2}\gamma B_0\right)t_1}\,\mathrm{e}^{-i\varphi_1}\end{pmatrix}\begin{bmatrix}\psi^-\\ \psi^+\end{bmatrix}\,.\end{aligned} \tag{1.130}$$

At the magnetic field borders transitions can be induced between the spin states by resonant electro-magnetic radiation, revealing strong similarities to the well-known Nuclear Magnetic Resonance (NMR) or Electron Spin Resonance (ESR) techniques. If frequencies and field intensities are adjusted appropriately, it is possible to achieve a complete population inversion of the two spin states. Eq. (1.130) shows exactly this, the resonance and π-flip conditions cause the non-diagonal elements to vanish and the population inversion corresponds to a π-flip of the polarization vector.

By photon absorption and emission from and to the radiation field, the total energy of the spin states changes after passage of a coil, i.e. due to the spin state inversion, the energy splitting is not reverted at the field boundaries. As we see in Fig. 1.5, spin-up and spin-down travel the zero-field space between the coils at different velocities, with the energy splitting between the two being $2\hbar\,\omega_{\mathsf{L}}$.

In the static homogeneous field of an NSE instrument, the total energy does not change for either of the spin states. Potential and kinetic energy in that case are

$$E_{\mathsf{pot}}^{\pm} = \mp\frac{\hbar\gamma B_0}{2}\,,\quad E_{\mathsf{kin}}^{\pm} = \pm\frac{\hbar\gamma B_0}{2}\,, \tag{1.131}$$

resulting in a splitting between spin-up and spin-down of ω_{L}. So for equally strong static fields, the splitting in kinetic energy (and hence the instrument resolution) is two times higher for NRSE compared to conventional NSE.

In the zero-field region the neutrons travel like free particles and experience no magnetic potential, hence no additional phase is accumulated.

The description of the time-evolution in the second field area is equivalent to that of the first. If the initial phases φ_1 and φ_2 at time $t = 0$ were equal (phase-locked) for both spin

states, the phases of the second RF field at time t_{12} can be expressed by the angular frequency of the field and the flight time:

$$\varphi_2(t_{12}) = \varphi_1 + \omega\frac{L_1}{v_0} \overset{\text{Reson.}}{=} \varphi_1 + \omega_\mathsf{L}\frac{L_1}{v_0} \tag{1.132}$$

According to Eq. (1.128), the spin state at the exit of the second flipper at time $t = t_2 = t_1 + (L_1 - D)/v_0 + D/v_0 = t_1 + L_1/v_0$ is represented by

$$\psi_2(t_2) = \mathrm{e}^{-\frac{i}{\hbar}\mathcal{H}_0\frac{L_1+D}{v_0}} \begin{pmatrix} \mathrm{e}^{-i(\pi-\omega_\mathsf{L}\frac{L_1}{v_0})} & 0 \\ 0 & \mathrm{e}^{-i(\pi+\omega_\mathsf{L}\frac{L_1}{v_0})} \end{pmatrix} \begin{bmatrix} \psi^+ \\ \psi^- \end{bmatrix} \tag{1.133}$$

The spin-up and spin-down states have now reached the same energy level again (s. Fig. 1.5) but accumulated different phases. The total phase difference after the second coil is

$$\Delta\varphi_{12} = 2\,\omega_\mathsf{L}\frac{L_1}{v_0} \tag{1.134}$$

which corresponds to the result we obtain in the classical picture (s. next section). Without the presence of a sample, the phases will be cancelled in the second NRSE arm. The analogy to NSE becomes obvious.

We shall point out, that it is the above described splitting in energy and momentum in the field free region which provides the basis for both the pseudo-field concept and the MIEZE technique with its interferometric character.

Another point that we silently assumed during this quantum mechanical description concerns the fact that at the field borders, which constitute potential wells, an incoming wave would be partially reflected. We can neglect those reflected parts like we did, if the potential energy in the magnetic field is small compared to the neutron energy,

$$\gamma B_0 = \omega_\mathsf{L} \ll \omega_0 \ , \tag{1.135}$$

where ω_0 is the matter wave angular frequency of the neutron.

1.2.1.2 Classical Picture

In this picture we investigate the precession angle of the neutron spins (i.e. the polarization vector) that is accumulated when passing the assembly.

When the coils are tuned to resonance and the incoming neutron beam is polarized in $+y$-direction, $\boldsymbol{P}$ performs a π-flip around the RF field vector in the x-y-plane. This can be understood most clearly when changing into the rotating coordinate system we used in section 1.1.4.1, where the static field $\boldsymbol{B}_0$ is gone and the rotating field $\boldsymbol{B}_1$ is static.

The angle between the initial and the final direction of $\boldsymbol{P}$ before the first and after the second coil does only depend on the orientation of the RF field vectors when the coils are entered:

$$\Delta\varphi_{12} = 2(\varphi_2 - \varphi_1) = 2\,\omega_\mathsf{L}\,\frac{L_1}{v_0} = 2\,\omega_\mathsf{L}\,\frac{L_1}{v_{\mathsf{n}1}} \ . \tag{1.136}$$

$\varphi_{1/2}$ are the RF field phases. As in Eq. (1.132), we expressed φ_2 by $\varphi_1 + \omega_\mathsf{L}\frac{L_1}{v_0}$.

We obtain the analogous expression for the second NRSE arm, i.e. coils 3 and 4 at distance L_2. The net angle after the instrument therefore reads

$$\begin{aligned}\varphi_{\mathsf{NRSE}} &= \Delta\varphi_{12} - \Delta\varphi_{34} \\ &= 2\omega_{\mathsf{L}} \left(\frac{L_1}{v_{\mathsf{n}1}} - \frac{L_2}{v_{\mathsf{n}2}} \right) = 2\,\frac{\gamma\, m}{h} \left(B_{01} L_1 \lambda_1 - B_{02} L_2 \lambda_2 \right) \,. \end{aligned} \tag{1.137}$$

This is the equivalent expression to Eq. (1.120), differing by a factor of 2.

The spin echo time of an NRSE instrument can be derived in the same manner as its equivalent Eq. (1.125) for NSE:

$$\tau_{\mathsf{NRSE}} = \frac{2\hbar\omega_{\mathsf{L}} L}{m \bar{v}_{\mathsf{n}}^3} = \frac{\gamma\,\hbar}{m}\,\frac{2 B_0 L}{v_0^3}\,, \tag{1.138}$$

where $L = L_1 = L_2$.

1.2.1.3 Bootstrap NRSE

The resolution of the instrument can be improved by making use of the so-called bootstrap technique shown in Fig. 1.6. By stacking N identical flipper coils along the neutron flight path with alternating static field directions, the precession angle (and hence the resolution) is increased by a factor N (s. [4]). Quantum mechanically seen, the alternating non-adiabatic field transitions represent additional potential wells, each causing additional splitting of the spin states as described in section 1.2.1.1.

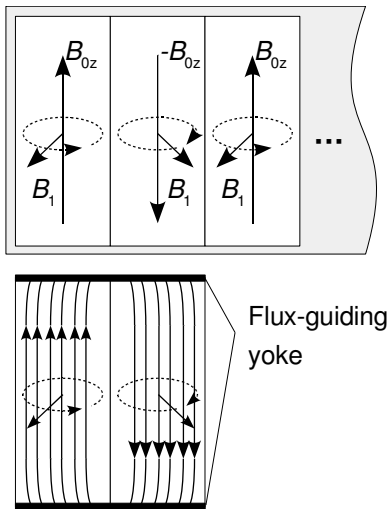

Figure 1.6: Boostrap principle. Two subsequent coils act as each others flux refeed.

Besides the resolution enhancement the boostrap technique has another advantage. If the number of coils N is even, two subsequent coils act as each others field refeed, since the magnetic flux forms a closed loop (s. Fig. 1.6). This is normally supported by implementing a yoke made of a soft magnetic material (e.g. Mu-metal®) to guide the flux.

There are also drawbacks, the obvious ones are the higher neutron absorption and increased small angle scattering, since the amount of material in the beam also increases by a factor N. The additional effort the technical implementation requires must be taken into account as well. Associated with the technical aspect are the effects of magnetic field inhomogeneities, which become even more relevant with higher N. Another factor is the intrinsic decrease in polarization due to the polychromatic beam, which we already estimated in Eq. (1.109).

Due to the aforementioned reasons, practically all NRSE/MIEZE instruments operate with double boostrap coils.

1.3 Modulation of IntEnsity by Zero Effort (MIEZE)

The Resonance Spin Echo variant MIEZE is the technique which this work focuses on. The principle setup using bootstrap coils is shown in Fig. 1.7. The most obvious difference to an NRSE instrument is the missing second arm. The sample position is now located behind the analyser and outside any zero-field region. That relaxes the requirements for the implementation of the sample environment and e.g. has the advantage of easily applying strong magnetic fields or realizing long beam geometries.

Explaining the working principle of an NRSE instrument, we pointed out the analogies to a conventional NSE instrument. In case of the MIEZE technique however, it seems more appropriate to draw a comparison to an interferometer.

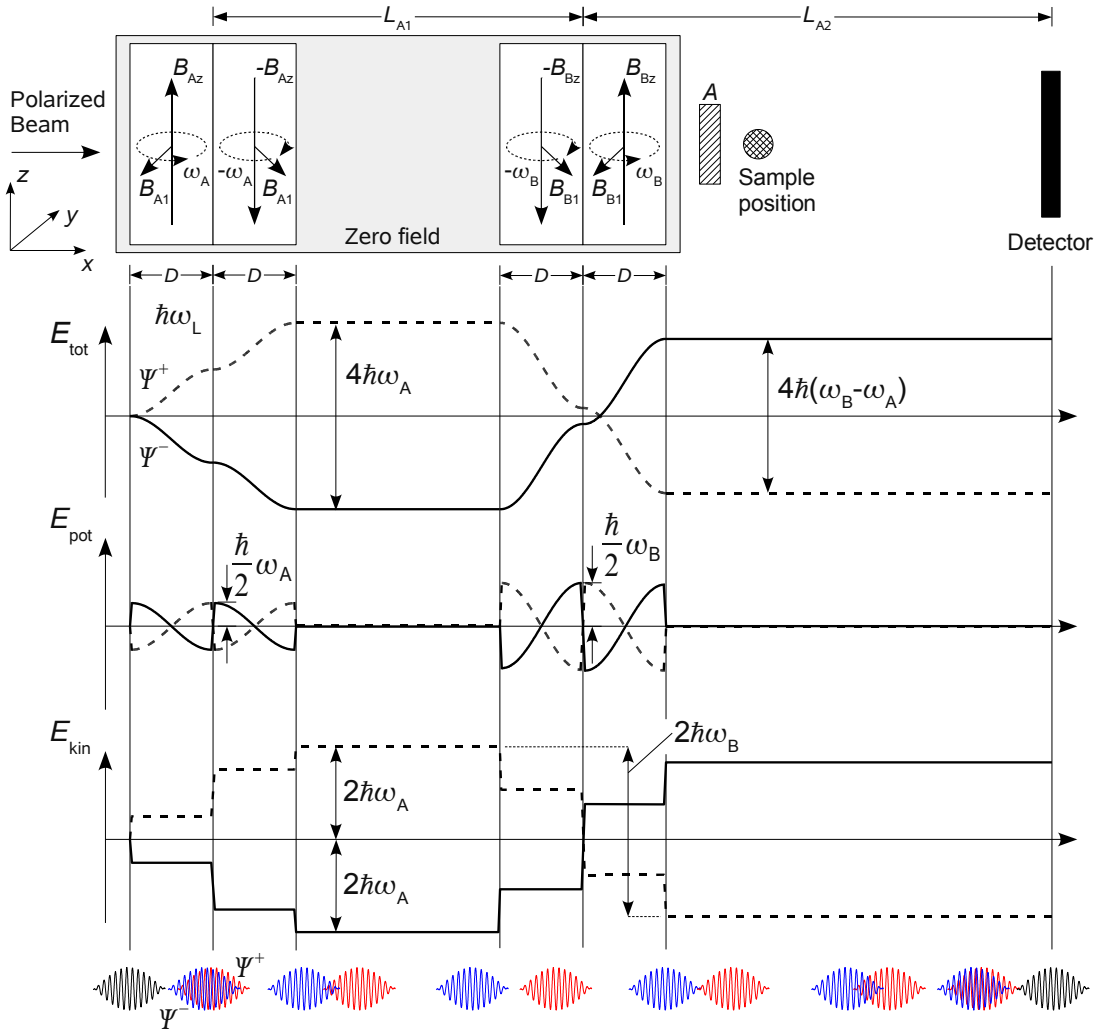

Figure 1.7: Working principle of a bootstrap MIEZE instrument. Only two Resonance Flipper Coils (contained in a zero-field region) are left, the second NRSE arm is omitted. The second coil is operated at a higher frequency compared to the first. Shown below the setup are the levels of potential, kinetic, and total energy for the neutron wavefunctions $\psi^{\pm}$ of the two spin directions, which are coherently split in the first coil. The energy splitting is reversed in the second coil to an extent which leads to a velocity focusing at a distance L_2 (detector plane), i.e. the spin-down state (blue) catches up with spin-up (red) and they are able to interfere. Their coherence volumina are symbolized by wave packets, the longitudinal splitting can actually be much larger than the coherence length.

The two coils are now being operated at a different frequency. As we will see below, that causes the phases of the two spin-states to be time-dependent after the second coil. The spatial splitting, which happens in a Mach-Zehnder interferometer, corresponds in the case of MIEZE to a coherent splitting in momentum and energy of the incoming spin-up and spin-down states. By operating the second coil with a higher frequency and static field than the first, the energy splitting is reversed. That causes a velocity focusing at the detector plane since the formerly separated states approach each other again. Their coherence volumina overlap after a distance L_{A2} and are then able to interfere positively. The point at which the focusing happens is determined by the so-called MIEZE condition, a relation between the coil/detector distances and HF frequencies. It can be viewed as the counterpart to the NSE condition Eq. (1.124) from the previous section.

When describing the MIEZE spectrometer theoretically, the chosen physical picture (and hence the mathematical formalism) is important when it comes to interpreting and understanding the way MIEZE works and the prospects for possible applications.

Two basically different approaches are obviously the (semi-)classical and quantum mechanical pictures. The former is based on the interpretation of the neutron as a classical, single particle with a magnetic moment, which is represented by the spin. Taking the classical viewpoint it is also no problem to describe the passage of a single, localized neutron through the assembly. The phase accumulation is derived from the concept of spin precession and the MIEZE condition follows from the cancellation of the time-independent parts of the phase at the detector.

For a classical description of MIEZE we refer to [4], but here we want to focus on the quantum mechanical picture and the additional aspects it introduces. Before presenting the treatment of a MIEZE instrument with single coils using the time-evolution operators we already calculated, we shall start with a few remarks and point out some difficulties.

The incoming neutron beam (polarized in y-direction) is written in spinor notation, in our case spin-up and spin-down states are equally distributed with respect to the z-axis. A general respresentation of this is

$$\psi_0 = \begin{bmatrix} \psi_0^+ \\ \psi_0^- \end{bmatrix} = \frac{1}{\sqrt{2}} \begin{bmatrix} 1 \\ 1 \end{bmatrix} \ .$$

Looking at NSE where the spinor enters a static, homogeneous magnetic field, we see that spin-up and spin-down have different kinetic energies and wave vectors (or velocities) within the field region, but their total energy is unchanged (both inside and outside the field) and the kinetic energy reverts to its initial level when exiting the field. Here the quantum mechanical and classical pictures appear coherent: A classical particle does not change its velocity, rather is its spin vector $\boldsymbol{S}$ precessing according to $\frac{\mathrm{d}}{\mathrm{d}t}\boldsymbol{S} = \gamma \boldsymbol{S} \times \boldsymbol{B}$. As Golub et al. pointed out in [13], the semi-classical concept of Larmor precession and the time-dependence of $\boldsymbol{S}$ at a certain position can be interpreted as the interference of two waves (spin-up and spin-down) with different wave vectors.

The situation changes however in the case of magnetic resonance; when using time-dependent and resonantly tuned RF fields like in our flipper coils, we will see that when applying the formalism, spin-up and spin-down do experience a change in total (and hence kinetic) energy that is not cancelled after the coil, which we already illustrated by Fig. 1.5 and described in

section 1.2.1. That means the $\boldsymbol{k}$-splitting remains in the zero-field (and hence zero-potential) region. If we apply the aforementioned interpretation of Larmor precession as an interference phenomenon, it would only be consequent to assume Larmor precession also in the absence of any magnetic field. This contradicts the classical view and is what F. Mezei called anomalous or wrong Larmor precession [14].

The behaviour of spin-$1/2$ particles and spinors in time-dependent magnetic fields and the strong connection to interferometry and basic questions of quantum mechanics have been discussed in various publications. We shall not review them here but merely cite some of them in the footnote below for further reading[1]. But the fact that similar problems have been approached in several different ways – concerning the mathematical techniques, assumptions and interpretations – shows that it is imperative to check whether the theoretical construct is compliant with the physical situation. The correctness of the interpretation of the results and whether they actually reflect „reality“ can then only be decided by appropriate and carefully conducted experiments.

In our context we would like to draw attention to the following two aspects:

i) the mathematical model by which the neutron or neutron beam shall be described and

ii) the consequences of the spinor concept, which means we are dealing with two coherently split wave functions.

As opposed to the classical situation, describing the passage of a neutron through the MIEZE setup is not straightforward. Even if we could prepare a single one, the uncertainty principle would only allow for either well-defined energy and momentum, in which case we have no information about its location; or for an exact location, which leaves the momentum undefined. That would render the definition of any well-defined flight times or positions impossible.

The mathematical analogon to this situation is a wave packet with its two extreme forms: a delta function-like peak in space, which means the wave packet is made up of an infinite spectrum of k-vectors, or a plane wave with only one wave vector that is defined at all points in space. Our experiments were conducted at a reactor, which means we used a continuous beam and in that case a plane wave approach seems legitimate. On the other hand, a neutron beam will always feature a specific wavelength distribution (s. section 1.1.4.6), depending on

[1] G. Badurek et al., Neutron interferometric double-resonance experiment. *Phys. Rev. A*, 34:2006-2008, 1986.
A. O. Barut and M. Bozic, On the interpretation of the spinor phase change in a magnetic field in neutron interferometry. *Phys. Lett. A*, 149:431-437, 1990.
R. Golub et al., A plane wave approach to particle beam magnetic resonance. *Am. J. Phys.*, 62:779-87, 1994.
E. Krüger, Acceleration of polarized neutrons by rotating magnetic fields. *Nukleonica*, 25:889-893, 1980.
S. K. Lamoreaux, A review of the experimental tests of quantum mechanics. *Int. J. Mod. Phys.A*, 7:6691-6762, 1992.
F. Mezei, Zeeman energy, interference and neutron spin echo: A minimal theory. *Physica B*, 151:74-81, 1988.
N. F. Ramsey, Complementarity with neutron two-path interferences and separated oscillatory-field resonances. *Phys. Rev. A*, 48:80-82, 1993.
Ch. Schwink and O. Schärpf, Solution of the Pauli equation for neutrons in varying magnetic fields and its application to reflection and transmission of helical magnetic structures. *Z. Phys. B*, 21:305-311, 1975.
J. Summhammer, Coherent multiphoton exchange between a neutron and an oscillating magnetic field, *Phys. Rev. A*, 47:556-565, 1993.

the monochromator. Therefore, the wave packet should provide an appropriate model. We will address this aspect in section 4.1.1.

An interesting question is what does the assumed coherent splitting into two sub-waves – with different $\boldsymbol{k}$ and ω – implicate in terms of the measurability and localization of the neutron wave function. Do we create an entangled state, is the wave function delocalized and is there an upper limit for the separation from that on a positive superposition becomes impossible? In [15] the authors describe the interferometric properties of a MIEZE spectrometer and propose a combination of MIEZE and a Mach-Zehnder interferometer, thus building an interferometer in time and space.

Strongly connected to these aspects is the verification of the longitudinal Stern-Gerlach effect, that is, the splitting of spin-up and spin-down in time as opposed to the spatial separation happening in the „traditional“ Stern-Gerlach effect. The Multi-MIEZE technique can provide experimental means for this, we will come back to that and closely related points and in more detail in sections 1.4, 4.1.1, and 4.2.4.

From the quantum mechanical point of view, the most elaborate treatment of NRSE/MIEZE has probably been given by Golub et al. in [13], using a plane wave approach. They start with the solution of Krüger's problem [16], which consists in finding the solution for a neutron beam passing through an indefinitely expanded static field with a perpendicular rotating field in a confined region, and apply their results to NRSE and MIEZE.

Our treatment differs in some respects. We will make use of the time-evolution operators we derived in the previous sections and we will assume different flight times for the two states, according to the fact that they do have different k-vectors. Many publications about MIEZE calculate the points in time or neutron flight times under the assumption that spin-up and spin-down travel at the same velocity $v = v_0$. This appears inconsequent given the fact that when neglecting relativistic effects – which is legitimate considering the velocities involved – wave vector k and velocity v are proportional.

That raises the question of how one defines a point of arrival or flight time for a plain wave, which is infinitely expanded? We will imply that we chose one particular point on the wave train, i.e. take a „snapshot“ of the phase at time t_0, and use that as a reference point for investigating how the phase of the state changes over time.

In the upcoming formulae we will introduce various differently indexed variables, and in order to provide an easy-to-read overview we summarized them in Table 1.1. In addition to Fig. 1.7 (which shows the energy levels), Fig. 1.8 gives another schematic overview for a single coil MIEZE setup, containing all relevant variables as a further aid for the reader.

The resonance condition, i.e. RF frequency equals Larmor frequency, does not depend on the wavelength of the incoming neutron, but the π-flip condition does. If we presume that at the coil boundaries the kinetic energies split due to exchange of quanta $\hbar\omega$, the two waves travel within the field at different velocities

$$v^{\pm} = v_0 \sqrt{1 \pm \frac{\omega}{\omega_0}} \approx v_0 \left(1 \pm \frac{\omega}{2\,\omega_0}\right) . \tag{1.139}$$

The π-flip condition $\omega_{\mathsf{A}} \cdot D/v = \omega_{\mathsf{A}} \cdot \Delta t = \pi$ can only be fulfilled for a particular velocity. The

Variable	Meaning
t_0	Time when entering the first coil (equal for both spin states)
t_1^+, t_1^-	Time when leaving the first coil for spin-up ($^+$) and spin-down ($^-$)
t_{12}^+, t_{12}^-	Time when entering the second coil
t_2^+, t_2^-	Time when leaving the second coil
t_D^+, t_D^-, t_D	Time at the detector
v_0	Initial velocity of the matter wave (equal for both spin states)
v_1^+, v_1^-	Velocity in the first coil for spin-up ($^+$) and spin-down ($^-$)
v_{12}^+, v_{12}^-	Velocities between the coils
v_2^+, v_2^-	Velocities in the second coil
v_D^+, v_D^-	Velocities between second coil and detector
ω_0	Initial matter wave frequency (equal for both spin states)
ω_1^+, ω_1^-	Matter wave frequencies at $t_1^\pm$
ω_{12}^+, ω_{12}^-	Matter wave frequencies at $t_{12}^\pm$
ω_2^+, ω_2^-	Matter wave frequencies at $t_2^\pm$
ω_D^+, ω_D^-	Matter wave frequencies at $t_D^\pm$
ω_A	HF frequency of the first coil
ω_B	HF frequency of the second coil
U_1	Time-evolution operator for the first coil
U_2	Time-evolution operator for the second coil
L_1	Distance between first and second coil
L_2	Distance between second coil and detector
D	Thickness of the coil

Table 1.1: Definitions of variables for the quantum mechanical MIEZE calculations (see also Figs. 1.7 and 1.8).

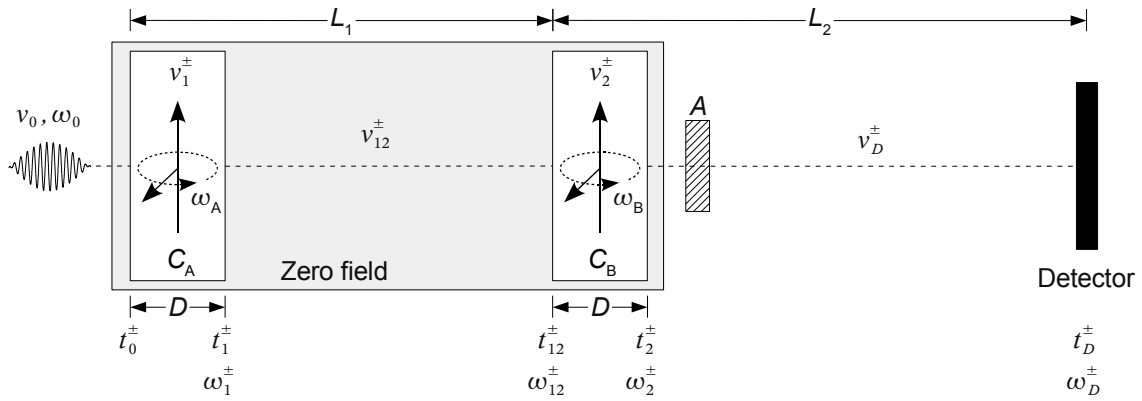

Figure 1.8: Single coil MIEZE setup, definition of variables.

time-evolution operator for a coil that is tuned to resonance reads

$$U(t,t') = \mathrm{e}^{-\frac{i}{\hbar}\mathcal{H}_0(t-t')} \times \begin{pmatrix} \cos\left(\frac{\omega_1}{2}(t-t')\right)\mathrm{e}^{-i\frac{\omega}{2}(t-t')} & -i\sin\left(\frac{\omega_1}{2}(t-t')\right)\mathrm{e}^{-i\left(\frac{\omega}{2}(t-t')-\varphi\right)} \\ -i\sin\left(\frac{\omega_1}{2}(t-t')\right)\mathrm{e}^{i\left(\frac{\omega}{2}(t-t')-\varphi\right)} & \cos\left(\frac{\omega_1}{2}(t-t')\right)\mathrm{e}^{i\frac{\omega}{2}(t-t')} \end{pmatrix} . \quad (1.140)$$

The diagonal elements of U can in principle only vanish for one of the states, i.e. a specific velocity or wave vector. That, on the other hand, would complicate the formal treatment to a degree which does not support the objective of demonstrating the MIEZE working principle. We therefore will assume that the π-flip condition does hold for both partial waves, and $U(t,t')$ takes on the simpler form

$$U(t,t') = \mathrm{e}^{-\frac{i}{\hbar}\mathcal{H}_0(t-t')} \begin{pmatrix} 0 & -i\,\mathrm{e}^{-i\left(\frac{\omega}{2}(t-t')-\varphi\right)} \\ -i\,\mathrm{e}^{i\left(\frac{\omega}{2}(t-t')-\varphi\right)} & 0 \end{pmatrix} . \quad (1.141)$$

We presume this in the light of the fact that the matter wave frequency ω_0 is normally much larger than the frequencies of the RF fields,

$$\omega_{\mathrm{A,B}} \ll \omega_0 . \quad (1.142)$$

This is the case for the wavelengths and RF fields used in our experiments, so we will consider the approximation to be true throughout the work.

Since the coils C_A and C_B of a MIEZE instrument are operated at different frequencies, the HF phases consequently do not have a static relation for all times in general. That means the phase difference $\varphi_2 - \varphi_1$ is not constant for any neutron in the beam, or in other words, for all wave phases at a specific time (as it is for NRSE). Therefore we must consider the times at which the spin states arrive at the coils, as can be seen from Table 1.1 we called them $t_0^\pm$ and $t_{12}^\pm$. Hence, the initial phases are

$$\varphi_1 = \omega_\mathrm{A}\, t_0 , \qquad \varphi_2 = \omega_\mathrm{B}\, t_{12} . \quad (1.143)$$

Since the π-flip condition shall hold for both states, we best proceed by investigating the two partial waves of the incoming beam separately, i.e. the two cases

$$\psi_0 = \begin{bmatrix} \psi_0^+ \\ 0 \end{bmatrix} = \frac{-i}{\sqrt{2}}\begin{bmatrix} 1 \\ 0 \end{bmatrix} \qquad \text{and} \qquad \psi_0 = \begin{bmatrix} 0 \\ \psi_0^- \end{bmatrix} = \frac{-i}{\sqrt{2}}\begin{bmatrix} 0 \\ 1 \end{bmatrix} .$$

With our definition of the variables and the representation for the time-evolution operator, we obtain for the spin-up state after the first coil at time t_1

$$\psi_1^+(t_1^+) = U_1(t_1^+, t_0)\begin{bmatrix} \psi_0^+ \\ 0 \end{bmatrix} = \frac{-i}{\sqrt{2}}\begin{bmatrix} 0 \\ \mathrm{e}^{-i\,\omega_\mathrm{A}\left(\frac{D}{2v_1^+} - t_1^+\right)} \end{bmatrix} . \quad (1.144)$$

We see again the complete inversion of population due to resonance and π-flip condition.

Between the coils we have zero-field and hence no magnetic potential. Therefore, the state does not accumulate any additional phase and by replacing t_1 by t_{12} and the flight time from the exit of the first to the origin of the second coil, we find

$$\psi_{12^+}^+(t_{12}^+) = \frac{-i}{\sqrt{2}}\begin{bmatrix} 0 \\ \mathrm{e}^{-i\,\omega_\mathrm{A}\left(\frac{D}{2v_1^+} - \left(t_{12}^+ - \frac{L_1 - D}{v_{12}^+}\right)\right)} \end{bmatrix} , \quad (1.145)$$

This is equivalent to the technique of transferring the output of coil A to a coordinate system with origin at coil B, used by Golub et al. in [13].

The time-evolution operator U_2 of the second coil – which is likewise tuned to resonance and π-flip – is equivalent to that of the first, but we have to consider the exchange of states. So after the second coil, the state is

$$\psi_2^+(t_2^+) = U_2(t_2^+, t_{12}^+)\,\psi_{12}^+ = \frac{-1}{\sqrt{2}} \begin{bmatrix} \mathrm{e}^{-i\left[(\omega_\mathrm{A}-\frac{\omega_\mathrm{B}}{2})\frac{D}{v_2^+}+\omega_\mathrm{A}(\frac{D}{2v_1^+}-\frac{D}{v_{12}^+})+\omega_\mathrm{A}\frac{L_1}{v_{12}^+}+(\omega_\mathrm{B}-\omega_\mathrm{A})t_2^+\right]} \\ 0 \end{bmatrix} . \tag{1.146}$$

For NRSE, ω_A and ω_B are equal and with the approximation that $v_\mathrm{i}^+ \approx v_0$ we see that the time-dependence vanishes and we can immediately derive the result we already gave in Eq. (1.134):

$$\Delta\varphi = \frac{2L_1\omega}{v_0} . \tag{1.147}$$

But the MIEZE instrument produces a state with a time-dependent phase, which means a non-cancelling kinetic energy splitting after the coil. At a certain point L_2, where we place the detector, a time-dependent, intensity-modulated, high-frequency signal is created after passing the beam through a polarization analyser (whose function will be addressed in the next section). The spin-up state after time t_D^+ reads

$$\psi_\mathrm{D}^+(t_\mathrm{D}^+) = \frac{-1}{\sqrt{2}} \begin{bmatrix} \mathrm{e}^{-i\left[(\omega_\mathrm{A}-\frac{\omega_\mathrm{B}}{2})\frac{D}{v_2^+}+\omega_\mathrm{A}(\frac{D}{2v_1^+}-\frac{D}{v_{12}^+})+\omega_\mathrm{A}\frac{L_1}{v_{12}^+}+(\omega_\mathrm{A}-\omega_\mathrm{B})\frac{L_2-D}{v_\mathrm{D}^+}+(\omega_\mathrm{B}-\omega_\mathrm{A})t_\mathrm{D}^+\right]} \\ 0 \end{bmatrix} \equiv \begin{bmatrix} \mathrm{e}^{i\varphi_\mathrm{D}^+} \\ 0 \end{bmatrix} \tag{1.148}$$

In the same way we obtain for spin-down:

$$\psi_\mathrm{D}^-(t_\mathrm{D}^-) = \frac{-1}{\sqrt{2}} \begin{bmatrix} 0 \\ \mathrm{e}^{i\left[(\omega_\mathrm{A}-\frac{\omega_\mathrm{B}}{2})\frac{D}{v_2^-}+\omega_\mathrm{A}(\frac{D}{2v_1^-}-\frac{D}{v_{12}^-})+\omega_\mathrm{A}\frac{L_1}{v_{12}^-}+(\omega_\mathrm{A}-\omega_\mathrm{B})\frac{L_2-D}{v_\mathrm{D}^-}+(\omega_\mathrm{B}-\omega_\mathrm{A})t_\mathrm{D}^-\right]} \end{bmatrix} \equiv \begin{bmatrix} 0 \\ \mathrm{e}^{i\varphi_\mathrm{D}^-} \end{bmatrix} \tag{1.149}$$

For an arbitrary distance L_2, the two states do not necessarily arrive simultaneously, but at times

$$t_\mathrm{D}^\pm = t_0 + D\left(\frac{1}{v_1^\pm}+\frac{1}{v_2^\pm}\right) + (L_1-D)\frac{1}{v_{12}^\pm} + (L_2-D)\frac{1}{v_D^\pm} \tag{1.150}$$

with a time difference

$$\Delta t_\mathrm{D} = t_\mathrm{D}^+ - t_\mathrm{D}^- . \tag{1.151}$$

By expressing t_D^- with t_D^+ and Δt_D and setting $t_\mathrm{D} \equiv t_\mathrm{D}^+$, we define the point of arrival to be equal for both partial waves. We now replace all velocities by expressions similar to Eq. (1.139), which yields

$$\begin{aligned} v_1^\pm &\approx v_0\left(1 \pm \frac{\omega_\mathrm{A}/2}{2\,\omega_0}\right) , \quad v_{12}^\pm \approx v_0\left(1 \pm \frac{\omega_\mathrm{A}}{2\,\omega_0}\right) \\ v_2^\pm &\approx v_0\left(1 \pm \frac{\omega_\mathrm{A}-\omega_\mathrm{B}/2}{2\,\omega_0}\right) , \quad v_\mathrm{D}^\pm \approx v_0\left(1 \pm \frac{\omega_\mathrm{A}-\omega_\mathrm{B}}{2\,\omega_0}\right) \end{aligned} \tag{1.152}$$

In order to obtain pure beats in time at the detector, all constant terms in the difference between the phases

$$\Delta\varphi_\mathrm{D}(t_\mathrm{D}) = |\varphi_\mathrm{D}^+(t_\mathrm{D}) - \varphi_\mathrm{D}^-(t_\mathrm{D})| \tag{1.153}$$

must vanish. The time derivation of $\Delta\varphi_\mathrm{D}$ (cp. Appendix A.2), i.e. the signal modulation frequency ω_M of the signal is

$$\frac{\mathrm{d}}{\mathrm{d}t_\mathrm{D}}\Delta\varphi_\mathrm{D} = 2\left(|\omega_\mathrm{B} - \omega_\mathrm{A}|\right) \equiv \omega_\mathrm{M}\ . \tag{1.154}$$

We find that in order to have pure beats in time, i.e. $\Delta\varphi_\mathrm{D} = 2(|\omega_\mathrm{B} - \omega_\mathrm{A}|)t_\mathrm{D}$, the following relation between frequencies and distances must hold:

$$\begin{aligned} L_1 = &\frac{D}{2}\left(\underbrace{\frac{1+\frac{\omega_\mathrm{A}^2}{8\,\omega_0^2}}{1-\frac{\omega_\mathrm{A}^2}{16\,\omega_0^2}}}_{\approx 1 \text{ for } \omega_0 \gg \omega_\mathrm{A},\,\omega_\mathrm{B}} + \frac{\omega_\mathrm{B} - 2\,\omega_\mathrm{A}}{\omega_\mathrm{A}} \cdot \underbrace{\frac{1-\frac{\omega_\mathrm{A}^2}{4\omega_0^2}}{1-\frac{(\omega_\mathrm{B}-2\,\omega_\mathrm{A})^2}{16\,\omega_0^2}}}_{\approx 1 \text{ for } \omega_0 \gg \omega_\mathrm{A},\,\omega_\mathrm{B}}\right) + \\ &(L_2 - D) \cdot \frac{\omega_\mathrm{B} - \omega_\mathrm{A}}{\omega_\mathrm{A}} \cdot \underbrace{\frac{1-\frac{\omega_\mathrm{A}^2}{4\,\omega_0^2}}{1-\frac{(\omega_\mathrm{B}-\omega_\mathrm{A})^2}{4\,\omega_0^2}}}_{\approx 1 \text{ for } \omega_0 \gg \omega_\mathrm{A},\,\omega_\mathrm{B}} \end{aligned} \tag{1.155}$$

With our assumption Eq. (1.142), all terms containing $\omega_{\mathrm{A,B}}/\omega_0$ are much smaller than 1, and Eq. (1.155) then takes the form of the classical, wavelength-independent MIEZE condition

$$\frac{L_1}{L_2 - D/2} = \frac{\omega_\mathrm{B}}{\omega_\mathrm{A}} - 1\ . \tag{1.156}$$

Many publications about MIEZE neglect the coil thickness D in the derivation of this expression for simplicity, which is normally justified since $L_{1,2}$ are usually much larger than D. With our definitions of the coil and detector distances (cp. Fig. 1.8), the classical result we obtained in Eq. (1.156) is in agreement with those from previous calculations (e.g. [4], [13] or [17]).

However, we see that the MIEZE condition – i.e. the relation determining the position where the coherence volumina interfere and we place our detector – is in principle slightly dependent on the neutron energy. For very high fields/frequencies the approximation Eq. (1.142) might not be appropriate any more and a decrease in polarization would become noticeable.

A comment seems to be indicated at this point. Our *time*-evolution operator, which we apply to a general spin state $(1, 1)$, gives the quantum mechanical state at a certain time t, based on a known state at time t'. It does not make any statement about a corresponding point in *space*. For our (one-dimensional) treatment we have linked the points in space, i.e. the coil and detector positions of a MIEZE setup, with points in time by the group velocities of the spin states. But from the viewpoint of a quantum mechanical measurement, time and space can be chosen arbitrarily: to obtain information about the „physical reality“ (i.e. evaluating $\langle\psi|\,\widehat{O}\,|\psi\rangle$ for the operator $\widehat{O}$ of a given physical quantity) at, say, the position of coil 2, we would have to place our measuring apparatus there and perform a measurement at time t, which yields a value for the quantity to be measured with a certain probability given by the probability amplitude at that time t.

This is a basic difference to Golub et al.'s plane wave approach, which does not require propagation times, since a plane wave is defined in total space with equal probability. The k-vectors and energy are investigated in space regions defined by the coil and detector positions. This,

however, attributes different k's and ω's in different space regions to an in principle indefinitely expanded wave.

Finally, we want to derive the expression for the corresponding polarization vector at the detector. We could of course do that by applying Eqs. (1.110)-(1.112) and calculating

$$\begin{pmatrix} 2\,\Re(\psi^{-*}\psi^{+}) \\ -2\,\Im(\psi^{-*}\psi^{+}) \\ |\psi^{+}|^2 - |\psi^{-}|^2 \end{pmatrix} , \tag{1.157}$$

but we must keep in mind that this would only give us the polarization of a pure state. For an initial polarization $\boldsymbol{P}_0 = (0, P_{0\mathrm{y}}, 0)$, we can make use of our results in section 1.1.4.1 and apply the expression for $\boldsymbol{P}$ in Eq. (1.80) to both coils consecutively.

As usual, we will assume both coils to be tuned to meet the resonance as well as the π-flip condition. With Eq. (1.156) the trivial calculation yields for the polarization vector at the detector the expected result

$$\boldsymbol{P}_{\mathrm{D}} = \begin{pmatrix} P_{0\mathrm{y}} \sin(2\,(\omega_{\mathrm{B}} - \omega_{\mathrm{A}})t_{\mathrm{D}}) \\ P_{0\mathrm{y}} \cos(2\,(\omega_{\mathrm{B}} - \omega_{\mathrm{A}})t_{\mathrm{D}}) \\ 0 \end{pmatrix} . \tag{1.158}$$

In the here demonstrated ideal case, $\boldsymbol{P}$ still lies in the x-y plane after two π-flips, rotating with an angular frequency of $2\,(\omega_{\mathrm{B}} - \omega_{\mathrm{A}})$.

As a concluding remark for this section, we like to point out the difference between the concept of polarization, which we elaborated on in the previous sections, and the treatment of the neutron as a matter wave.

Although the polarization $\boldsymbol{P}$ can be defined for a single neutron by the direction of its spin vector (Eq. (1.16)), it makes more sense to see it as an ensemble average of the neutron beam, measured or analyzed at a certain position or certain time. The polarization is calculated via *time*-evolution operators and since the points in space (coil and detector positions) are given, we need a measure for how fast those defined positions are reached. It makes sense to use the average wavelenth λ_0 or neutron velocity v_0 for that purpose, but in contrast to the wave function formalism, that velocity is not assigned to a specific state or particle.

In the case of a matter wave we are treating its wave function with the quantum mechanical formalism, which implies that we have a physical picture of the neutron according to its nature as a quantum mechanical particle. This picture is expressed by the formal mathematical construct of the wave function. The wavelength/velocity/k-vector is therefore a property of the investigated state.

In order to have a reproducible way to check the derived results in this chapter and to be able to repeat them with different parameters, the calculations have been performed with the help of Mathematica™, a mathematics software for numeric and symbolic computation. The scripts used to deduce the presentation of the spinor for the MIEZE instrument and the MIEZE condition are attached in Appendix A.2.

1.3.1 Measuring with MIEZE

1.3.1.1 The Beam Intensity of a MIEZE Signal after the Analyzer

The purpose of the polarization analyzer after the second coil might not be obvious at first glance. Its involvement is necessary to actually obtain the intensity-modulated signal that can be measured time-resolved with a fast scintillation detector. Our analyzer is a supermirror bender, whose working principle was already explained in section 1.1.5. There we have defined the z-axis to be the direction of polarization analysis, which is the case in the actual experiments. The polarization vector, however, is leaving the second flipper coil of the MIEZE setup in the x-y-plane. Only after passing the coupling coils it is rotated into the x-z-plane, which is necessary as we need a defined way of leading the polarization from the inside of the zero-field region to the outside. For the following theoretical derivation of the beam intensity we do not consider the coupling coil.

The analyzer will only let the $\sigma_\mathsf{y} = +1$ wave pass, but the effect is probably more straightforward to comprehend when looking at the polarization vector Eq. (1.158). After the second MIEZE coil $\boldsymbol{P}$ is rotating in the x-y-plane, and if the bender is aligned to analyze in $+y$-direction, the transmission probability reads

$$T = \frac{1}{2}\left(1 + \cos\varphi_\mathsf{D}\right) = \frac{1}{2}\left(1 + \cos[2\left(\omega_\mathsf{B} - \omega_\mathsf{A}\right)t_\mathsf{D}]\right) = \cos^2[(\omega_\mathsf{B} - \omega_\mathsf{A})t_\mathsf{D}] \tag{1.159}$$

If the incoming intensity was I_0, the intensity at the detector yields

$$I(t_\mathsf{D}) = \frac{I_0}{2}\left(1 + \cos[2\left(\omega_\mathsf{B} - \omega_\mathsf{A}\right)t_\mathsf{D}]\right) = I_0\,\cos^2[(\omega_\mathsf{B} - \omega_\mathsf{A})t_\mathsf{D}]\,, \tag{1.160}$$

and we obtain an intensity modulated, sinusoidal signal with a frequency of $2(\omega_\mathsf{B} - \omega_\mathsf{A})$.

1.3.1.2 The Spinecho Time Analogon for MIEZE

As already mentioned in section 1.1.5, in MIEZE measurements the polarization of the signal is replaced by the contrast C, which is determined by the maximum and minimum count rates I_max and I_min of the oscillating intensity $I(t_\mathsf{D})$ according to Eq. (1.116).

The scattering function can be obtained analogously to NSE (compare section 1.2, Eqs. (1.126, 1.127) and [4]):

$$C \sim \int_0^\infty S(\boldsymbol{Q}, \omega_\mathsf{s}) \cos(\omega_\mathsf{s}\tau_\mathsf{M} - \overline{\omega}_\mathsf{s}\tau_\mathsf{M})\,\mathrm{d}\omega_\mathsf{s} = S(\boldsymbol{Q}, \tau_\mathsf{M})\,. \tag{1.161}$$

The Fourier or MIEZE time τ_M is

$$\tau_\mathsf{M} = \omega_\mathsf{M}\,\frac{\hbar L_2}{m\,v_0^3}\,, \tag{1.162}$$

with L_2 being the detector distance. The modulation frequency of the signal is

$$\omega_\mathsf{M} = 2N(\omega_\mathsf{B} - \omega_\mathsf{A})\,, \tag{1.163}$$

where N is the number of coils in the bootstrap resonance flipper. For double bootstrap flippers ω_M can be in the MHz range. For a coils distance of 1 m and frequencies of $\omega_\mathsf{A} = 600$ kHz and $\omega_\mathsf{B} = 800$ kHz, the detector distance is 3 m from the second coil. These parameters would yield a MIEZE time $\tau_\mathsf{M} \approx 35$ ns for 10 Å neutrons, which corresponds to an energy resolution of approx. 19 neV.

1.3.1.3 The Detection Range of a MIEZE Signal

The distance within which a time-dependent intensity modulation is detectable depends on the average wavelength λ_0 of the neutron beam and the longitudinal coherence length l_c.

l_c is the distance at which two waves start to be out of phase and are hence unable to interfere. For a stationary neutron beam with a wave vector distribution $g(k)$ this is usually defined when the coherence function $\Gamma(\boldsymbol{r}-\boldsymbol{r}') = \int g(k)\,\mathrm{e}^{ik(\vec{r}-\vec{r}')}\mathrm{d}k$ has dropped to a value $1/e$ [18]. In analogy to photon optics, the longitudinal coherence length of a neutron beam can be written as [19]

$$l_\mathrm{c} = \frac{\lambda_0^2}{\Delta\lambda}\,, \tag{1.164}$$

with $\Delta\lambda$ being the characteristic width of the wavelength distribution.

The coherence volumina of spin-up and spin-down must overlap to interfere, in which case we are able to measure the MIEZE signal. That overlapping happens within a certain range L_M around the MIEZE point at L_2, which is determined by Eq. (1.156). The range depends on l_c, the average wave packet velocity v_0, and the velocity difference Δv between the spin-up and spin-down states (which in turn depends on the RF coil frequencies).

As a side note we should mention that the longitudinal coherence length of coherently split propagating wave packets is constant over time, despite the fact that they spread during their propagation and the dispersion can result in an overlap of the amplitudes. This has been stated by [20] and is in accordance with the concept of the collapse of the wave function (or reduction of the wave packet) when a quantum mechanical particle is observed, i.e. measured.

By expressing the longitudinal coherence length with the flight time T from $L_2 - L_\mathrm{M}/2$ to L_2, we obtain $l_\mathrm{c} = T\,\Delta v \approx L_\mathrm{M}/2 \cdot \frac{\Delta v}{v_0}$. With Eqs. (1.152) and (1.164) follows

$$L_\mathrm{M} \approx 2\,l_\mathrm{c}\,\frac{v_0}{\Delta v} \approx 2\,l_\mathrm{c}\,\frac{\omega_0}{|\omega_\mathrm{B}-\omega_\mathrm{A}|} = \frac{2\pi\,h}{m}\,\frac{1}{\Delta\lambda\,|\omega_\mathrm{B}-\omega_\mathrm{A}|}\,. \tag{1.165}$$

For a 10 Å neutron beam with a typical relative wavelength distribution of $\Delta\lambda/\lambda_0 \approx 10\%$ and a frequency difference of 100 kHz, the oscillations of a MIEZE signal are supposed to be detectable in a range of $L_\mathrm{M} \approx 4$ cm under ideal conditions.

1.4 Multi-level MIEZE

What happens when multiple MIEZE setups are serially stacked, i.e. the time-dependent, intensity modulated signal of a first MIEZE assembly is fed into a second? This is one of the key questions the thesis at hand is concerned with. The schematic instrument setup is sketched in Fig. 1.9. All MIEZE levels must be tuned to have a common velocity focussing point, i.e. the same detector position.

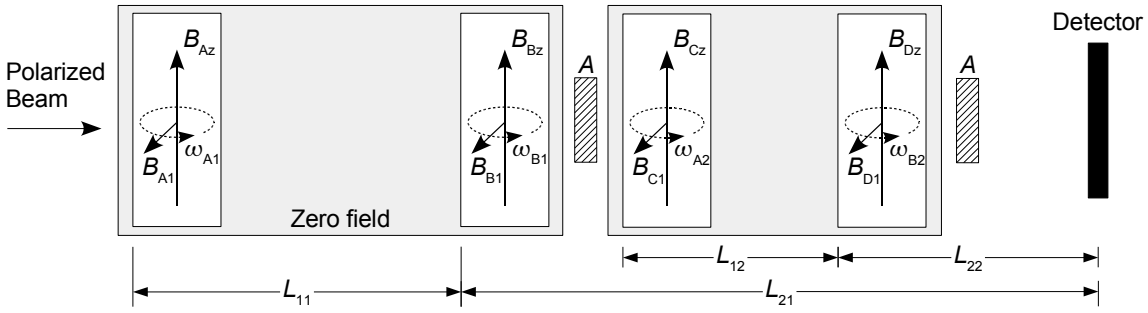

Figure 1.9: Principle setup of a two-level Multi-MIEZE instrument.

The time-dependent intensity function for an n-level Multi-MIEZE is assumed to be the product of the individual intensity distributions, i.e. a beat of the signals produced by each single MIEZE setup. This assumption is based on the fact that the intensity modulation of the signal of each setup at the detector position is a function of the arrival time t_D [3]. Therefore, every MIEZE stage has a time-dependent transmission probability and the total intensity of a Multi-MIEZE instrument can be written as the product of the respective transmission functions:

$$I_{MM}(t_D) = I_0\, T_{MM} = I_0 \prod_{\nu} T_\nu \ , \tag{1.166}$$

with T_ν as in Eq. (1.159).
In the following we assume that each MIEZE is operated with bootstrap coils, thus according to section 1.2.1.3 the phase difference and consequently the signal frequency are increased by a factor of N. We define

$$\omega_{M\nu} = 2N(|\omega_{B\nu} - \omega_{A\nu}|) \ , \tag{1.167}$$

for the νth setup and assume that $\omega_{M\nu}$ differs for subsequent setups by a factor F_M, i.e.

$$\omega_{M(\nu+1)} = F_M\, \omega_{M\nu} \ . \tag{1.168}$$

With Eqs. (1.159) and (1.160), the intensity of an ideal Multi-MIEZE instrument after n setups can then be

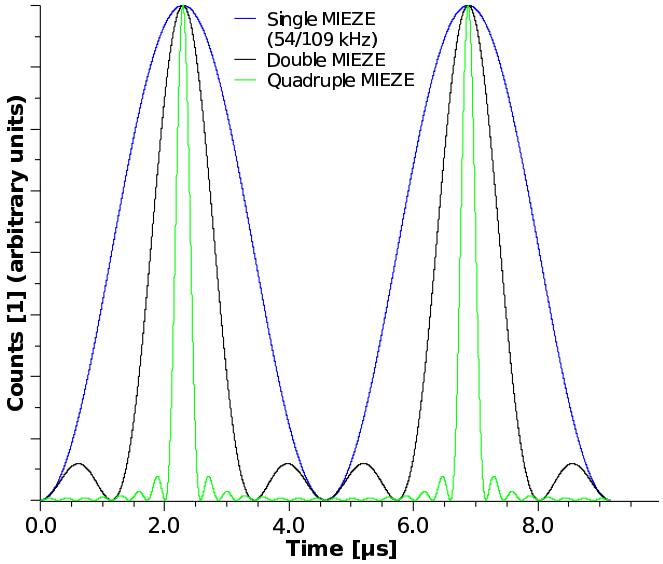

Figure 1.10: Ideal intensity distributions of a single (blue), double (black), and quadruple (green) MIEZE setup ($F_M = 2$, $N = 2$, $\omega_{M1} = 2N \cdot 2\pi \cdot 54.5$ kHz).

described by

$$I_{\mathsf{MM}}(t_{\mathsf{D}}) = I_0 \prod_{\nu=1}^{n} \cos^2\Big(\frac{1}{2}\, F_{\mathsf{M}}^{\nu-1}\, \omega_{\mathsf{M1}}\, t_{\mathsf{D}} + \varphi_\nu\Big) \tag{1.169}$$

$$= I_0 \prod_{\nu=1}^{n} \frac{1}{2}\left[1 + \cos(F_{\mathsf{M}}^{\nu-1}\, \omega_{\mathsf{M1}}\, t_{\mathsf{D}} + \widetilde{\varphi}_\nu)\right] . \tag{1.170}$$

The phases $\varphi_\nu/\widetilde{\varphi}_\nu$ depend on the choice of F_{M} as well as the instrument geometry and must be adjusted such that the peak maxima overlap and positive superposition is achieved. As we will see later, this can be done experimentally by tuning the phases φ_ν via the RF synthesizers, which are producing the sinusoidal signal fed into the RF oscillating circuits.

Fig. 1.10 shows the calculated signals for ideal single ($n = 1$), double ($n = 2$), and quadruple ($n = 4$) bootstrap MIEZE setups with a MIEZE factor $F_{\mathsf{M}} = 2$ and $\omega_{\mathsf{M}\nu} = 2N \cdot 2\pi \cdot 54.5$ kHz. These settings were also used in the experiments.

The parameters which influence the Multi-MIEZE signal shape, its frequency and the pulse width are N, n, F_{M}, and ω_{M1}. They can be chosen and tuned to obtain a signal with specific characteristics:

The basic signal frequency of the main peaks is that of the first stage ω_{M1}, as follows also from Eq. (1.170). In the ideal case, there is no loss of contrast.

The width of the main peaks sharpens, the degree depending on the number of MIEZE levels n, and on the RF frequencies. The higher the initial frequency ω_{A1}, the narrower will the resulting width of the Multi-MIEZE peaks be. Increasing the factor F_{M}, i.e. the frequency differences $\omega_{\mathsf{M}\nu}$ of the subsequent levels, will enhance the sharpening effect.

To achieve a large separation in time of the neutron pulses, the frequency difference ω_{M1} of the first level must be small, as it defines the Multi-MIEZE signal frequency.

Finally, running the resonance flipper coils in bootstrap mode ($N > 1$) will increase the signal frequency by a factor N.

In principle F_{M} can be an arbitrary integral number as long as the phases φ_ν are set correctly. However, due to the nature of the cosine function a value of $F_{\mathsf{M}} = 2$ seems preferable. It results in a beating that has only very weakly pronounced side maxima (cp. Fig. 1.10) and relaxes the technical limits, i.e. the applicable frequencies and number of MIEZE levels.

One of the main goals was to verify the Multi-MIEZE principle, i.e. its nature as a beat of several time-dependent intensity distributions as described by Eq. (1.170), and the resulting predicted sharpening of the main signal peaks. As will be elaborated on in the next chapters, this was done using a two-level setup and the obtained data were fitted with a function according to Eq. (1.170).

An instrument based on Multi-MIEZE would rather represent a high resolution TOF spectrometer, measuring $S(\boldsymbol{Q}, \omega)$ instead of $S(\boldsymbol{Q}, t)$ like spin echo-based instruments do. The resolution would be given by the peak width, with the dynamic range being defined by the peak separation. A discussion of possible applications of a Multi-MIEZE spectrometer in science will follow in chapter 4.

1.4.1 The Contrast of a Multi-MIEZE Signal

The definitions of polarization P or contrast C as they were given by Eqs. (1.115) and (1.116) are not directly applicable for a Multi-MIEZE signal in this form. The latter is a beating of several sinusoidal signals and hence has multiple local minima and maxima. Therefore, we would like to propose a definition that is appropriate for the nature of the signal and able to provide information about its quality.

We should start with a few remarks about possible scenarios of how the signal can be produced and what parameters influence its quality: A MIEZE factor $F_{\mathrm{M}} = 2$ produces a signal beating that has relatively weakly developed side maxima. But we could in principle choose another (integral) factor that results in two main peaks with more complexly structured sidebands.

A wrong phase relation of the single signals can result in a distortion of the Multi-MIEZE signal and hence change the peak height, width, and distance in comparison to the ideal case. In the worst case it will be completely detuned, in section 3.4 we gave an example. In the following we will imply that there is no phase detuning, since such an effect is difficult to quantify and include in the definitions.

The last parameters we are going to considere are the contrasts C_i of the single MIEZE setups. Here we have to distinguish three cases producing different outcomes, which we want to explain with the example of a two-level Multi-MIEZE:

i) The first MIEZE setup is completely detuned ($C_1 = 0$), the second is not ($C_2 > 0$). This will result in a time-dependent intensity modulation at the detector with sideband maxima that are equally high than the main peaks (basically a single MIEZE signal with the modulation frequency and half the intensity of the second level).

ii) The second MIEZE setup is detuned ($C_2 = 0$) and the first is not ($C_1 > 0$). Here we will observe a Multi-MIEZE signal that has no sideband wiggles, but also no peak sharpening (basically a single MIEZE signal with the modulation frequency and half the intensity of the first level).

iii) Both setups are reasonably tuned ($C_{1,2} > 0$).

We see intensity modulations at the detector in all three cases and could therefore define a contrast-like quantity that reflects the difference between maxima and minima. But we also need to have a measure of how much Multi-MIEZE character is actually contained in the signal. Therefore, we introduce the „Multi-MIEZEity“ M of an n-level Multi-MIEZE signal

$$M = \frac{\sum_{i=1}^{n-1}\left(\sqrt{C_i}\cdot\sum_{j=i}^{n}\sqrt{C_j}\right)}{\sum_{k=1}^{n-1}(n-k)}\,. \tag{1.171}$$

What Eq. (1.171) does is calculating the sum of all different products $\sqrt{C_i\,C_j}$ for $i \neq j$ and weighting them with the number of products. Like a contrast, M will take on values between 0 and 1.

If at least $(n-1)$ single MIEZE setups are completely detuned (i.e. $C_i = 0$), the Multi-MIEZE character of the signal will be lost and we obtain $M = 0$, i.e. at least two of n single MIEZE levels must have a contrast $C_{i,j} \neq 0$ to achieve $M > 0$. For a perfect Multi-MIEZE with

$C_i = 1 \,\forall\, i$ we get $M = 1$. To give an example, a three-level Multi-MIEZE setup with contrasts $C_1 = 0.8$, $C_2 = 0.75$, and $C_3 = 0.5$ would have a Multi-MIEZEity $M = 0.67$.

Eq. (1.171) is not based on the count rates actually measured at the detector, but rather on the contrasts of each single MIEZE, which can only be derived from the parameters of a data fit analysis of the signal. As opposed to the definition of the MIEZE contrast Eq. (1.116), which only includes the maximum and minimum in the count rates, Eq. (1.171) considers the beat nature of a Multi-MIEZE signal.

Given its mathematical features, the quantity M can serve as an analogon to the conventional contrast definition and is indeed suitable when comparing Multi-MIEZE setups running with the same frequency factor F_M. But we would like to give an example why the contrast, which should be a measure for the instrument or signal quality, would be different for two Multi-MIEZE setups that both have an ideal „Multi-MIEZEity“ $M = 1$: As mentioned above, we can in principle use an arbitrary MIEZE factor F_M, but this also changes the RF frequencies. Hence, although the polarization in the main peaks is preserved, the sideband structure of the detector signal changes.

For a reasonable definition of the contrast, not only the absolute maximum of the main peaks in comparison to a minimum should be taken into account, but also its relation to the height of the peaks in the sideband. If we defined a contrast based on these criteria, we would get a higher contrast for a signal with stronger suppressed side maxima, although we can have $M = 1$ in both cases.

As we have pointed out above, a Multi-MIEZE setup rather resembles a high-resolution TOF instrument, measuring $S(\boldsymbol{Q}, \omega)$. For the purpose of TOF measurements, the relevant features of the signal are the peak width and their separation. If we define the width as FWHM, we need to know the peak height. This is best defined as the difference between the peak maximum and the first minima appearing on its left and right. A contrast definition based on these requirements could therefore look like

$$C_\mathrm{TOF} = \frac{I_\mathrm{max} - I_\mathrm{min1}}{I_\mathrm{max} + I_\mathrm{min1}}\,, \tag{1.172}$$

where I_max and I_min1 are the aforementioned count rates in the main peak maximum and in the first minimum of the sideband, respectively. C_TOF can be calculated directly from the counting rates of the measured signal and, as opposed to M, it depends strongly on a correct tuning of the phases φ_i of the MIEZE signals. M only considers the contrasts C_i of each MIEZE level, and will give the same value whether or not the Multi-MIEZE setup is properly phase-tuned.

Increasing the frequency factor F_M to values > 2 will on the one hand have the (normally unfavorable) consequence of pronouncing the sideband peaks. On the other hand, this will also narrow the width of the main peaks. Whether avoiding the first or achieving the second effect is more important must be decided according to the application.

2

The Experimental Setup and Devices

As described in chapter 1, the NRSE technique replaces the long static fields of classical spin echo by short field regions in which a static and a resonantly tuned RF field are superposed. Since the phase accumulation in the field should ideally be equal for all neutrons over the beam cross-section, highly homogeneous (static) fields with well-defined borders are necessary. This seems only possible to accomplish with sharp, non-adiabatic field transitions ($0 \leftrightarrow B_0$). Hence, it is unavoidable that the beam penetrates the winding layers of the coil and interacts with the material.

Depending on the area of application and the utilized wavelength of the beam, the coils must be designed appropriately. In the case of MIRA, which is operated at a beamline for very cold neutrons (8–30 Å), certain effects must be taken into account that are of only minor relevance if thermal neutrons would be used:

- Absorption and scattering cross-sections of the coil material.
  Those are in general higher for slow neutrons, which affects e.g. Small Angle Neutron Scattering applications and limits the possible number of coils in the beam.

- The profile of the wire used for winding the coils.
  A rectangular cross sectional profile (i.e. a tape-like wire) instead of a circular wire should be preferred. For the latter the neutron path in the material is not constant, which leads to depolarization. [21] have done calculations on the coil performance using different wire profiles.

- The demands on the manufacturing precision increase.

At the FRM-II three instruments make currently use of the NRSE technique: MIRA, RESEDA [22] and TRISP [23]. For MIRA new resonance flipper coils were developed within the scope of the project of this thesis, with the objective of meeting the above criteria.

In the following sections we explain why a new design was planned instead of adapting the existing one and discuss materials, design and properties of the MIRA coils. Computer aided simulations were performed to investigate and optimize the different approaches.

Furthermore, this chapter covers all components used in the MIEZE and Multi-MIEZE measurements, such as electronic equipment, detector system, polarization analyzers and magnetic shielding.

2.1 The Instrument MIRA

Figure 2.1: The instrument MIRA.

The Multi-level MIEZE measurements have been conducted at MIRA, which is a versatile instrument on the very cold beam line NL6b of the neutron source FRM-II. With neutron wavelengths ranging from 8 to approx. 30 Å (flux $\approx 4 \cdot 10^5$ neutrons/(Å s cm^2) at 10 Å), MIRA is well suited as a testing platform for new instrumental components and methods since the setup can be changed quickly. It is equipped with a fast 2-D PSD detector (1024×1024 pixels, 1×2 mm^2 resolution) and a ^{3}He counter. All measurements can be performed with polarized or non-polarized neutrons. Currently three exchangeable but permanent measuring options are available: reflectometry, Small Angle Neutron Scattering (SANS), and in the near future NRSE/MIEZE.

More information about MIRA can be found at `http://www.frm2.tum.de/mira/` or in the yearly released annual reports of the FRM-II.

2.2 The B_0 Coils

The coils in use at RESEDA and TRISP share a similar design in principle, the main similarity is the usage of an aluminum tape of 8 mm width and 0.5 mm thickness to form the coil windings. For the purpose of electrical insulation, the tape is coated with an aluminum oxide layer that is grown by anodisation. This insulation layer has two process-related properties that are undesirable in conjunction with neutron scattering: i) a significant amount of H_2O is bound in the layer and ii) during the growth process small „spikes“ form in a regular pattern on top of the surface. The first leads to higher absorption and scattering cross-sections, the second causes a small angle scattering background which overlays the signal caused by the sample (see section 2.2.7).

Another factor which led to the decision to conceive new B_0 coils was that the current design required considerable experience on the part of the experimenter when it comes to winding and assembling the coils. The many components (wound coil body, water and air cooling channels, electrical connectors, etc) are composed and assembled in a way (e.g. glued parts) that makes mechanical changes or repairing difficult. Although the fact remains that NRSE resonance flippers will always be delicate and to some extend complicated devices, the new coils were planned to be simpler in design while using more „standardized“ manufacturing processes.

2.2.1 The Principle Coil Design

The design was inspired by work done previously at the Max-Planck Institute for Solid State Physics Stuttgart (group Prof. Dosch) and published in [24]. The windings of the so-called SERGIS coils consist in principle of stacked aluminum sheets in the form of a coil body, which are electrically contacted by small stripes of aluminum foil. The electrical insulation of subsequent layers was ensured by inserting Kapton® foils of the same shape like the aluminum sheets.

The approach seemed promising to us in principle, so starting from there, we saw mainly three issues that had to be investigated or resolved, respectively:

- The electrical contacting method did not seem to be sufficiently reliable and causing problems (e.g. shortcuts).
- The insulation material Kapton® (although an excellent insulator, rigid and suitable for high temperatures) is a polyimide film containing hydrogen, which we wanted to avoid if possible, due to incoherent scattering.
- A sufficient accuracy of the produced static magnetic field had to be ensured. Therefore, finite element simulations of the planned design were conducted (s. section 2.2.8).

The coil winding material must be conductive, i.e. either metallic or a highly doped semiconductor. At the same time, since the neutron beam penetrates the coil material, it should have low absorption and scattering cross sections in the respective neutron wave length range. Initially another approach was considered where the conductor paths are brought onto an insulating substrate (like silicon or sapphire) by sputtering techniques. It was discarded due to the technical complexity and probably insufficient current density.

Doted semiconductors have conductance values still significantly lower than those of metals. Although some of them feature relatively low scattering and absorption cross-sections (like silicon), the cost-benefit ratio seemed too high. Furthermore, lower conductance would have also meant a higher heat load. So the decision was to use a metal conductor.

2.2.2 The Coil Winding Layers

Of all candidate metals, aluminum has by far the most favorable absorption and scattering properties for cold neutrons. Furthermore, the activation by exposure to the neutron beam is relatively low and the gamma radiation produced by nuclear reactions less critical than for e.g. Copper.

There are, however, many alloys available containing traces or significant fractions of additives like Mg, Si, Cu, Mn or Pb. Highly pure Al is in comparison the best electric conductor but would certainly have been too soft to guarantee an easy enough handling and processibility. We therefore chose the standard alloy AlMg3, which seemed to provide the best compromise of neutron transparency, processibility and costs. Also the total bound scattering cross section of magnesium, the main additive for this alloy, is of the same order of magnitude than that of Aluminum (Mg: 3.71 barn, Al: 1.503 barn) [25].

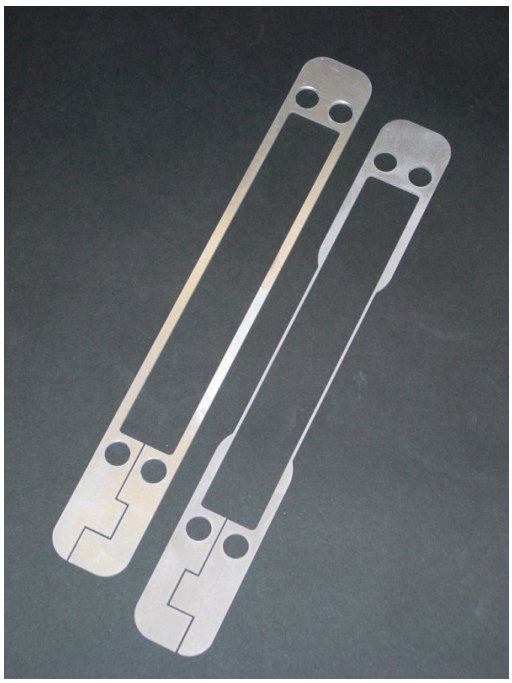

Figure 2.2: Coil windings with neutron window (right) and straight sides (left). They have a thickness of 2 mm.

The winding sheets have a thickness of 2 mm and were produced using wire-cut EDM (supplier: Neutron Science Components (NSC) Germany). This technique combines high accuracy and smooth surfaces, so it was preferred over other alternatives like laser or jet cutting. One disadvantage in comparison

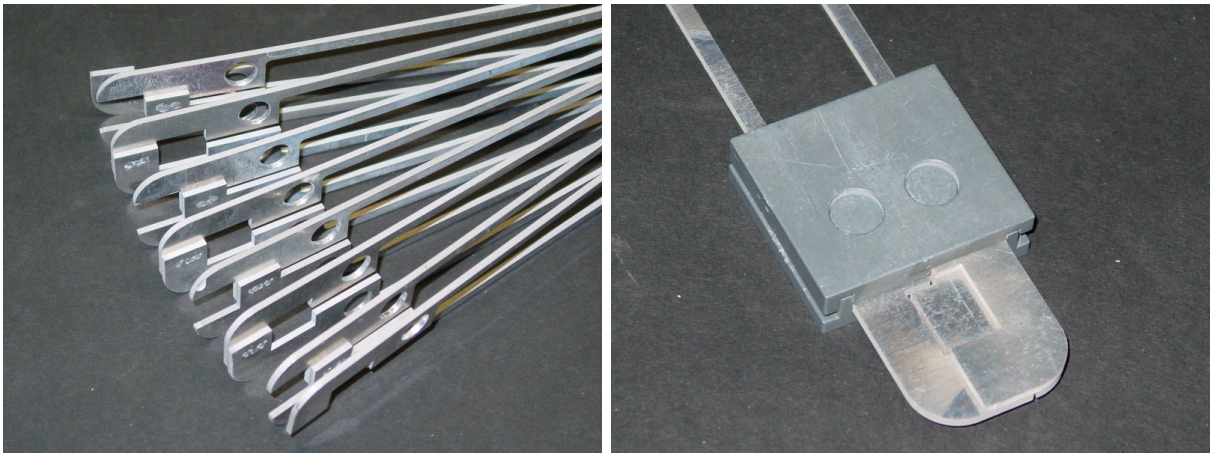

Figure 2.3: Welded coil windings (left), the coil is formed by attaching them with alternating orientations. The accuracy of the spot-welding procedure is ensured by using an alignment clamp (right).

with the latter techniques are higher costs. Fig. 2.2 shows the basic shape of the coil winding layers. They are non-symmetric with respect to the longitudinal axis and have two displaced contact fields at the end. That way, coil windings can be formed by stacking subsequent layers with flipped orientation and contact them at the opposing contact fields (s. Fig. 2.3 (left)). Anodised aluminum pipes will be inserted into the two round holes on either end, acting as cooling channels as well as ensuring proper alignment of the resulting coil body (see section 2.2.4) As depicted in Fig. 2.2 (left), those windings which are directly exposed to the neutron beam have been reduced from initially 4 mm to a width of 1 mm. The advantage is the obviously higher transmission and lower scattering.

A disadvantage is a significantly increased heat production in that area due to the smaller cross-section, which has to be compensated by cooling. We will get back to this issue in section 2.2.5.

Furthermore, to remove the layer of aluminum oxide that has formed in the wire-cutting process, the coil part with the neutron window has been cleaned by etching in sodium hydroxide.

Several methods of contacting two subsequent winding layers were considered. Finally we figured that a solid metallic conjunction would provide the best connection with a low transition resistance. Therefore, the technique of spot-welding was used. Although the welding of aluminum alloys with their excellent heat conduction properties is non-trivial, the welding apparatus (manufacturer: Peco Welding Systems GmbH, model: M90/M2L) could be tuned properly and after several tests we have been able to achieve good results. Fig. 2.4 shows the apparatus with the custom-made copper electrodes, Fig. 2.4.

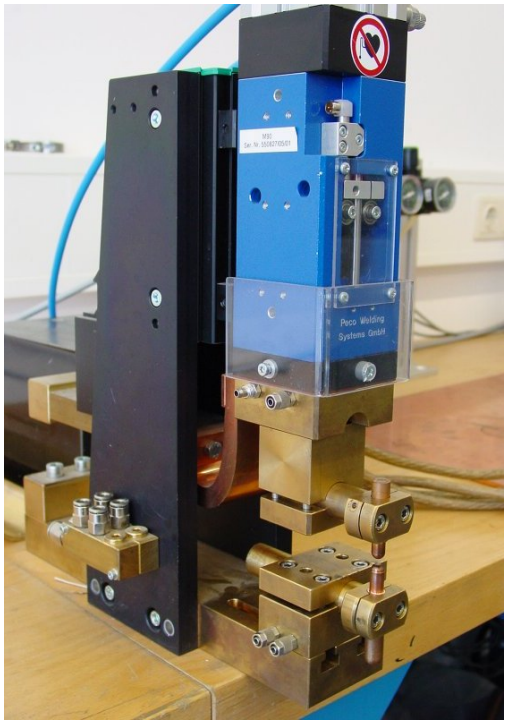

Figure 2.4: The spot-welding apparatus (Peco Welding Systems GmbH, model: M90/M2L) with installed electrodes.

To assure a good alignment during and after the welding procedure, a specially made clamp was used

to hold the aluminum sheets (Fig. 2.3 (right)). In that fashion stacks of approx. 25 windings each were produced, which in a final step were then connected to form the whole coil.

2.2.3 The Electrical Insulation

Different approaches, like various different coatings, were made to solve the problem of electrically insulating the coil winding layers against each other, while at the same time avoiding a material in the beam area that would be disadvantageous in terms of transmission and scattering properties.

Finally, we decided that not having any insulation material in the neutron window would be preferable. Given the thickness of the aluminium winding sheets of 2 mm and their excellent flatness, just having an air gap between them provides sufficient insulation. To ensure a well-defined spacing, sheets of an insulating material were inserted between the windings, and on an area of 50 by 80 cm^2, where the neutron beam penetrates the B_0 as well as the interior RF coil, the insulation material was cut away.

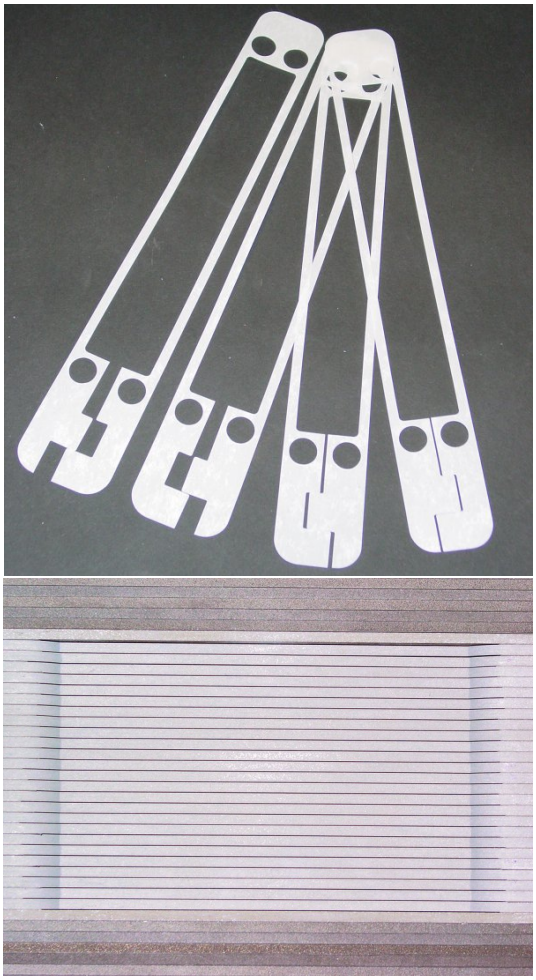

Figure 2.5: Nomex® insulation layers with a thickness of 130 μm (top). The material in the neutron beam window is cut out (bottom).

Instead of Kapton®, the insulator we chose was Nomex® paper, a very rigid, easy to handle, temperature-resistant, and inexpensive aramid fibre made of aromatic polyamids. Fig. 2.5 (top) shows the Nomex®sheets, which resemble the shape of the aluminum windings. They have a thickness of approx. 130 μm and were produced using a specially made and reusable diecutting tool (manufacturer/supplier: CMC Klebetechnik GmbH). Since even at high currents only a relatively low voltage needs to be applied (approx. 45 mV/winding voltage drop at 20 A), the air gap of 130 μm provides sufficient insulation. This solution seems to work well and no shortcuts were experienced yet. Fig. 2.5 (bottom) shows the neutron window of a bootstrap coil and the Nomex®-free area.

2.2.4 The Bootstrap Coil Construction

The core part of a MIRA bootstrap coil, depicted in Fig. 2.6, is the above described coil body consisting of the aluminum winding sheets. To superpose the static field it produces with a resonantly rotating field, an RF coil (see section 2.3) is inserted into its interior. In the following the principle construction of the bootstrap coil is explained, supported by and with references to the respective images.

The aluminum coil bodies must be mounted and fixated accurately. The Mu-metal yokes (Fig. 2.7) are placed on top and below in order to connect the B_0 coils and hence support

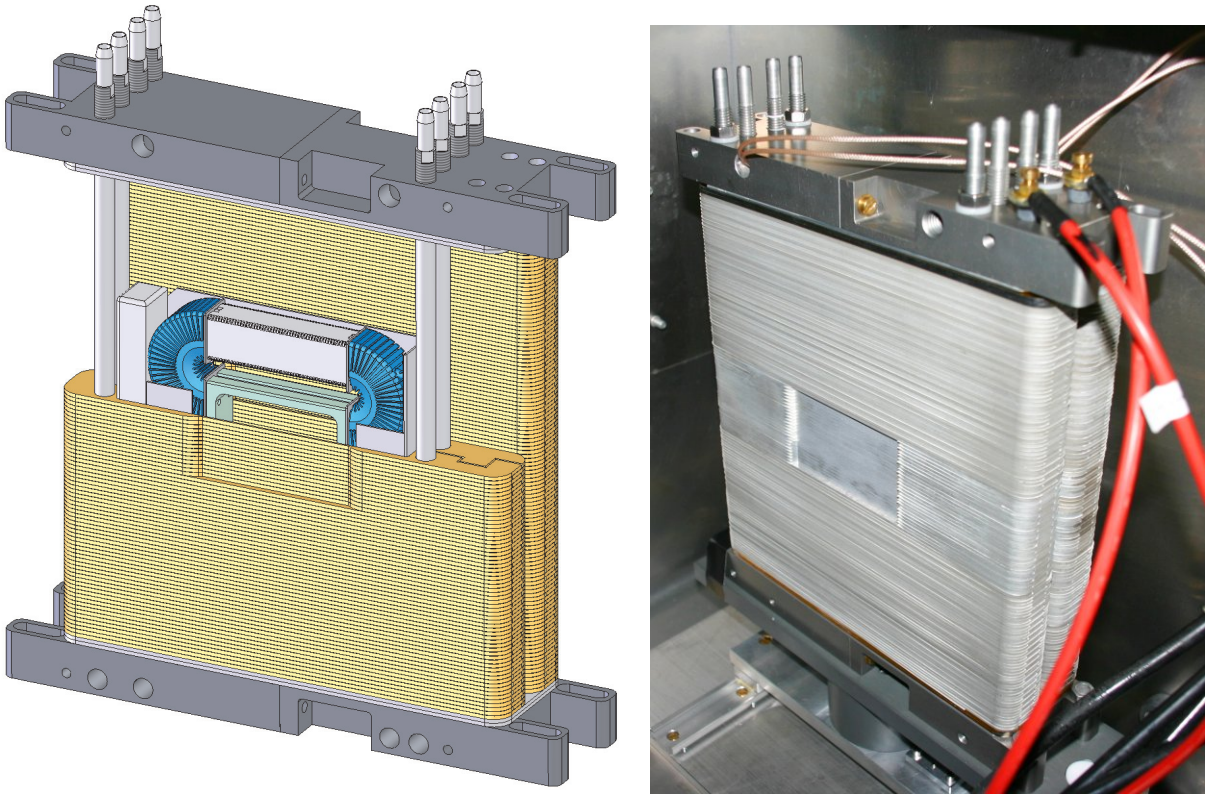

Figure 2.6: 3D drawing of a bootstrap coil and its components (left). A completely assembled coil with already inserted RF coils and installed air cooling is shown on the right (the Mu-metal shield of the coil is missing).

the magnetic flux refeed and homogenize the field as described in section 1.2.1.3. The cooling system (see also next section) has to be integrated and the RF coils must be positioned inside the B_0 coil in a secure and precise way. Fig. 2.6 shows a technical 3-D drawing of a complete bootstrap coil.

The coil windings are aligned by inserted anodised (hartcoated) aluminum pipes (Fig. 2.8), which also act as cooling channels. These are screwed into the base panel and waterproofly sealed with an o-ring (Fig. 2.9).
Beside the screw threads and bore holes for the cooling channels, the bottom and top panels also have respective outlets on their sides for cooling water or air and the RF coil cables. The panels are made of two parts connected by strong steel springs (Fig. 2.10 (bottom)). They serve the purpose of keeping the coil under slight tension, thus supporting the thermal expansion of the coil body at higher DC currents and avoiding deformation of the coil windings.
The DC current contacts for the power supply are on the top panel, while in the bottom panel a metal bridge connects the two single coils (Fig. 2.10 (top)). Electrical contact with the upmost coil winding is simply made by a threaded bolt reaching through the upper panel.

Up to the time of the writing of this thesis, four MIRA bootstrap coils have been built and installed. However, they differ slightly with respect to the neutron beam area: two of them have the above-mentioned neutron windows, reduced to a thickness of 1 mm as in Figs. 2.2 (right) and 2.6, the other two do not. The decision to not build them identically had its reason in some technical and processing difficulties we were experiencing: the Al sheets with the already cut out window required extreme care when handling them for the welding procedure.

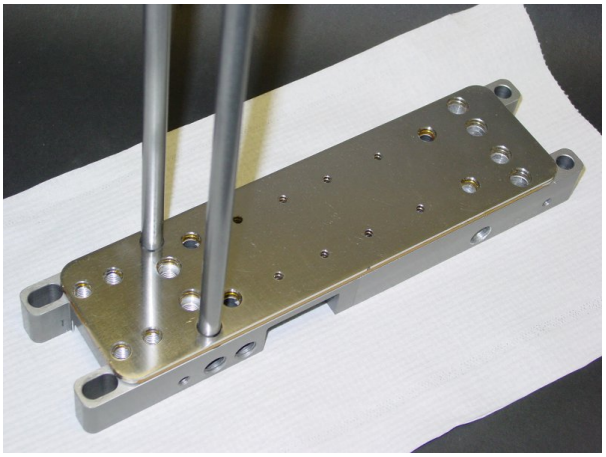

Figure 2.7: The Mu-metal yokes, placed above and below the coil bodies.

Figure 2.8: Hart-coated aluminum cooling pipes.

Figure 2.9: The top and bottom panels with inserted cooling pipes. Waterproof mounting is achieved by an o-ring seal.

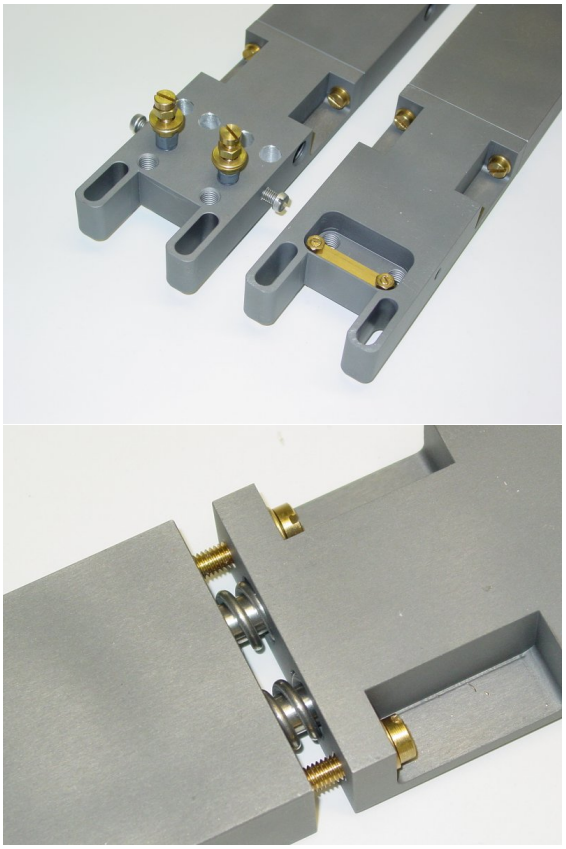

Figure 2.10: Contacts for the DC power supply on the upper panel and the contact bridge between the single coils (top). Strong springs in the interior mechanically support the heat expansion of the coil caused by high currents to avoid distortion of the windings (bottom).

Therefore, we made the attempt to add the cut-out in the neutron area to a ready-made 25 layer winding block after welding it. This was tried using both the wire-cut and cavity sinking EDM technologies. Since that could not be achieved at the time with completely satisfying results, we decided to build the two remaining coils entirely of aluminum sheets with 4 mm bars and accept the resulting higher neutron absorption. This had also several positive aspects:

- Lower heat production
- Supposedly better field homogeneity in the neutron window region due to the absence of current gradients
- Better mechanical handling
- Still acceptable transmission values (0.93 for one bootstrap coil including RF coils at 10 Å)

Depending on the measurement configuration and geometry (NRSE, MIEZE, SESANS, etc.), the last item is of more or less importance. For certain measurement variants like e.g. SESANS, it is necessary to tilt the bootstrap coils with respect to the beam direction. The neutron window of the B_0 coil has a width of 80 mm. Considering the width of neutron frame of the RF coils (see section 2.3), which are mounted inside the B_0 coil body, a tilting angle up to 45° is possible, still allowing a 10 mm neutron beam.

2.2.4.1 The Required Field Homogeneity and Mechanical Accuracy

The homogeneity of the static field depends on the principle coil design and the mechanical accuracy of the construct. The required homogeneity can be obtained by estimating the loss of polarization due to different path integrals (i.e. the phase the neutron spin accumulates when passing the coil) over the neutron beam cross section, which also depends on beam properties like wavelength and beam divergence.

The classical precession angle for a neutron when passing the coil on a trajectory s_i is

$$\varphi_i = \frac{\gamma}{v} \int_{s_i} |\boldsymbol{B}| \, \mathrm{d}s \,, \tag{2.1}$$

with γ being the gyromagnetic ratio and v the neutron velocity.

The estimation of the requirements has already been given in [2, 4]. The depolarization of the beam is caused by field inhomogeneities as well as mechanical deficiencies. To achieve an acceptable value of $\approx 90 - 95\%$ for the lower limit of the polarization, in our case the mean deviation of the precession angles for all trajectories over the neutron beam cross section should not exceed $\Delta\varphi \approx 10°$ for one coil.

For this purpose, the produced magnetic fields have been simulated with finite element methods prior to the construction process (s. section 2.2.8).

2.2.5 The Cooling System

Initially, a water cooling system was planned and the cooling pipes are installed with respective proper sealing (s. above). However, it was brought to our attention [26] that air cooling, if properly installed, provides a very effective way to dissipate heat. Therefore, we attached the cooling pipes to the instruments compressed air supply and from the outlets at the coil bottom, split the air stream and directed it on critical parts of the coil: the neutron windows (i.e. the coil center) and the gap between the two single coils.

Fig. 2.11 shows the construction. The air stream is guided by pipes which are normally used for cooling liquid at milling machines. Consisting of single plastic elements (blue and orange), they are very flexible yet stiff once positioned.

This low-cost solution has the huge advantage of avoiding water in the system, which always goes along with the risk of leakage. Although the heat capacity of air is far smaller than that of water, the air stream can be distributed significantly better.

A problem constitutes the fact that although the heat is transported away from the coil, the hot air is emitted into the interior of the Mu-metal shielding. From there, it should be further transported to the outside. A solution is to attach fans to available holes in the shielding bottom, which will be evaluated soon.

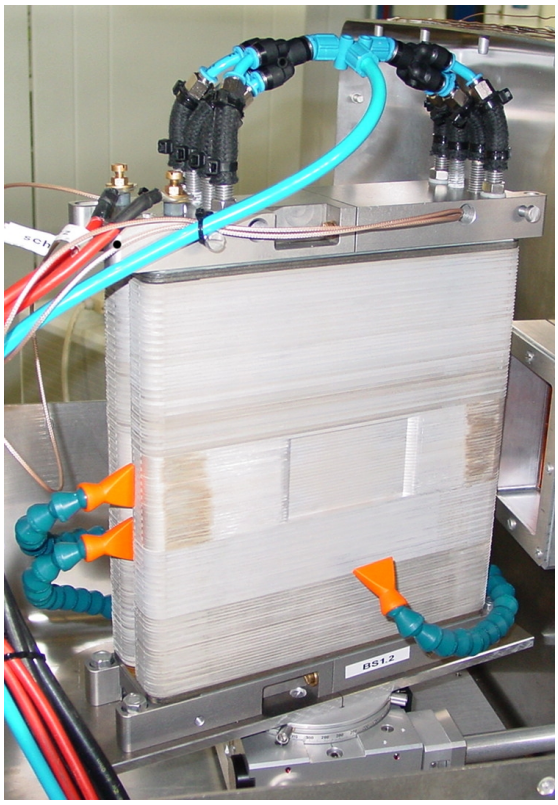

Figure 2.11: Bootstrap coil with air cooling system installed. Compressed air is led through the cooling pipes and then directed to and pointed on critical parts.

The cooling system has been tested at bootstrap coil 3 and 4. At an amperage of 45 A (corresponding to a magnetic flux density of 275 Gauss) the voltage drop is 30 V. With a resulting power dissipation of 1.35 kW, the coil temperature stabilized at approx. 80 °C. This is an acceptable value, and if the above mentioned problem of transporting the heat out of the magnetic shielding can be solved satisfactorily, the air cooling system in its current form could be kept.

2.2.6 Summary of the Properties of the B_0 Coils

The following table summarizes the relevant properties of the MIRA B_0 coils.

Property	Value
Thickness of Al winding sheet	2 mm
Aluminum alloy	AlMg3
Number of windings	117
Length (single coil)	250 mm
Width (single coil)	25 mm
Coil height	300 mm
Neutron window	80×50 mm^2
Maximum tilting angle (w.r.t. beam direction)	45°
Thickness of Nomex®layer (insulation)	0.13 mm
Neutron window thickness (in beam direction)	1 mm (coil 1 & 2), 4 mm (coil 3 & 4)
Magnetic flux density (calculated[1])	$\approx$ 117.6 Gauss at 20 A
Magnetic flux density (measured[2])	$\approx$ 122 Gauss at 20 A

[1] without Mu-metal yokes

[2] with open coil (upper Mu-metal yoke missing), measured at the center

Table 2.1: Summary of the MIRA B_0 coil properties.

A reasonable measurement of the field homogeneity of a completely assembled coil was not possible for several reasons: extra holes would have been necessary in both the upper panel and the Mu-metal yoke to insert the probe. Furthermore, the measurement should have been performed in zero-field to obtain an accurate result. Although many parameters and additional components are involved, the quality of the coils can be estimated best by actual neutron measurements (section 3.2).

2.2.7 Investigation of the Anodised Aluminum Band

As explained earlier in this chapter, at the beginning of this PhD project the question arose whether the NRSE design concept of the coils built for the instruments RESEDA, TRISP, or ZETA (at the Institute Laue-Langevin) could also be used for MIRA, or how it could be improved. The critical component was, as mentioned, the anodised aluminum band used for the coil windings of both B_0 and (in a thinner variant) RF coils.

The properties of the band – dimensions, alloy, insulation layer thickness, inclusion of chemically combined water – were known relatively well, but no measurements about neutron absorption and small angle scattering existed. Therefore, small angle scattering measurements were conducted at the Paul-Scherrer-Institut (PSI) at the SANS machines. In addition to the original untreated Al band, other samples were investigated that had undergone different treatments prior to the measurements: annealing, deuteration (at 200°C), and a combination of both.

The measurements at wavelengths of 8 Å revealed that transmission and scattering properties could be enhanced. Fig. 2.12a shows a plot of intensity over the scattering angle. The small

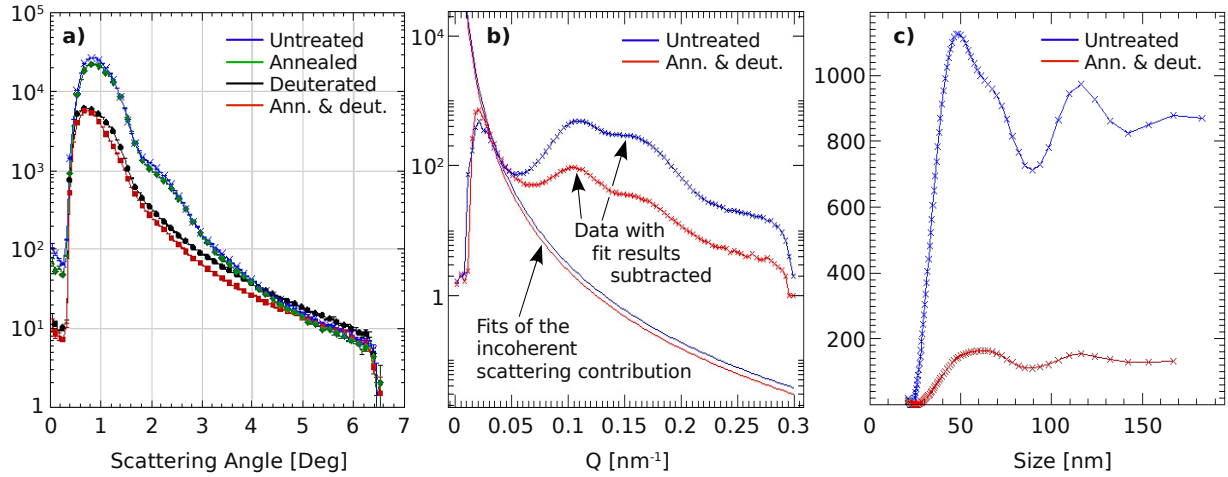

Figure 2.12: Results from SANS measurements on the anodised Al band.
a) Plot of intensity over scattering angle of all samples.
b) Fits of the incoherent scattering and the coherent scattering contribution for the untreated and deuterated & annealed sample (intensity over Q).
c) Discrete Fourier transformation of the coherent scattering fraction (arbitrary units on the ordinate).

angle scattering could be reduced most efficiently by exchanging the H_2O by D_2O in a deuterium atmosphere at 200°C, whereas the effect of the annealing procedure was noticable mainly in the transmission values listed in Table 2.2.7. The annealed sample has the lowest absorption, which might appear inconclusive at first. This can be explained by the extreme heating, which most likely evaporated the water enclosed in the anodization layer.

Plotted in Fig. 2.12b is the intensity over Q in momentum space for the untreated and deuterated&annealed samples. The straight lines are fits to the incoherent scattering part of the data at very small Q values. The data points indicated by red and blue crosses denote the coherent scattering contribution of the samples. They are obtained by subtracting the fitting curves from the raw data.

The incoherent fraction of the scattered intensity is then transformed into real space by a discrete Fourier transformation, shown in Fig. 2.12c. This finally gives information about the size of the scattering structures or particles. We see peaks at approx. 50-70 nm and 100-130 nm, the units on the ordinate are arbitrary.

To also get a visual impression of the aluminum band on the microscopic scale and verify the results of the SANS measurements, pictures were taken using an Atomic Force Microscope (AFM). The measurements could be done at the institute E13, Physics Department TU Munich. Although it was not possible to further improve the quality of the AFM pictures due to technical reasons, the dimensions of the scattering structures within the surface layer could be confirmed. Fig. 2.13 shows two surface sectors at different resolutions. The larger vertical grooves (left picture) most probably result from the manufacturing process (rolling) of the Al

Sample	Thickness	Wavelength	Transmission
Untreated	6 mm	8 Å	0.886 ± 0.016
Annealed	6 mm	8 Å	0.913 ± 0.016
Deuterated	6 mm	8 Å	0.896 ± 0.016
Ann. & deut.	6 mm	8 Å	0.920 ± 0.016

Table 2.2: Transmission values of the investigated Al band samples for different treatments.

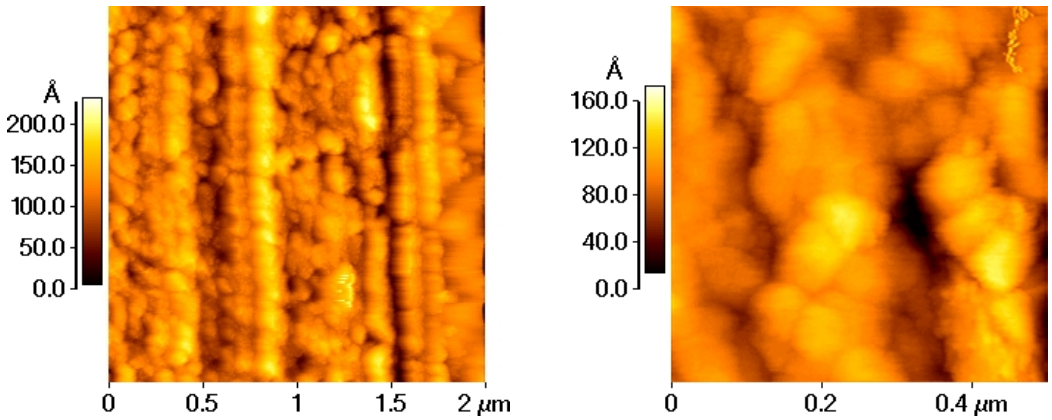

Figure 2.13: Atomic Force Microscope (AFM) measurements of the anodised Al band surface. The dimensions in the surface structure are in agreement with the results from previous SANS measurements.

band itself. The smaller dot-like structure develops during the anodization; this and the inclusion of water in the anodization layer are the main sources for the observed small angle scattering.

Although deuteration positively affects the properties of the Al band, the coherent scattering cannot be suppressed entirely due to the surface structure. Furthermore, as could be seen from the annealed samples, the D_20 contained in the anodizatoin layer is prone to evaporate slowly by heating of the coils during normal operation, to be replaced again by H_2O (air humidity). So the results of the measurements led to the decision to develop new coils with more favorable scattering properties, especially in the light of the long wavelengths MIRA is operated at.

2.2.8 Magnetic Field Simulations

The field homogeneity required for the static field in NRSE resonance flippers was estimated in section 2.2.4.1. As mentioned there, the field quality does not only depend on the mechanical accuracy, but also on the principle design. The layer concept of the MIRA coils with the integrated cooling pipes and the non-symmetric contact fields might not appear suitable at first glance, compared to conventional wound coils. To investigate the produced magnet field and its suitability, computer-aided simulations were performed.

For this purpose, the software package FARADAY® was used, a 3D eddy current magnetic field solver, which implements the so-called Boundary Element Method (BEM) to calculate the relevant physical quantities. That is, like the Finite Element Method (FEM), a discretization method to solve initial and boundary value problems in mathematical physics. In contrast to FEM, the BEM method only discretizes (i.e. divide into suitable subareas) the surface of the investigated structure and not the volumes. This procedure has certain advantages, especially with respect to the geometry at hand.

Although FARADAY® is designed to be an eddy current solver, also DC currents and static fields can be investigated. Further information about the software can be found in [27], the boundary element method is covered in [28].

Besides FARADAY® other FEM 3D simulation software packages were tested (ANSYS®, FEMLab® and Mathematica® with an extension module). It turned out that only with

FARADAY® a satisfying solution to the problem could be found. The reason for that has its origin in the geometry of the MIRA coils:

i) the winding sheets are quite thin, i.e. their volumes have extreme proportions (length compared to thickness).

ii) unlike a wound coil, they have no relevant symmetry plane if the simulation model should be as close to the original as possible.

The first property is known to cause problems with FEM-based programs. The second, since very little symmetries can be used, further complicates the model and increases its size and hence the computing time significantly. This also caused problems with FARADAY®, but still a detailed enough model could be created and processed.

The objectives of the simulations were on the one hand to investigate the field homogeneity inside the coil for different models, and on the other hand to obtain information of the stray fields on the outside. The models differed with respect to: single coil and bootstrap geometry and inclusion or omission of a Mu-metal yoke, respectively. Since NRSE flippers are normally built as bootstrap coils, we will mainly focus on these model types here.

Figs. 2.14a,b show the 3D model of two coil windings. Due to the anti-parallel stacking of the winding layers, two subsequent windings constitute the smallest possible entity for the model. The coil body was then created by multiplying it (s. Fig. 2.14c). All volumes that do not contribute to the actual calculation are not plotted in this illustration.

The blue conic arrows indicate the current flux. The flux had to be created by defining the volumes which should be passed through by a volume current. More desirable would have been a method which allows to build the model, define a voltage drop at the contact fields and let the current density in the geometry be calculated by the software. A feature like this was in the process of being implemented into future FARADAY® versions, but not available at the time. The amperage applied was 5.8 A, this is the corresponding to the (calculated) current producing a B_0 field that matches an RF frequency of 100 kHz.

A difficult part to model were the contact spots, where a current flux from one layer to the next, turning from a perpendicular direction into the winding sheet plane had to be realized. The holes for cooling channels as visible in Fig. 2.2 had to be omitted due to restrictions arising from the current definition method described above.

The Mu-metal yokes (s. section 2.2.4) are crucial for bootstrap coils for guiding the magnetic flux. But since the fieldlines enter the metal plates almost perpendicular, they also have the effect of virtually expanding the coil infinitely, hence homogenizing the field inside. Therefore, we included them in the simulation model. This, on the other hand, implicated some disadvantages: with only the windings in the model it was possible to define a linear pattern for the field solver and that way simulating a coil of full height (without the need of actually multiplying the model geometry). With the yoke included this was not possible since the pattern definition applies always to the entire model. After 12 geometry multiplications ($\widehat{=}$ 24 windings) the model reached the limits of its processibility.

Fig. 2.15 shows the contour plots of the magnetic flux density amplitude in the middle plane for a model with and without the Mu-metal yokes included. In the latter the homogeneity is significantly improved.

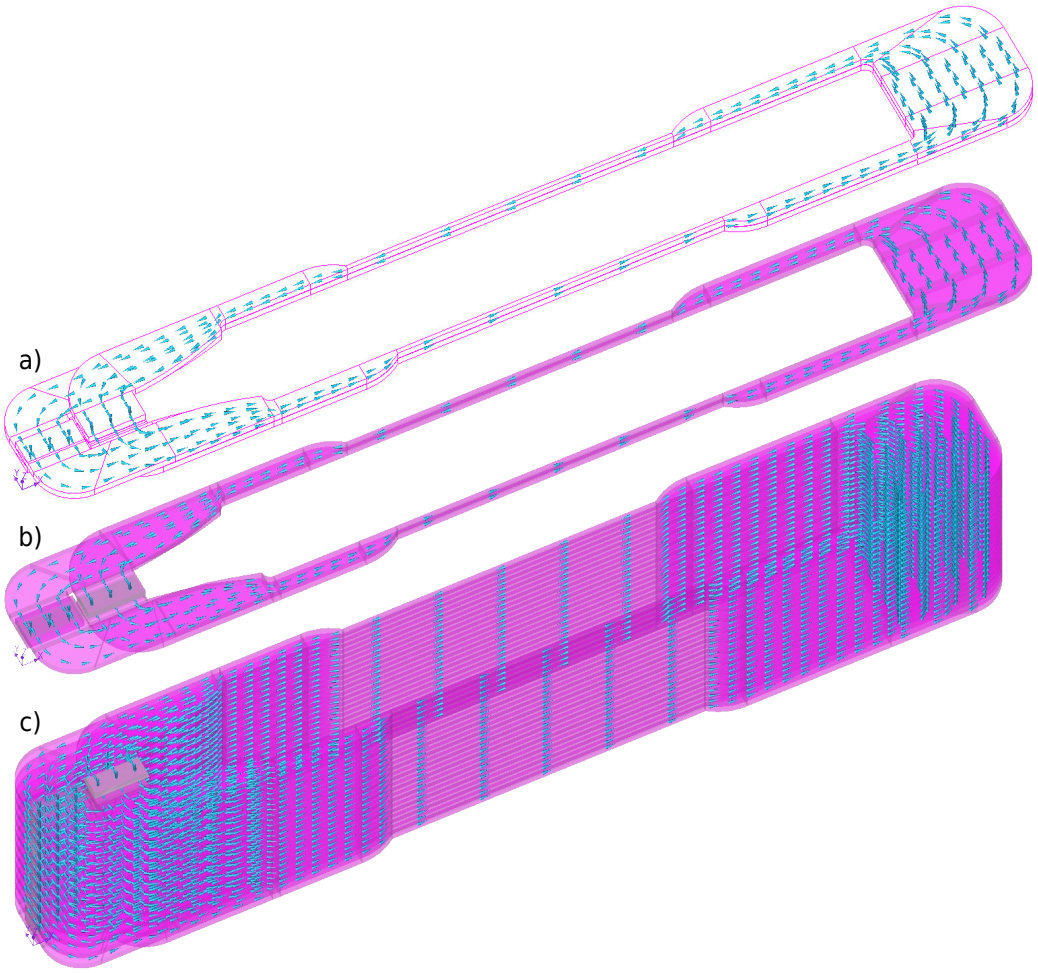

Figure 2.14: Plot of the simulation model and the current distribution through the volumes. a,b) Two windings stacked with opposite orientation are the smallest model entity. c) The entire model is created by multiplying the geometry.

The results of the simulation, of course, allowed not only for the plotting of field lines or intensities, but also for extracting the data and calculating the field integral and neutron precession angles according to Eq. (2.1) for in principle any arbitrary path in the model. The standard deviation of the precession angle for flight paths within the core beam area of the coil (neutron window) was in all cases below 10°, as demanded by the prerequisites described in section 2.2.4.1. Of course the divergence of the neutron beam in real experiments will cause neutrons with different flight paths to accumulate different phases in the coil. But this situation is very difficult to account for when planning and simulating coils with fields as homogeneous as possible.

From the results of the simulations we concluded that the principle coil design was suited for our purposes. Also the coil could not be simulated in full height (only the beam area part) and the field quality can be expected to rather improve in the case of the longer full-sized coil.

Eventually a Mu-metal shield around the coil was added to the model. Normally these kind of shieldings are installed to reduce remaining stray fields emerging from the coil and reaching into the zero-field region. Mu-metal has a strong influence on the magnetic environment by its extraordinary permeability. If the either the shielding design is not appropriate or the material

properties have been altered and it adopted a magnetic remanence by e.g. mechanical or thermal strain, the effects on the flux distribution in the surrounding space can be quite unpredictable. With the MIRA coil shieldings one or both of the latter have happend and after observing severe depolarization, they were dismounted again. To illustrate the effects just described, Fig. 2.16 shows a vertical and a horizontal arrow plot with the shielding case added to the geometry. The color coding has been scaled so that the critical parts are well distinguishable: the Mu-meta edges attract the flux lines and thus increase the field strength close to the beam window area. If distances and geometric proportions of the shielding are not chosen carefully, more problems may arise than are solved. For calculations on Mu-metal shieldings for NRSE applications see e.g. [29] and [21].

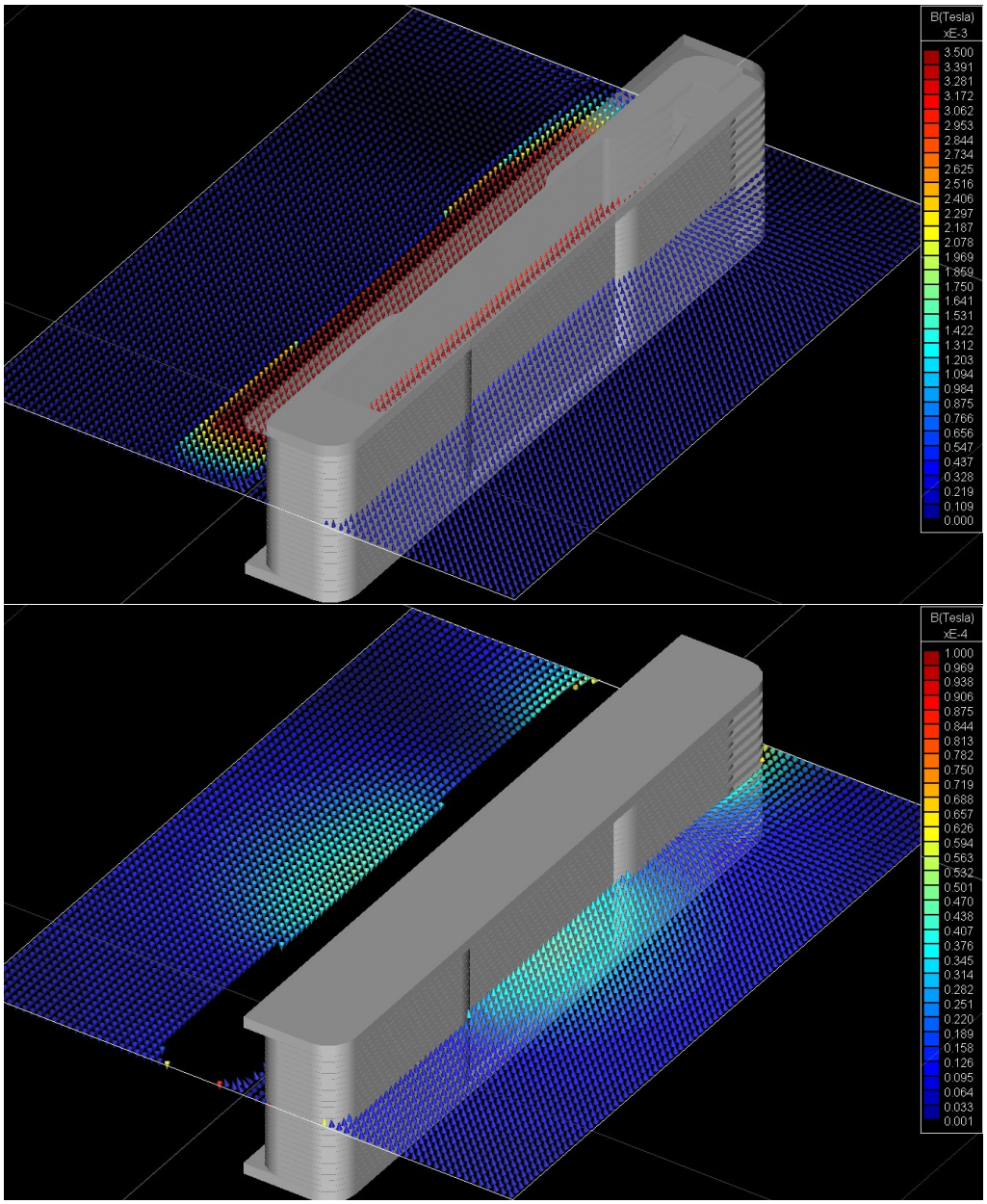

Figure 2.16: Arrow plots showing the magnetic field magnitude and flux line direction in the middle plane of a bootstrap coil with Mu-metal yokes attached above and below. The two plots have a different scaling range to reveal the field distribution inside the coil (top) and the much weaker stray fields on the outside (bottom).

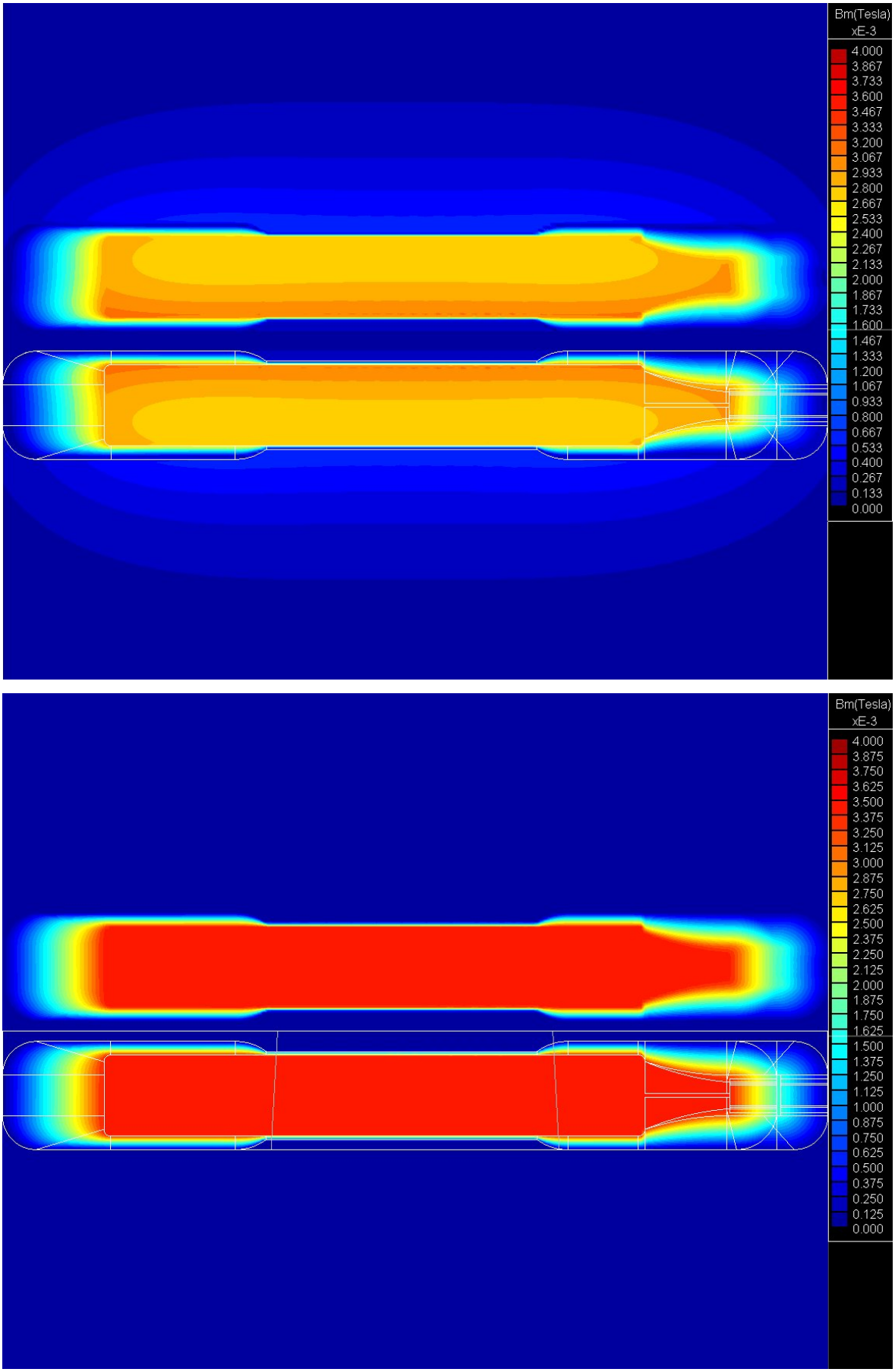

Figure 2.15: Contour plots of the magnetic field magnitude in the middle plane of a bootstrap coil. In comparison to the model without Mu-metal yoke (top), the homogeneity is improved (bottom).

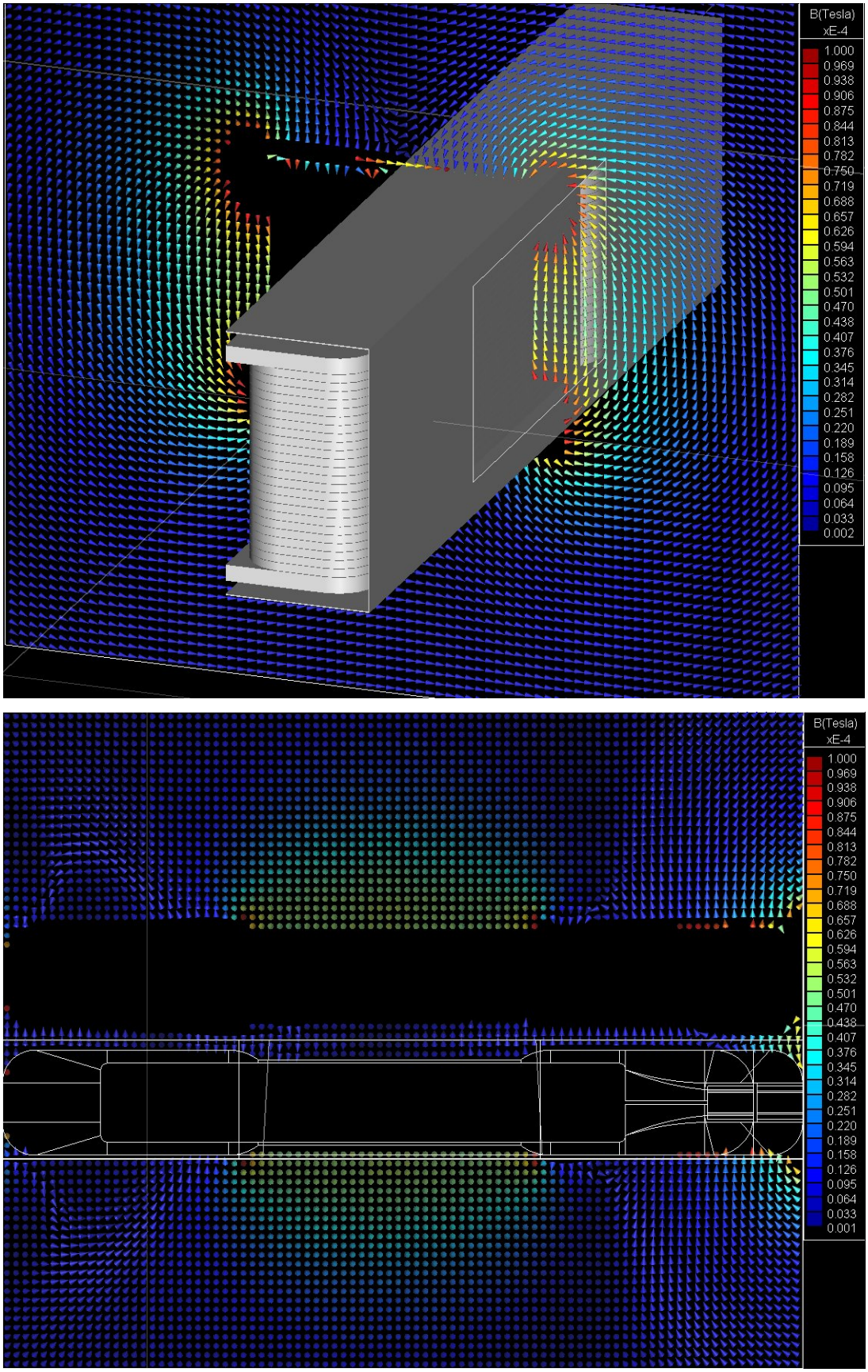

Figure 2.17: Vertical (top) and horizontal arrow plots of the magnetic field magnitude and direction with a Mu-metal shielding case in the model. The two plots have been scaled so that the influence of the shielding on the field close to the neutron beam area becomes visible.

2.3 The RF Coils

The static B_0 field has to be superimposed with a rotating RF field. Since rotating fields can be realized only with considerable effort, a linearly oscillating field (which can be decomposed into two counter-rotating fields) is used, generated by the RF coils. The resulting slight inhomogeneity of the static field caused by the wrong RF component, the so-called Bloch-Siegert shift described in section 1.1.4.1, is usually tolerated. It is negligible for cold neutrons and frequencies of 50 kHz and above.

The RF coils must not, however, produce significant stray fields. Therefore, a design exists (RESEDA, ZETA) that includes a magnetic flux refeed in form of two closed loops. Fig. 2.18 show the principle design with all components, and Fig. 2.19 a wound and completely assembled coil. The design was overhauled compared to previous versions that have been built for the instrument RESEDA.

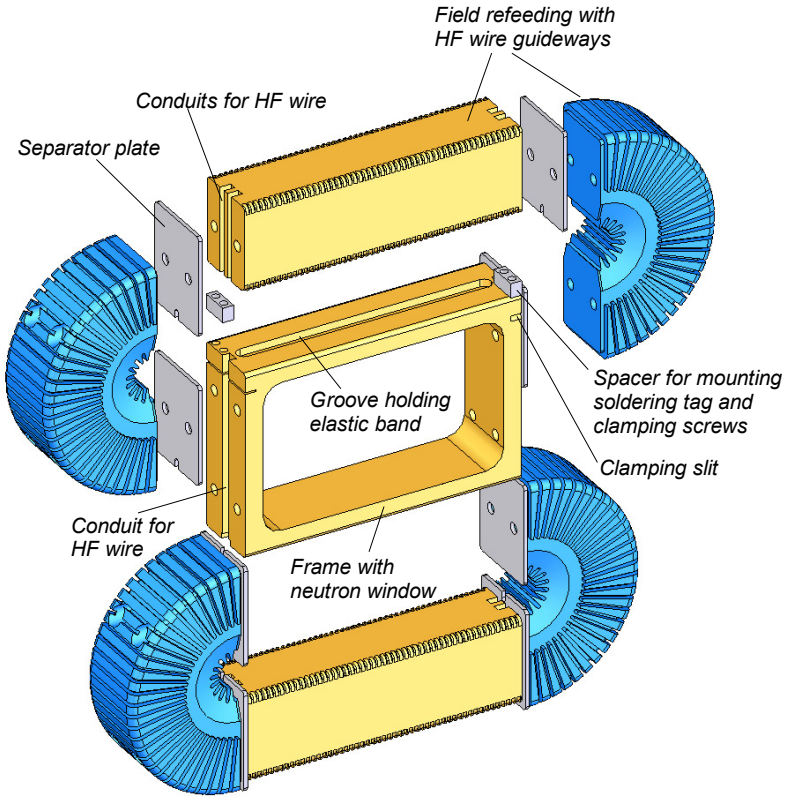

Figure 2.18: Principle design of the MIRA RF coils.

The main improvements are

- Replacing the anodised aluminum tape by one made of pure aluminum without insulation to reduce absorption and scattering
- The electrical contacts and cable conduits have been made more secure and shortcut-free by leading them internally through the coil parts (s. Fig. 2.18)
- Usage of a doubly insulated HF wire, which furthermore is now stored inside grooves in the shell-like parts of the flux refeed (printed blue in Fig. 2.18). The RF coil can be inserted into and extracted from the B_0 coil more safely without harming the wire or aluminum windings, which avoids previous problems with shortcuts and flashovers.

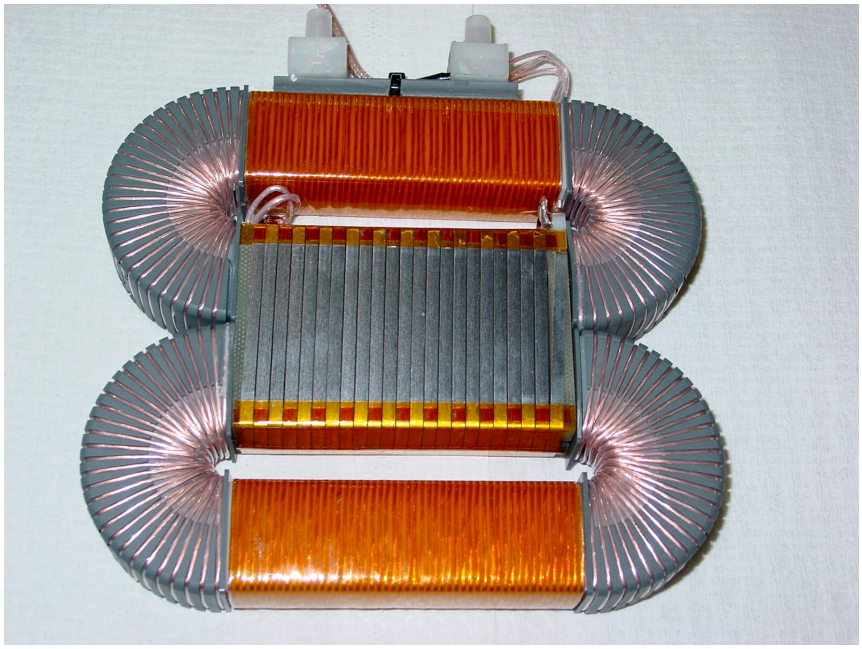

Figure 2.19: Assembled RF coil. The aluminum wire is not isolated but wound in a way that leaves a gap between the windings with a Kapton® stripe as spacer.

The coil body in the center is made of glass-fiber reinforced plastic (GRP) to avoid any mechanical distortion. The other plastic parts are made of either PVC or the polyamid PA6.

The winding tape is 99.5% pure aluminum (3×0.2 mm^2, supplier: Allfoils Inc., Cleveland, USA). In order to maintain the good neutron absorption and scattering properties of Al, it is not coated with any insulator, but wound in a way that leaves a sufficient gap between subsequent windings using meandering Kapton® stripes as spacers.

The refeed parts bear a HF filament wire (supplier: Synflex Elektro GmbH & Co. KG) to avoid heat production at higher frequencies due to the skin effect. It is connected to the Al band at the end of the neutron window frame with soldering tags.

A MIRA RF coil has an inductance of approx. 30 µH, this value becomes relevant when the oscillation circuit must be adapted to the desired frequency (see section 2.8.2). In the bootstrap mode both RF coils are used and they are connected in parallel, which yields a total inductance of approx. 15 µH per NRSE flipper. Table 2.3 summarizes the most relevant properties of the RF coils. Relevant for the resonant π-flip is only the area where static and rotating fields are superimposed, which is therefore defined by the thickness of the RF coil in beam direction

Property	**Value**
Dimensions aluminum band	3 mm × 0.2 mm
Aluminum alloy	0.995% pure Al
Number of windings	20
Length	120 mm
Width (in beam direction)	20 mm
Coil height	50 mm
Inductance (Al coil and flux refeed parts)	≈ 30 µH

Table 2.3: Summary of the MIRA RF coil properties.

(20 mm). The presence of a homogeneous static field outside that area merely adds a static phase to the signal.

2.4 The Coupling Coils

Coupling coils are required to have a defined way of leading the neutron polarization from the outside guide field into the interior of the Mu-metal shielding (or vice versa) and turn the polarization vector into the plane in which the RF field rotates, i.e. perpendicular to the static field. The coils are mounted tightly inside a Mu-metal nozzle at the front side of the shielding, as shown in Fig. 2.20 (top). The nozzle will carry the outside flux and hence absorb stray fields which otherwise might reach into the zero field region.

Therefore, the coils are built to produce an abrupt transition from field to zero-field on one side, realized by a current sheet (cp. Fig. 2.20 (bottom)), and an adiabatic transition into the guide field by bending out the coil windings on the other side.

The working principle of a coupling coil has been explained in detail in section 1.1.4.5. The field turns adiabatically from z- to y-direction, which is the case if the spatial rotation of the field happens much slower than the precession of the spin (see Eq. (1.101)). The polarization vector will then follow the direction of the field vector until the current sheet is reached, which it transfers unchanged due to the abrupt transition.

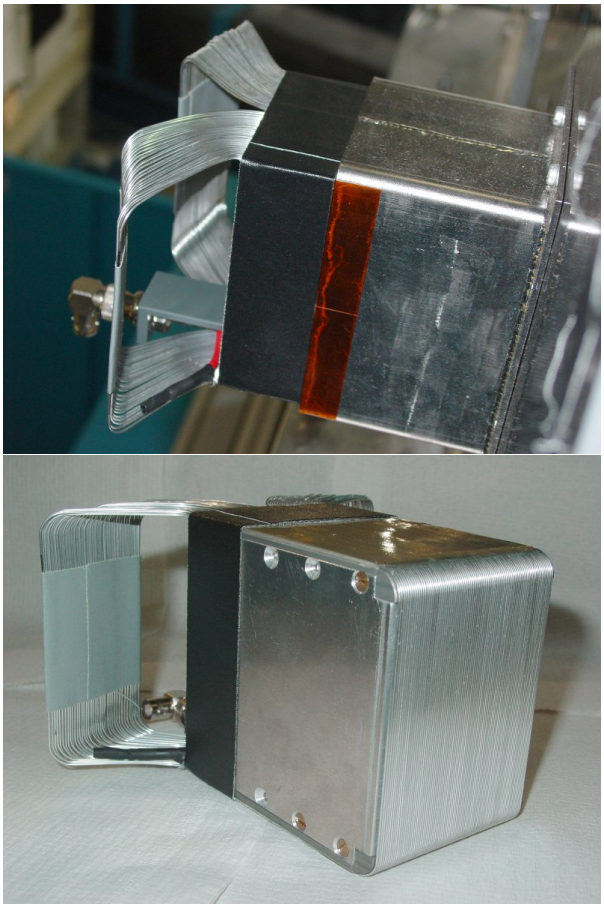

Figure 2.20: The MIRA coupling coils are mounted at the front sides of the shieldings inside a Mu-metal nozzle. It implements an abrupt field transition on one side, and an adiabatic on the other.

Whether the coil does function as just described depends on its geometry and the neutron wavelength. The dimensions of the MIRA coupling coils have been chosen to comply with these requirements. The wire used for winding them is made of anodised pure Al with a gauge of 0.8 mm.

2.5 The Polarization Analyzers

The three polarization analysis devices used in the measurements were supermirror benders, one of them (manufacturer: Swiss Neutronics) is shown in Fig. 2.21. The working principle has already been explained in section 1.1.5. They are capable of producing a beam polarization of ≈ 93 %.

A difficulty in usage inherent to those devices is the fact that the neutron beam has to be reflected („bent“) at the layers and therefore needs to enter and/or leave the bender under a fixed angle of $\approx 1\text{-}2^{\circ}$. Hence, the position of the instrument parts has to be adapted and the shieldings including the NRSE coils need careful adjustedment.

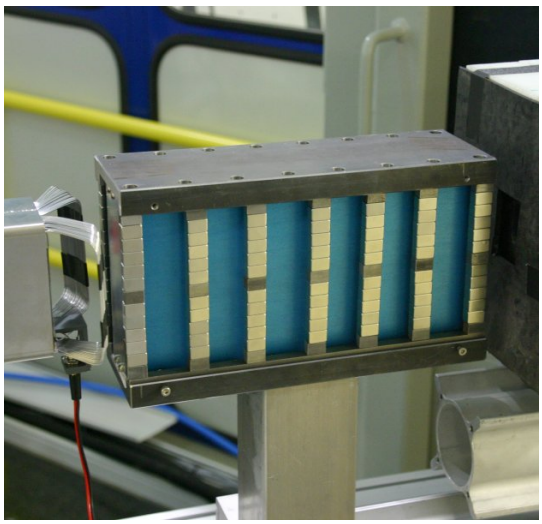

Figure 2.21: Polarization device (bender) used in the MIEZE/Multi-MIEZE measurements.

To maintain the magnetization of the layers of the bender, it is mounted inside a magnetic cage producing a field of approx. 300 Gauss at its center. The stray fields on the outside are therefore significant and an appropriate distance to the Mu-metal shielding and the coupling coils must be kept and bridged with appropriate guide-fields.

2.6 The Magnetic Shielding

External magnetic fields (like the terrestrial magnetic field and stray fields from other instrumentation) must be compensated or absorbed to obtain the required zero field region between the two resonance flippers. This is realized by installing the coils inside a magnetic shielding, made of a magnetically soft material with a high permeability μ and a very low remanent magnetization. This so-called permalloy, consisting of mainly nickel and iron, is also well-known as

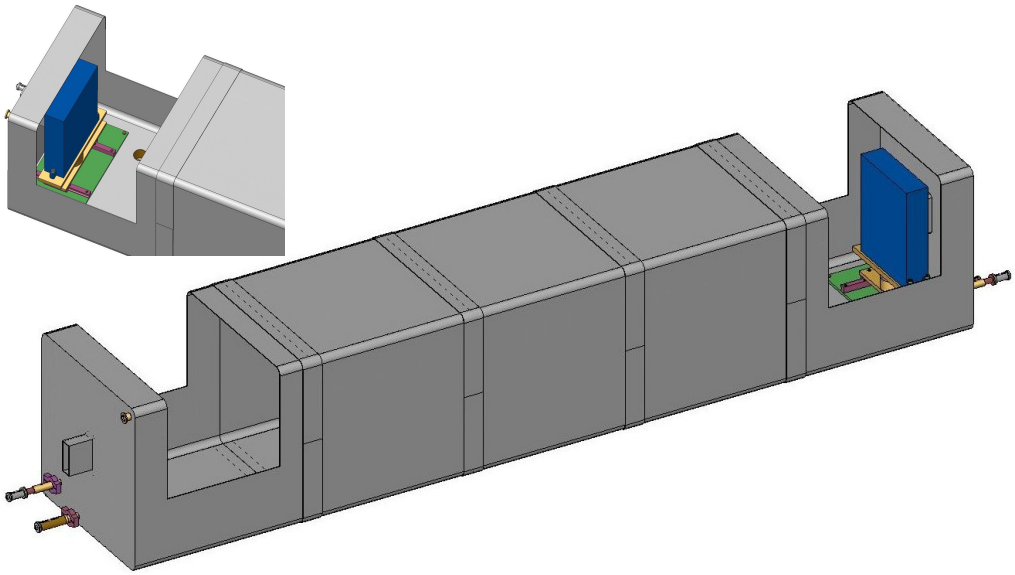

Figure 2.22: 3D model of the longer Mu-metal shielding used for the Multi-MIEZE measurements, including the coil mounting and positioning system.

Mu-metal® (a registered trade mark of VAC Vacuumschmelze, Hanau, Germany).

The extraordinary magnetic properties originate from a special treatment, which includes annealing at approx. 1100 °C in a hydrogen atmosphere and a controlled cooling procedure, resulting in permeability values of ≈ 50,000 (depending on the shape).

The MIRA shieldings were designed at the FRM-II in collaboration with VAC and built by VAC in Hanau. Due to budgetary reasons, only a single layer shielding of 2 mm thickness was conceptualized, although given the long wavelengths at the MIRA beamline, a double-layer shielding would have been preferable.

Fig. 2.22 shows a 3D technical drawing including the installed positioning system. The boxes have outlets on the top and bottom of the front sides and have been designed to allow for flooding with Argon gas if necessary. They have a length of 3 m and 1.2 m, respectively, and a square profile of 50×50 cm^2. On the front sides rectangular nozzles are mounted, covering 50×100 mm^2 holes and holding the coupling coils (see section 2.4).

The shielding bodies were designed to be modular and therefore consist of several parts. For the use as a permanent measuring option at MIRA, the shieldings will be reassembled and are shorter to match the instrument geometry of MIRA (sample environment and detector position).

For Mu-metal shieldings having longish geometric proportions and openings at the front sides, the component along the shield axis is always bound to be less well absorbed, i.e. the longitudinal shielding factor is lower than the vertical. In recent measurements, such a remaining longitudinal magnetic field component was recognized inside the shielding. The resulting depolarization most probably accounts for a significant part of the contrast losses observed, but beam-time restrictions didn't allow for countermeasures (see also sections 3.3 and 3.5).

2.7 The Detector System

A MIEZE signal is a high-frequency, time-dependent intensity modulation only detectable at a specific distance after the resonance flipper coils. Therefore, the detector used must be capable of detecting the neutrons both fast enough and in a well-defined detection plane. Best suited for this purpose are scintillation detectors in combination with a photomultiplier tube, a Single Channel Analyzer (SCA), and – in order to finally obtain a time-resolved signal – a multichannel analyzer card.

The detector used in our MIEZE measurements was already available at the FRM-II. It is a ^{6}Li-doped glass scintillator of ≈ 0.5 mm thickness, with an integrated photomultiplier tube. The approximated detection efficiency is 60 - 70% for a signal frequency of 200 kHz.

The SCA was an ORTEC® 590A with selectable shaping times (active-filter shaping) from 0.5-3 µs and high count-rate capability. The multichannel analyzer card along with respective hardware drivers were provided by the electronics group at FRM-II. It has a resolution of 16 channels, which can be switched with a frequency of up to 6 MHz. The card has a PCI interface and could therefore be integrated easily into the data acquisition system of MIRA. Two input signals are required for operation: the detector signal and a RF signal to trigger switching to the next counting channel. Both must comply with the TTL standard, i.e. the input level

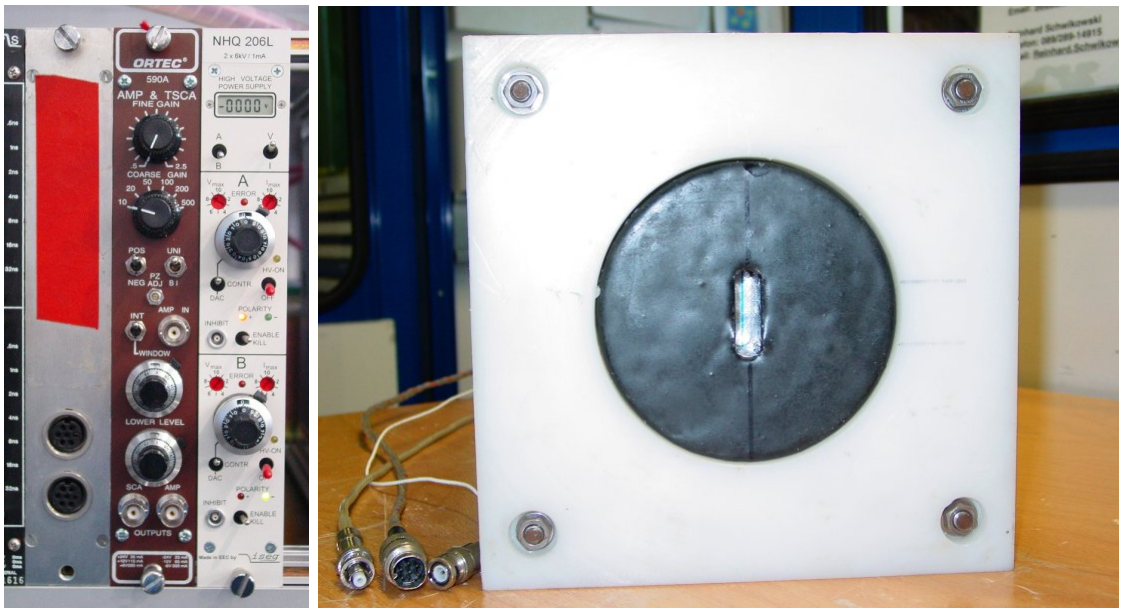

Figure 2.23: Pre-amplifier, Single Channel Analyzer (SCA), High Voltage (HV) supply, and the scintillation detector (left to right). For radiation protection the latter is covered in an iron tube (black) and a polyethylene shielding (white).

must be between 0 - 0.8 V („low“) and 2 - 5 V („high“). The trigger signal is produced by a wave function generator (see section 2.8.1) that is phase-locked with the generators feeding the MIEZE RF oscillating circuit. The phase-locking is necessary to avoid any drifting of the input signals relative to each other. This in turn would result in a non-defined phase relation of the spin-up and spin-down states and hence a destruction of the signal contrast at the detector.

2.8 The Electronic Equipment

The electronic devices needed to supply the B_0 coils with a highly stabilized DC current and to implement the RF oscillating circuit are mostly standard and readily available. Only the adaptation of the resonant curcuit requires a custom-made solution, as described below.

2.8.1 The Wave Function Generators and RF Amplifiers

To produce a resonant sinusoidal oscillation in the RF curcuit, basically three components are needed: a waveform generator with sufficient frequency stability, an amplifier, and a device to adapt the impedance of the oscillation circuit according to the chosen frequency. The current through the RF coils defines the field, which must be adapted to match the π-flip condition depending on the neutron wavelength.

The principle implementation of the RF circuit is very similar to the one at the instrument RESEDA. For more information we refer to [30].

The arbitrary waveform generators (vendor: Agilent®, models: 33250/33220A) depicted in Fig. 2.24 (top) are able to produce sine signals from 1 µHz to 20 MHz, with an accuracy of $\pm$(20 ppm + 3 pHz) per year (frequency) and ± 1 mV_{PP} (amplitude) .

The function generators are equipped with an external frequency reference option, which allows for phase-locking all devices by letting them run on one reference quartz. As mentioned in 2.7, this is important to avoid drifting of the multichannel analyzer trigger pulses, which would destroy the MIEZE signal.

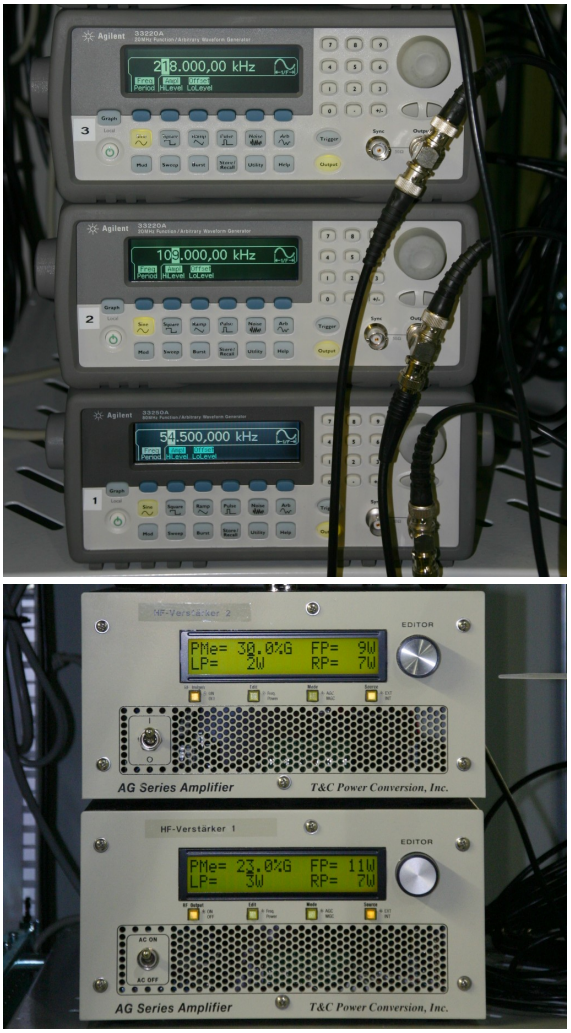

Figure 2.24: The RF function generators and signal amplifiers.

To obtain the required field strength produced by the RF coils, the generated signal – i.e. the current through the coils – must be amplified. The three amplifiers used (vendor: T&C Power Conversion Inc., model: AG 1016) are shown in Fig. 2.24 (bottom), they have a harmonic level better then -14 dBc for the 3rd harmonic at 550 W.

When the RF circuit is correctly tuned and resonantly oscillating, the amplifier is able to feed power into it without significant reflection (see next section). Whether or not this is the case can easily be observed on the display of the device (see Fig. 2.24). It shows the power put into the circuit (Forward Power, FP), the reflected power (Reverse Power, RP), and the power actually loaded (Load Power, LP).

For measurements the fine-tuning of the RF current is done by altering the input signal amplitude while keeping the gain fixed. This allows for a more fine-grained adaptation and is,

due to technical reasons, also safer in terms of avoiding overload.

2.8.2 The Capacitance Adaptation Devices

The design of the RF resonator circuit and especially that of the capacitance adaptation devices (C-boxes) has been adapted from the RESEDA instrument. Since the relevant components neither have extraordinarily complicated physical aspects, nor are they execptionally critical parts of the instrument technical-wise, we will restrict ourselves to mainly describing the physical principle. More technical details have been covered in [30], which we refer to for that purpose.

The capacitors are all connected in parallel to each other, and in series to the RF coils. The resulting impedance of the RF circuit is then

$$Z = \sum_i R_i + i\left(\omega L_\mathrm{c} - \frac{1}{\omega \sum_j C_j}\right) , \quad (2.2)$$

with $\sum_i R_i$ being the total resistance, L_c the inductance of the RF coils in the circuit, and C_j the involved capacitances.

In order to produce a resonant oscillation and load power into the RF circuit, the impendance of the integrated components must match the frequency. Therefore, Z has to be adapted in a way that its imaginary part vanishes,

$$\Im(Z) = \omega L_\mathrm{c} - \frac{1}{\omega \sum_j C_j} \stackrel{!}{=} 0 \iff$$
$$C_\mathrm{p} \equiv \sum_j C_j = \frac{1}{\omega^2 L_\mathrm{c}} , \quad (2.3)$$

which is achieved by adding capacitances C_j according to the desired frequency ω.

Figure 2.25: The MIRA capacitance adaptation boxes (C-boxes). The mica capacitors are connected in parallel and suited for high voltage.

A MIRA RF coil (see section 2.3) has an inductance of approx. 30 µH. In the bootstrap case the RF coils are connected in parallel, which yields a total inductance of $L_\mathrm{c} = 15$ µH per NRSE flipper coil.

The C-boxes of RESEDA also have additional serial capacitors for impedance adaptation, which were omitted for MIRA due to simplicity and budgetary reasons. This means a certain loss of adaptivity in terms of tunable frequencies, but it is still sufficient for MIRA. A circuit diagram of the MIRA C-boxes can be found in Appendix A.3.

Due to possible high voltage that can occur in the oscillating circuit, the capacitors used (Fig. 2.25 (bottom)) are fabricated of mica, a silicate mineral which features high dielectric strength and very good chemical stability (vendor: Richardson Electronics GmbH, Puchheim, Germany).

The capacitance values chosen are in the range of 2.5 nF to 1.28 µF with additional correction capacitors (21 in total). Properly combined, they will allow for tuning roughly the following frequencies: 37.5, 50, 75, 100, 150, 200, 300, 400, 600, 800, and 1200 kHz. These values were

primarily selected for MIEZE setups with equal distances L_1 and L_2, because all values have a counterpart differing by a factor of 2. But they should also provide a reasonable variety to choose from for normal NRSE measurements and other MIEZE configurations.

For frequencies smaller than 37.5 kHz the Bloch-Siegert shift becomes noticable. The upper limit of 1200 kHz is mainly connected to the maximium possible B_0 field (i.e. the respective DC currents) and to a certain degree also to an increased heat production caused by the skin effect.

2.8.3 The DC Power Supplies

The DC power supplies must provide a current which is both high enough to produce the respective B_0 fields, and sufficiently stabilized to ensure that the phase, which the neutrons accumulate when passing, is almost identical for all neutrons in the beam and for all times. Due to the low resistance of the coils ($R \approx 0.8\ \Omega$), the voltage is not a limiting or critical factor.

The required stability of the DC current follows from the estimation of the required field homogeneity (s. section 2.2.4.1). Since the variation of the magnetic field should not exceed $\approx 10^{-4}$ and the flux density is proportional to the current, roughly the same requirement applies to the DC power supplies for the residual ripple of the current output.

Figure 2.26: DC power supplies: Heinzinger PTN 3p 80-80 (left) and FUG NTN 14000M-125 (right).

The devices used for the Multi-MIEZE measurements were a Heinzinger PTN 3p 80-80 (80 V/80 A) and a FUG NTN 14000M-125 (125 V/100 A). They are highly stablilized and comply with these requirements. The latter was kindly provided by the RESEDA team, the first will continued to be used for the permanent NRSE/MIEZE measurement options at MIRA.

3

Measurements and Results

The Multi-MIEZE measurements took place at the instrument MIRA in late 2005 and beginning of 2006. Fig. 3.1 shows the setup with the Mu-metal shielding of the two MIEZE levels, containing two bootstrap resonance flipper coils each. Also visible are the polarization analyzers, the C-boxes used for adapting and tuning the resonant circuit, and the scintillation detector in its polyethylene shielding (the rack containing the RF synthesizers and amplifiers is missing in the picture). The overall length of the assembly was approximately 6 m, taking up all the available space at MIRA.

The first beam time was primarily used to characterize the coils, test the equipment and conduct first single MIEZE measurements. During the second beam time periods in January and February 2006, the whole setup had to be installed again and Multi-MIEZE measurements were performed.

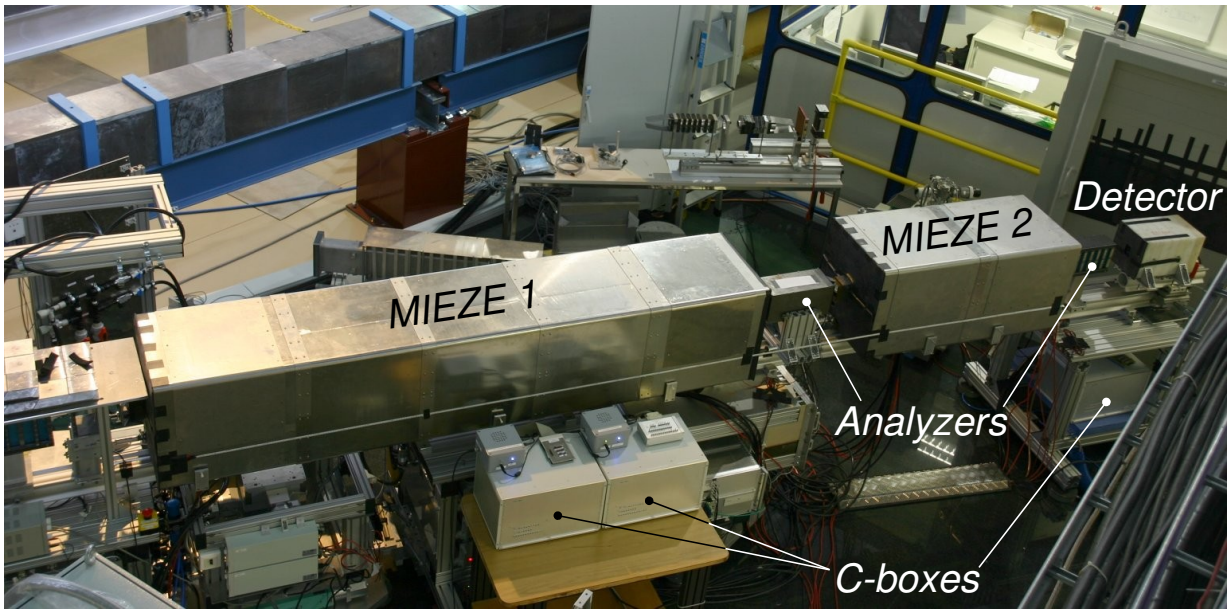

Figure 3.1: Overview of the Multi-MIEZE setup at MIRA.

3.1 The Instrument Configuration

To obtain relatively simple geometric conditions for the coil and detector distances $L_{11,12}$ and $L_{21,22}$, a frequency ratio ω_{Bi}/ω_{Ai} of 2 for the MIEZE stages was chosen. That means, according to Eq. (1.156), the respective distances are approximately equal, i.e. $L_{11,12} \approx L_{21,22}$ (see Fig. 3.1).

The Capacity Adaption Boxes were designed for frequencies that are multiples of 50 kHz. It was decided that all measurements will be conducted at frequencies of $f_{A1} \approx 50$ kHz (coil BS1), $f_{B1} = f_{A2} \approx 100$ kHz (BS2 and BS3) and $f_{B2} \approx 200$ kHz (BS4). The second coil of the first and the first coil of the second MIEZE setup had to be run at $f_{A2} = f_{B1} \approx 100$ kHz. This constraint arose from the situation that for the middle coil pair the same electronic equipment had to be used.

The above values allowed on the one hand for the usage of a current-limited (but sufficiently stabilized) DC power supply that was already available at MIRA, and on the other hand for DC currents at which the B_0 coils could be operated without cooling. Tuning and operating a MIEZE instrument is also generally easier at lower frequencies.

It turned out that the resonant circuits could be well adapted (low reverse power) to frequencies of 54.5 kHz, 109 kHz, and 218 kHz.

The distances were restricted by the dimensions of the Mumetal shielding, the possible positions of the coil positioning system, and the space needed by the polarization analyzers. For the measurements they were set to $L_{11,12} = 2.4$ m and $L_{21,22} = 0.8$ m.

The coupling coils were operated with a current of 0.5 A, producing a field of ≈ 4.5 G in the center and ≈ 6 G at the current sheet side. This was sufficient to reliably turn the polarization vector into the x-y plane and perpendicular to the B_0 field.

3.2 Characterization of the NRSE Coils – Determining the π-flip and Resonance Condition Parameters

As described in section 1.1.4.1 the boostrap coils must be tuned to meet the resonance and π-flip conditions Eqs. (1.81) and (1.82), i.e. the radio frequency and static fields must be set to values at which the neutron spin performs a resonant π-flip in each RF/DC field area.

This is normally tested by letting the neutron beam pass the coils with the polarization in $+z$-direction (instead of $+x$-direction for normal operation). If the coils operate at the correct parameters, the polarization is π-flipped around the RF field vector from $+z$ to $-z$. This easy to comprehend when looking at the field configuration in a coordinate system rotating with the RF frequency (cp. section 1.1.4.1). Then in the case of resonance, the B_0 field vanishes and the RF field is static. The result of the polarization being flipped from up to down is an intensity minimum at the detector (zero in the ideal case) since the analyzer is set to transmission for $+z$ polarization. If the coils are detuned, i.e. not driven at the correct parameters, the beam becomes depolarized. To achieve the aforementioned, the coupling coils, which turn the polarization adiabatically and guide it into the zero-field region inside the shielding, are normally rotated about 90° so that their field in the inside is also pointing in $+z$-direction, thus acting as a guide field. Due to technical constraints, this is not possible at MIRA.

As an alternative, we switched off the coupling coils and made the guide field from the first polarizer to the coupling coils suffciently strong. That way it was possible to preserve the initial polarization up to a degree still allowing to measure the correct π-flip/resonance parameters.

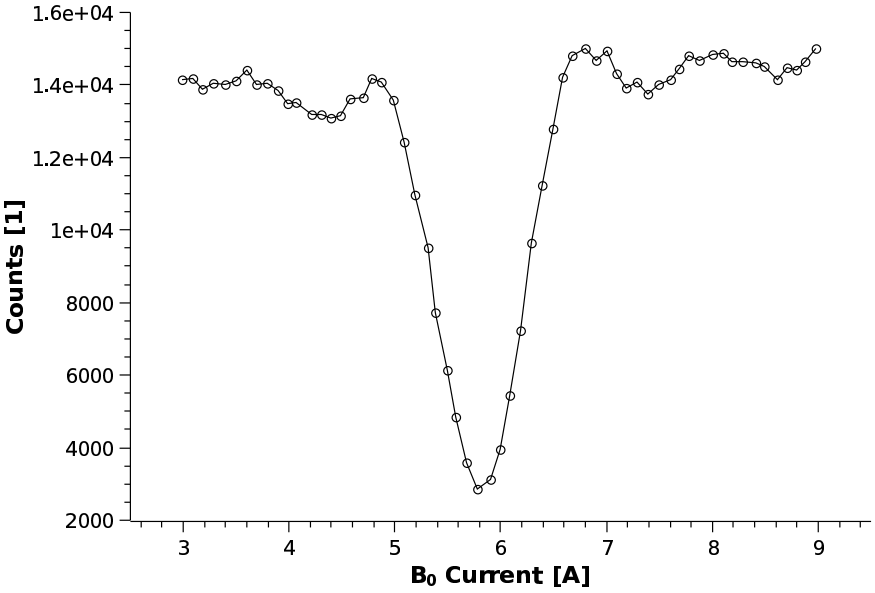

Figure 3.2: π-flip scan of DC current (B_0 field) at a given RF amplitude with the incoming polarization in $+z$-direction. The minimum corresponds to a π-flip from $+z$ to $-z$ and defines the DC current matching the RF frequency.

Fig. 3.2 shows such a DC current scan at a given RF amplitude. The location of the minimum indicates the correct DC current value at which the π-flip happens.

A different approach that does not require the coupling coils to be rotated, and which is therefore more appropriate for the situation at MIRA, was proposed by W. Häußler [12]. By performing a 2D scan of DC current and RF amplitude over a wide range of both parameters, each coil can be tested separately even if the coupling coils are installed in their normal orientation and switched on.

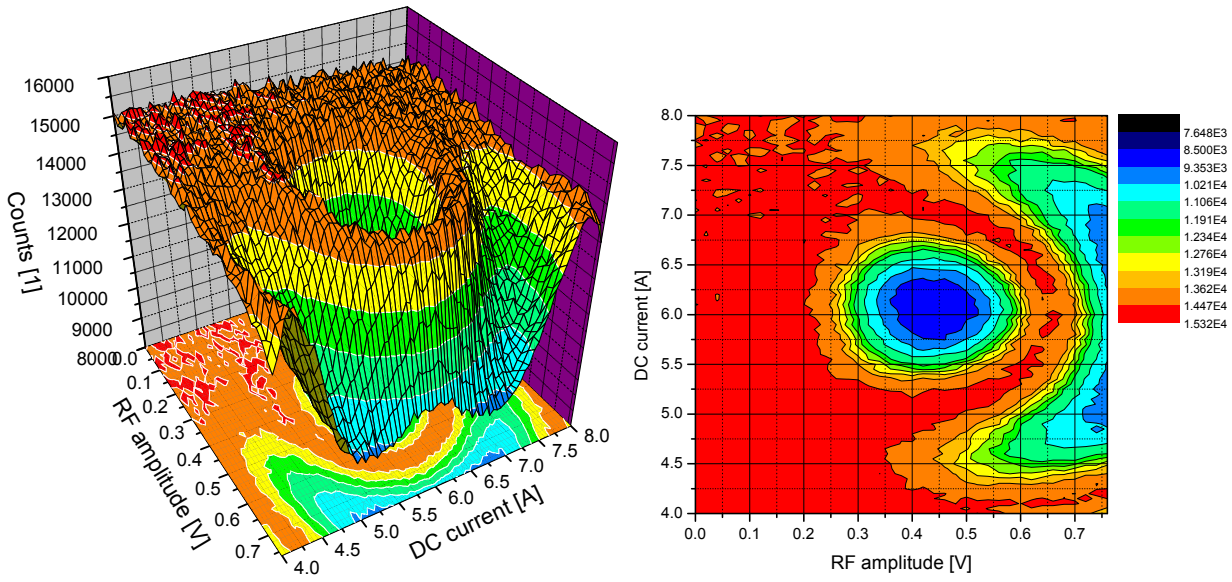

Figure 3.3: 3D surface (left) and contour plot (right) of a DC current versus RF amplitude scan of bootstrap coil BS3 with the incoming polarization in $+x$-direction. The resonant π-flip happens at 6.1 A *and 0.45* V*.*

Bootstrap Coil	Frequency [kHz]	DC Current [A]	RF Synthesizer Output Level [V]
1	54.5	3.1	0.45
2	109	6.2	0.45
3			
4	218	12.3	0.45

Table 3.1: Field parameters of the four resonance flippers depending on the frequency.

What happens is that at the correct tuning point of DC and RF current (i.e. field amplitudes), the neutron spins are resonantly flipped but staying inside the x-y plane. The phase of the RF field vector, i.e. its angle with respect to the spin, changes for neutrons in the beam that enter the coil at different times. Hence, the orientation of the spins at different times is distributed in the x-y plane and the beam becomes effectively depolarized. Therefore, after the analyzer the measured intensity at the detector for a certain measurement time Δt is half the initial (polarized) intensity in the case of resonance. Fig. 3.3 shows such a scan of coil BS3 with all other resonance flippers turned off. The correct field parameters are clearly identifiable by the minimum at 6.1 A and 0.45 V.

For very small RF field amplitudes the polarization does not change significantly with increasing B_0 field. When the correct amplitude is approached and the resonant π-flip happens, the above mentioned minimum forms. If the amplitude reaches the point where the spins perform a 2π-flip, the initial polarization is nearly recovered. When the amplitude becomes three times as strong, another intensity minimum appears (3π-flip). This is not entirely visible in Fig. 3.3, since for our purpose of finding the correct field parameters such a large scan range was not required (see [12] for a more extensive scan). Please note that the RF current output of the amplifier and hence the B_1 field strength do not go linear with the signal provided by the frequency synthesizer.

The side minima which occur with an increasing B_0 field for a given RF amplitude are only indicated here and would also appear more clearly if the scan would be performed over a wider range. These minima are caused by more complex interactions of B_0 and B_1 (incomplete vanishing of the diagonal elements in the time-evolution operator; see also [12] for details).

The next step after determining the appropriate field parameters of each coil for a given frequency (summarized in Table 3.1) is scanning the coil postions and then starting the actual MIEZE and Multi-MIEZE measurements.

3.3 Tuning of the Single MIEZE Levels

Before both MIEZE setups could be run together, each one had to be tuned to produce the sinusoidal, time-dependent signal as described in section 1.3. After determining the proper field amplitudes B_0 and B_1 for each coil (see previous section), the data depicted in Fig. 3.4 was collected (measuring time: 1800 s).

Since the count rate was sufficient and to improve the signal contrast, a Boron aperture of 1 cm^2 was placed after the last analyzer to suppress the counting of neutrons with noticeably different path lengths ($\rightarrow$ beam divergence).

At the time the measurements were performed the coil positioning system was a non-

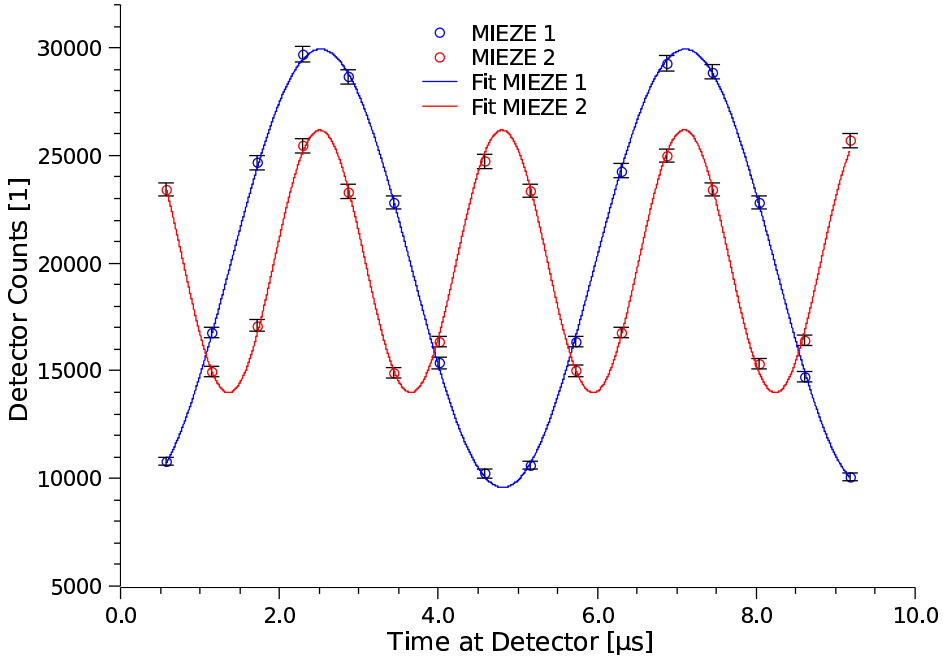

Figure 3.4: The independently measured signals of the first (54.5/109 kHz*) and second (109/218* kHz*) MIEZE level, including fits. Measurement time: 1800s*

motorized, non-commercial solution and the positions had to be scanned manually with reduced precision. Therefore, we estimate the longitudinal position accuracy to be within the mm range. The rotation of the coils was set merely by visual judgement since the beam time did not allow for another extensive and time-consuming manual scan of all four coils. This situation, however, has been resolved in the meantime, all coils are equipped with precision linear and rotation tables including stepping motors.

The signal contrasts $C_1 \approx 51.5\%$ and $C_2 \approx 30.4\%$ are obviously not ideal and were a lot lower than expected from the good π-flips measured for the coils. Although no obvious sources of depolarization could be found, several possibilities were considered:

- Stray fields from the coils that were not absorbed by the missing Mu-metal coil case
- A remaining magnetic field component in the zero-field region due to an insufficient shielding factor (single-layer shielding)
- Suboptimal coil alignment (tilting, rotation)
- Non-homogeneous DC fields, damaged Mu-metal yokes
- Coupling coil effects
- Detector efficiency and scintillator crystal thickness

Whether or not any of the above listed points really had a noticable effect could not be investigated deeper, neither would it have been possible to eliminate them due to technical constraints or lack of time. However, for the main purpose of proving the Multi-MIEZE principle, the suboptimal contrasts were not of critical importance.

When conducting the first regular MIEZE measurements at MIRA, the main factor for the polarization losses could be identified to be a longitudinal field component inside the magnetic shielding. We will elaborate on this further in section 3.5.

The multi-channel analyzer card (16 channels) was triggered by another RF synthesizer, which is phase-locked with the synthesizers feeding the RF coils. Since the MIEZE signal frequency is $2\,N\,(\omega_B - \omega_A)$ and the coils were operated in bootstrap mode ($N = 2$), it had to provide a frequency of $f_{MCA} = 2 \cdot 2 \cdot 16 \cdot 54.5$ kHz$= 3.488$ MHz to record one sinusoidal signal period.

3.4 Two-level Multi-MIEZE Measurements – Verification of the Multi-MIEZE Principle

For MIEZE to work, the phases of the two involved resonance flipper coils must be locked, i.e. they must have a constant difference. Otherwise the accumulated phase of the wave function at the detector has additional time-dependent terms which cannot be cancelled and destroy the polarization. This was easily provided by the so-called phase-lock option of the RF synthesizers (see section 2.8.1), which offers the possibility to run all connected devices on one reference oscillating quartz. Fig. 3.5 shows a snapshot of the oscilloscope display with the phase-locked input signals for all three frequencies.

A similar prerequisite holds for the stages of a Multi-MIEZE setup: the sinusoidal oscillations of each level must have the „right“ RF phase relation for the signals to overlap correctly at the detector and produce the predicted signal form. If the phasing is detuned, the peaks are misaligned and do not superpose constructively. We also recorded such a detuned signal, which is plotted in Fig. 3.7. To achieve the correct superposition, the phases could be easily shifted agains each other by the phasing adjustment functionality of the RF synthesizers. After tuning the single MIEZE stages as described in the previous sections and adjusting them to have the same detector position, both were switched on together.

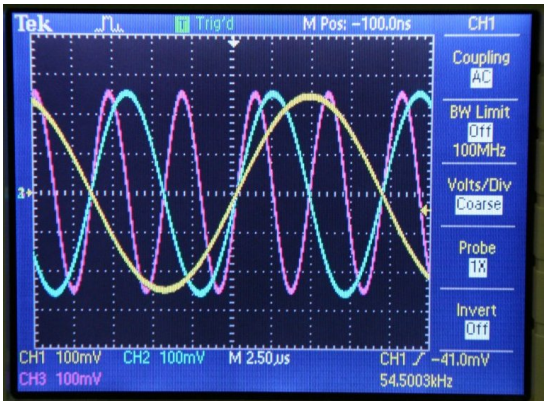

Figure 3.5: Oscilloscope display with the phase-locked input signals.

In section 1.4 we derived the expected signal form Eq. (1.170) of a Multi-MIEZE setup. The data obtained in the measurements must now be fitted with the respective intensity distribution function to be able to either verify or disprove the principle.

Eq. (1.170) represented the signal in the ideal case, i.e. without loss of polarization or intensity caused by non-perfect coil or stray fields, absorption, and scattering caused by material in the beam. In real measurements, however, this will happen to some extent and the initial intensity I_0 will not be preserved in the maximum of the Multi-MIEZE signal.

Based on Eq. (1.170), the model used for fitting the Multi-MIEZE data is

$$\begin{aligned} I(t_\mathrm{D}) &= \frac{I_0}{2}\left[1 + C_1\,\cos(2\,N(\omega_{\mathrm{B1}} - \omega_{\mathrm{A1}})\,t_\mathrm{D} + \varphi_1)\right]\times \\ &\quad \frac{1}{2}\ \left[1 + C_2\,\cos(2\,N F_\mathrm{M}\,(\omega_{\mathrm{B1}} - \omega_{\mathrm{A1}})\,t_\mathrm{D} + \varphi_2)\right] \\ &= I_0 \prod_{\nu=1}^{2} \frac{1}{2}\left[1 + C_i\,\cos(F_\mathrm{M}^{\nu-1}\omega_{\mathrm{M1}}\,t_\mathrm{D} + \varphi_i)\right], \end{aligned} \tag{3.1}$$

where the fitting parameters are I_0 (initial beam intensity), $C_{1/2}$ (signal contrasts), and $\varphi_{1/2}$ (signal phases). The constants $N = 2$, $F_\mathrm{M} = 2$, and $\omega_{\mathrm{M1}} = 2N \cdot 2\pi \cdot 54.5$ kHz are the bootstrap and MIEZE factors, and the modulation frequency of the first MIEZE level, respectively. They have been introduced and explained in section 1.4.

Eq. (3.1) is the equivalent to Eq. (1.170) for non-ideal intensity distributions where the cosine part is weighted with the respective signal contrast $C_{1/2} < 1$.

The fitting curve is plotted in Fig. 3.6 along with those for the single MIEZE signals, and Table 3.4 lists the results of the fitting procedure. The non-linear fitting was done using a scaled Levenberg-Marquardt algorithm without weighting (tolerance 10^{-4}). The respective results for the fitting of both single MIEZE signals can be found in Appendix A.4. The fitting results based on Eq. (3.1) match the data distribution very well. For better comparison, Fig. 3.8 shows the scaled (normalized) first single together with the Multi-MIEZE signal. Besides the good match with the predicted intensity function, the peak sharpening becomes obvious.

Parameter	Fit result
I_0	79332.0 ± 1.0
C_1	$0.52583 \pm 2 \cdot 10^{-5}$
C_2	$0.29641 \pm 2 \cdot 10^{-5}$
φ_1 [rad]	$2.85363 \pm 4 \cdot 10^{-5}$
φ_2 [rad]	$-0.51719 \pm 6 \cdot 10^{-5}$
R^2	0.996988
χ^2/doF	396591

Table 3.2: Fitting model parameters and results for the Multi-MIEZE data.

In a previous Multi-MIEZE measurement we accidently recorded a signal with a phase relation between the two MIEZE stages that was not correctly tuned. The intensity distribution is plotted in Fig. 3.7 and is of course unusable for experiments. However, it too can serve as prove for the Multi-MIEZE principle by fitting the data with our fitting model Eq. (3.1). Like for the correctly tuned signal, the fitting curve is in almost perfect agreement with the data.

In section 1.4.1 we defined the quantity M („Multi-MIEZEity“) as a measure for the quality of a Multi-MIEZE signal and as an analogon for the contrast C of a single MIEZE. From the fits of the signal recorded in our measurements we obtained contrasts of $C_1 = 0.526$ and $C_2 = 0.296$, which yields $M = 0.395$.

In addition to the statistical errors, we would like to discuss the effects of three sources for systematic errors:

i) misalignment of the phases $\varphi_{1,2}$ of two MIEZE signals at the detector (cp. section 3.4 and Eq. (3.1))
ii) non-perfect π-flips in the first and second coil of a MIEZE level
iii) influence and consequences of a finite detector thickness

The first effect can be influenced and tuned very easily by manually shifting the phases of the RF signals at the frequency synthesizer. This was done prior to the Multi-MIEZE measurements,

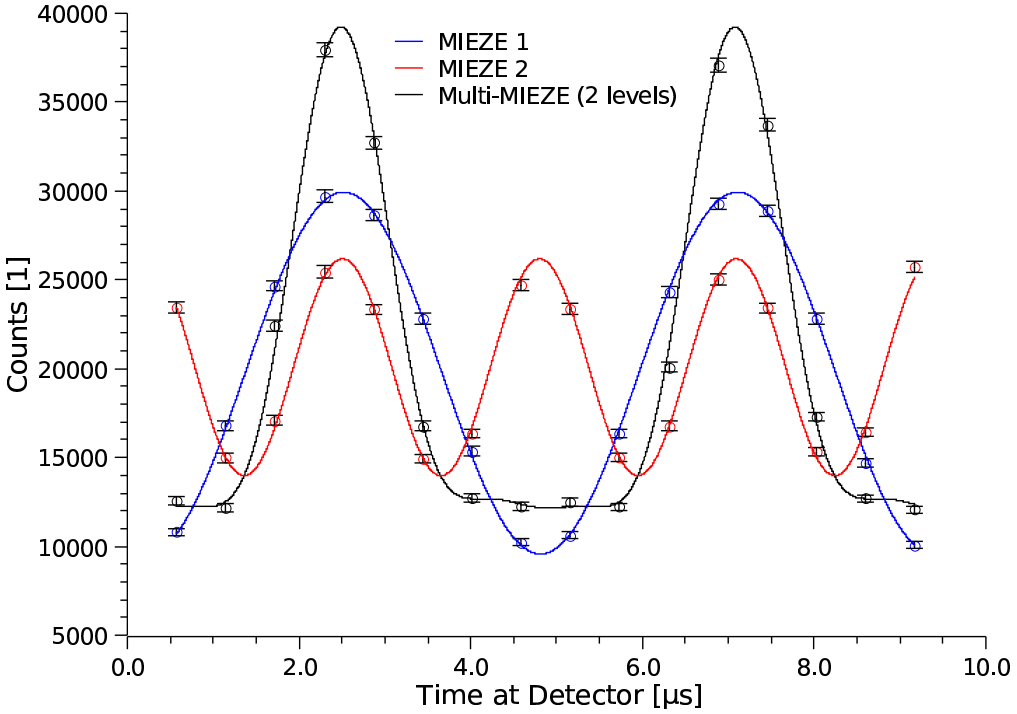

Figure 3.6: Single and Multi-MIEZE data with fits (statistical error range: 2 σ). The non-linear fitting model of the Multi-MIEZE data matches the predicted intensity distribution very well. Measurement time: 1800 s (single MIEZE), 3600 s (Multi-MIEZE).

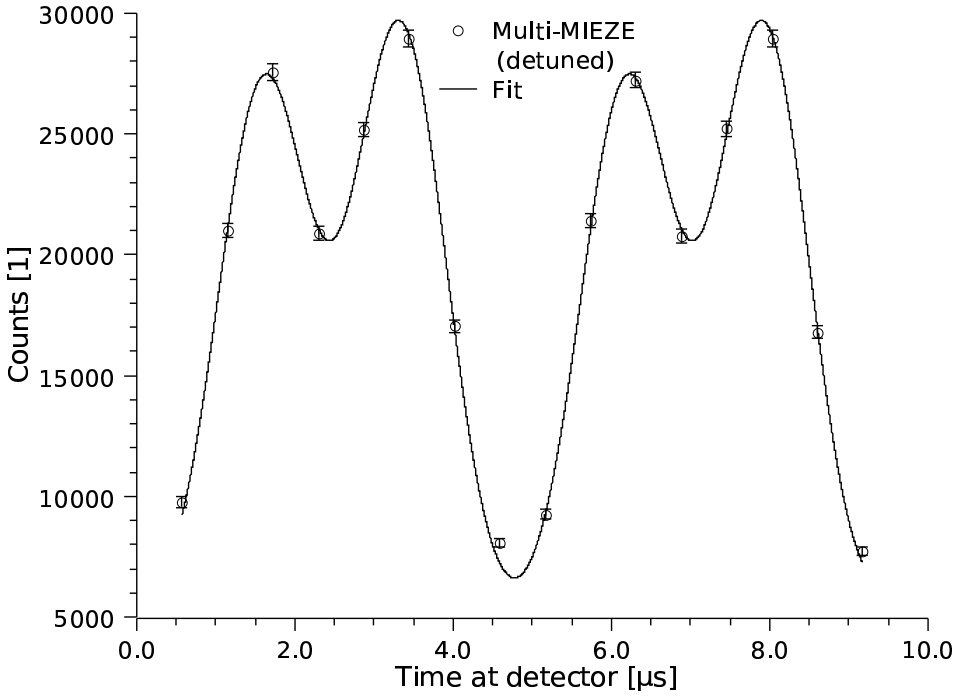

Figure 3.7: Data plot and fit of a detuned Multi-MIEZE measurement. Again the fitting model provides a very good match with the data. Measurement time: 3600 s

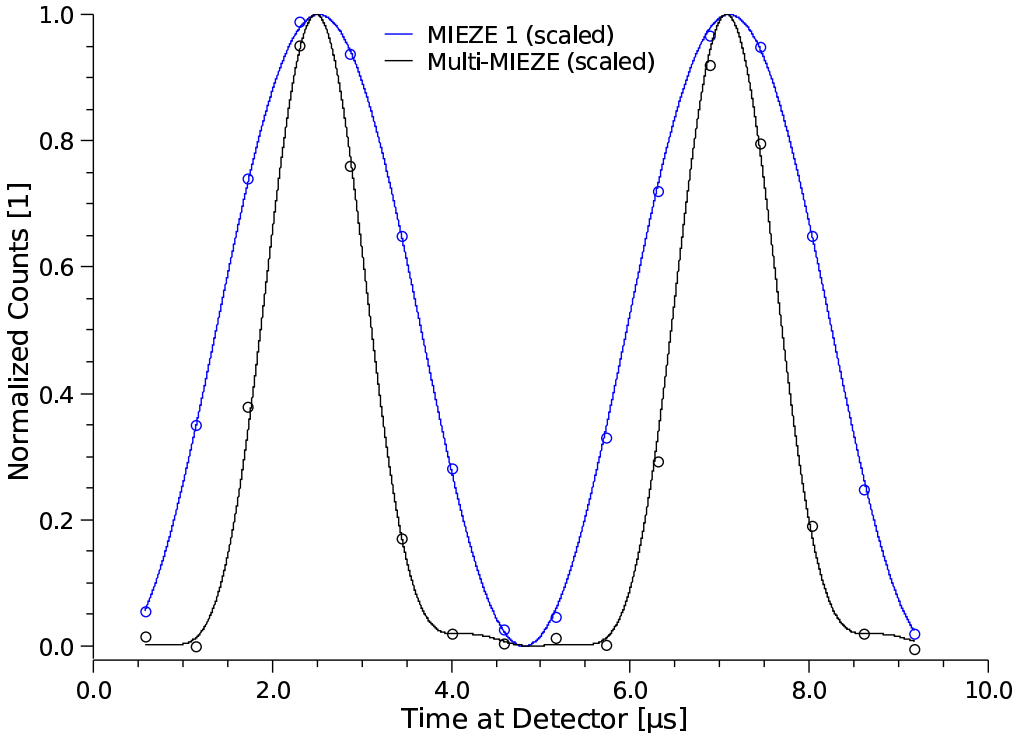

Figure 3.8: First MIEZE and Multi-MIEZE signals, scaled for better comparison.

but for the reason of time saving not with the aid of data fitting tools but in a step by step procedure and the subjective judgment of recorded signals with short measurement times. Therefore, we estimate the uncertainty to be of the order of degrees. The two phases, however, are parameters in the fitting model. Further manual fine-tuning of the parameters would probably result in an even slightly better match of the data.

The second point manifests itself in a beat, which is visible in the MIEZE signal: of two subsequent maxima, one is slightly increased, the other is slightly lower (the same applies to the minima).

To better understand that effect, we should recall the magnetic resonance spin echo technique how it was initially presented by Gähler and Golub in [2]. Here the polarization vector when entering the first coil is pointing in the same direction as the B_0 field (in our case: z), the resonance flippers are tuned to $\pi/2$- instead of π-flips, and the zero-field regions are replaced by low guide fields. An instrument of that kind is actually the direct NRSE analogue to NSE, the spin echo time in that case is $\tau_{\mathrm{NRSE}} = \tau_{\mathrm{NSE}}$ for equally strong static fields (and not increased by a factor of 2).

This scenario transposed to MIEZE would result in a sinusoidal signal with a period a factor of 2 higher or half the modulation frequency: if we have a partially polarized beam with $P < 1$ (so that there is a component P_z in z when entering the coil) and further assume an imperfect π-flip in our resonance flipper, the signal at the detector with frequency $2(\omega_B - \omega_A)$ would be superposed with a small sinusoidal contribution of half the frequency. Such a beat would result in the observed deformation of every second peak.

The effect is detectable in the Multi-MIEZE data, but not in the fits (since it is not accounted for in the fitting model). It becomes even more obvious in the single MIEZE data in Fig. 3.10 and the 3D color plot Fig. 3.11.

The thickness of the detector is an important factor for any MIEZE instrument. The volume in which the neutrons are actually measured is in our case the Germanium scintillator crystal with a thickness of approx. 0.5 mm. The process of neutrons producing a photon in the crystal, which is then detected by the photo multiplier, happens at different locations. Most neutrons will interact within a certain small area at the beginning of the crystal. The distribution function describing the absorption along the flight path through the crystal probably resembles an exponential-like decrease (see illustration on the right). In principle, the sinusoidal MIEZE signal must be convolved with that absorption function and integrated over the respective time interval since the accumulated phases of the spin-up and spin-down states will only be equal at a certain position. Neutrons that are measured outside that plane will contribute to a contrast decrease.

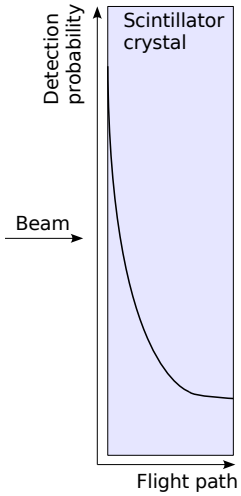

In addition, if the convolution function is not constant the resulting signal would not be a pure cosine anymore, causing a non-symmetric signal distortion. This introduces a systematic error for the (Multi-)MIEZE signal which is very complex to quantify and also not considered in the fitting model.

We should mention here that this detector requisite is one of the limiting factors of the MIEZE technique, since even for a perfectly monochromatic beam with an infinite coherence length the phase relation of spin-up and spin-down at the point of detection is relevant.

A detector system that circumvents the problem of a not well-defined detection plane is CASCADE, which is a promising alternative to fast scintillators for MIEZE and would also be able to provide 2D spatial resolution. It uses an implementation of boron coated converter layers for detection, each with a thickness in the µm range. The effective detection volume and hence the efficiency is increased by using several subsequent of these layers. For more information on CASCADE we refer to [31, 32].

Coming back to the key question of this section and the work at hand, we can say that the evaluation of the collected data supports the conclusion that the Multi-MIEZE principle can be considered verified.

3.5 First MIEZE Measurements at MIRA

In late 2006 the MIEZE equipment was installed at MIRA basically in the configuration in which it will be used as a standard measurement option. Fig. 3.9 shows the setup at MIRA. The main purposes of the measurements were

i) to test the MIEZE equipment and to detect possible problems when it is installed as a standard option, i.e. when all parts are integrated into the existing instrumental infrastructure of MIRA. This concerns mainly the required space for the Mu-metal shielding, the coupling coils, guide fields, and the polarization analyzer in relation to the sample region. The latter still must provide enough space for bulky equipment like the cryostat and/or the magnet, and the rotation or tilting of the sample table must not be restricted.

ii) to show that MIEZE is a technique suitable for complex sample environments (like ferromagnetic samples, high or low temperature environments, strong magnetic fields, etc.), which can be installed at conventional NSE or NRSE instruments, if at all, only with considerable effort.

When planning a MIEZE setup for either an existing or a dedicated instrument, the desired resolution (MIEZE time τ_{M}) and possible measurement configurations and geometries must be taken into account. This defines important parameters like coil distance and Mu-metal shielding dimensions, as well as sample environment and detector positions.

By combining Eqs. (1.156), (1.162) and (1.163) (and neglecting the coil thickness D for simplicity) we obtain for the MIEZE time

$$\tau_{\mathsf{M}} = 2\,N\,\omega_{\mathsf{A}}\,L_1\,\frac{\hbar}{m\,v_0^3}\,. \tag{3.2}$$

Therefore, in principle the coil distance L_1 and the frequency of the first coil ω_{A} define the

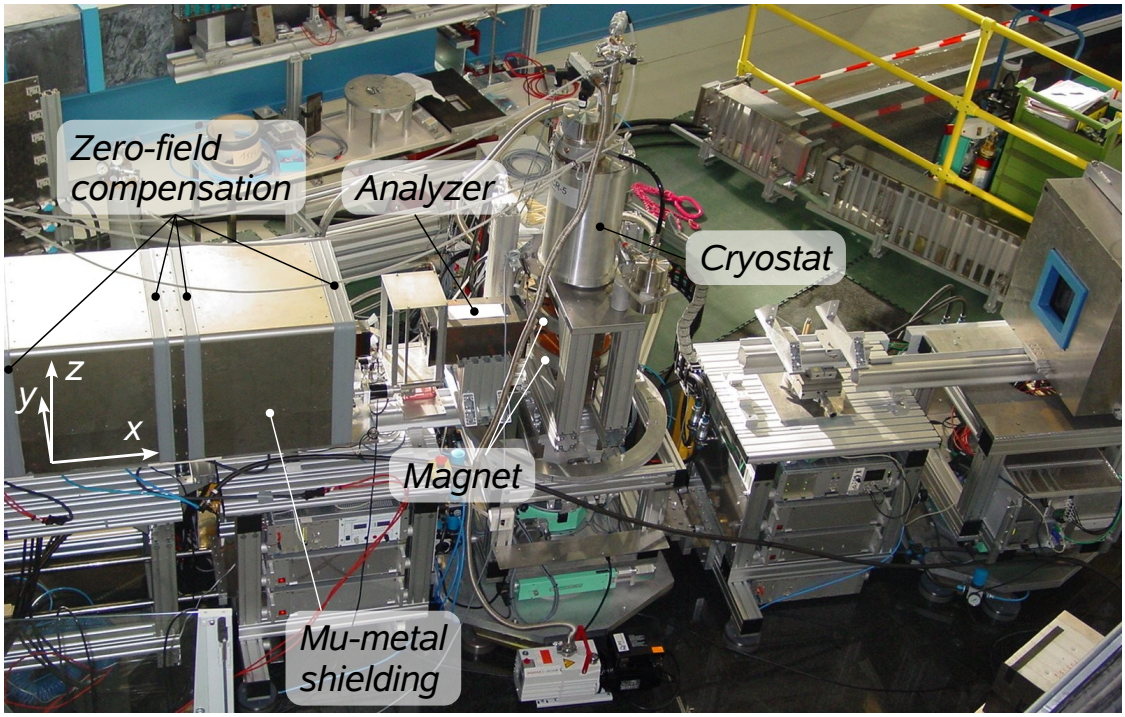

Figure 3.9: MIEZE setup at MIRA with a sample region consisting of a cryostat and a 0.25 T magnet. When the picture was taken the detector was temporarily unmounted.

resolution parameter τ_M. The detector distance L_2 can be chosen according the the geometric constraints of the instrument or requirements of the measurement setup, e.g when a SANS measurement requires a large sample-detector distance. The frequency ω_B of the second coil then follows from that choice according to Eq. (1.156).

These considerations apply in particular to MIRA, which is a versatile instrument that includes, besides other instrumental options, also the possiblity for reflectometry and SANS measurements. Therefore, different measurement geometries and resolutions are required for a large variety of samples and sample environments. Here the MIEZE technique does not only expand the set of scattering tools at MIRA by adding the possibility of spin echo-like measurements of dynamics, but with the flexibility described above it can also extend the established scattering methods, e.g. by adding energy resolution to small angle scattering experiments.

The sample environment location between the two arms of MIRA is fixed and cannot be altered. Instead, the whole instrument was shifted from the monochromator by inserting extension rods, thus gaining space for guide fields and the polarization analyzer. We placed a 0.25 T magnet and a cryostat at the sample region, which in principle does not need any magnetic shielding since the MIEZE signal modulation is already prepared at the analyzer. The flipper coils were running at frequencies of $\omega_\mathsf{A} = 59$ kHz and $\omega_\mathsf{B} = 88.5$ kHz (non-boostrap, $N = 1$), the coil distance was $L_1 = 0.8$ m, and the sample-detector distance was set to $L_\mathsf{s} = 0.8$ m. For 10 Å neutrons, this resulted in a MIEZE time of τ_M=0.3 ns, which corresponds to a resolution in energy of 2.2 μeV.

Plotted in Fig. 3.10 is the MIEZE signal without the magnet switched on. Compared to previous measurements, the contrast could be improved significantly to approx. 80% with an initial polarization of 93%. The main reason for the polarization loss was obviously a remaining longitudinal field component in the magnetic shielding. With more beam time available, the effect could be determined by installing a DC mode option for the RF coils, thus having them produce a DC field in y-direction (cp. coordinate system in Fig. 3.9). If the polarization vector (which is likewise turned from z- to y-direction by the coupling coils) undergoes Larmor precession in the y-z plane caused by a longitudinal field, it would be rotated out of the y-z plane by the DC field inside the RF coils when passing them. This becomes noticable by a significant intensity decrease after the analyzer.

As a countermeasure the Mu-metal boxes were equipped with a compensation coil consisting of 10 windings around the longitudinal axis, attached on the outside. They are visible as grey stripes in Fig. 3.9. By scanning the current through this compensation coil and measuring the polarization following the method described in the previous paragraph, the correct parameters for a given external magnetic field environment can be determined.

The MIEZE experiment consisted in recording of the signal for different fields of the sample environment magnet. Although a magnetic field that is applied downstream the analyzer does not alter the signal in principle, there is the possibility that the strong external solenoid fields could influence the zero-field region or the coil fields inside the shielding. However, we could not observe a noticeable influence for a magnetic flux density up to approx. 2.5 kG ($\widehat{\approx}$ 245 A). The 3D plot in Fig. 3.11 shows the time-modulated signal as a function of the magnetic field at the sample environment (1 A $\widehat{\approx}$ 10.2 G). The signal contrast is basically unaffected, which demonstrates the ability of MIEZE to provides means to measure dynamics in physical systems that require to be prepared in the aforementioned environments.

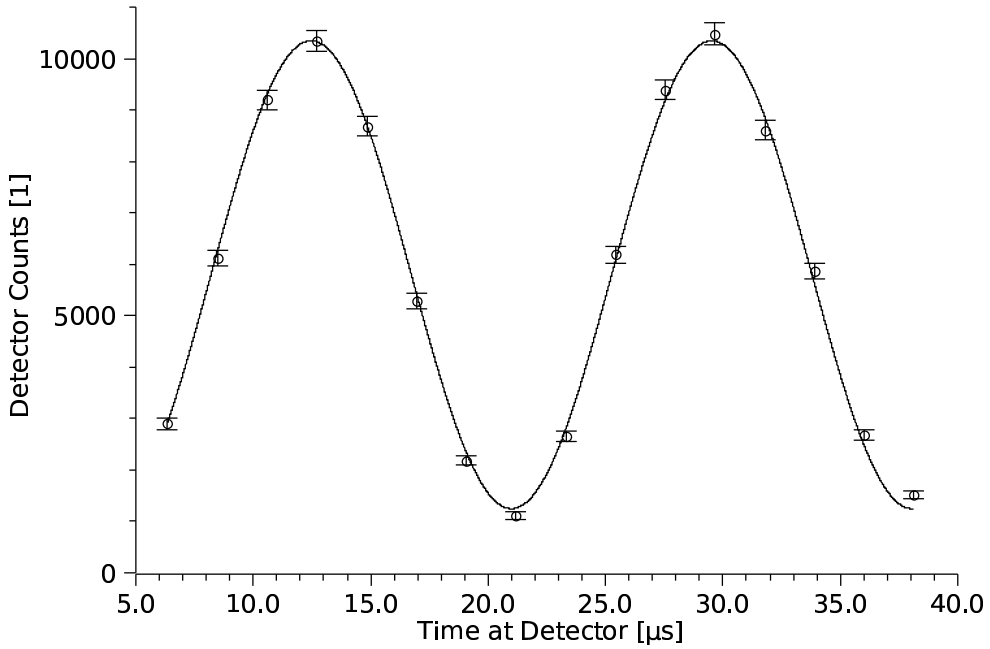

Figure 3.10: Data fit of the MIEZE signal from first regular measurements at MIRA (top) and plot of a 2D scan of MIEZE signal versus solenoid current (bottom). The initial polarization is basically unaffected by an increased external field at the sample position.

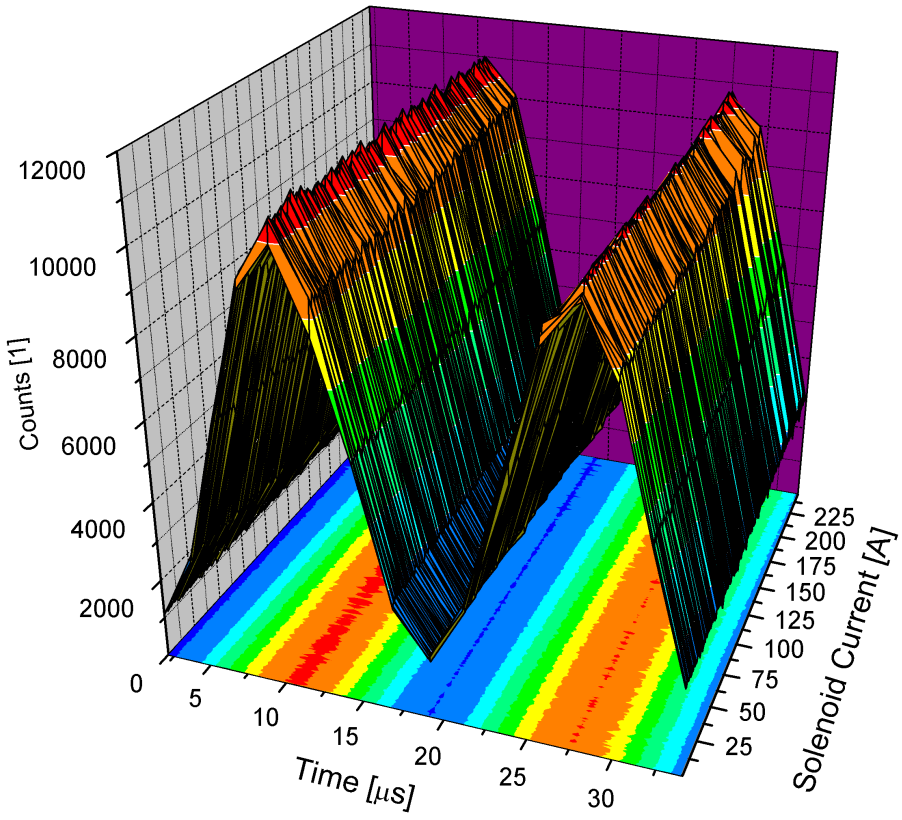

Figure 3.11: Data fit of the MIEZE signal from first regular measurements at MIRA (top) and plot of a 2D scan of MIEZE signal versus solenoid current (bottom). The initial polarization is basically unaffected by an increased external field at the sample position.

3.6 First NRSE Measurements at MIRA

Prior to the MIEZE setup the NRSE option was tested during a proposal beam-time that included resonance spin echo measurements at MIRA. The second Mu-metal shielding was reassembled in order to have the same dimensions than the first. The coil distance was set to 0.8 m, together with a frequency of 69 kHz (non-bootstrap) this yields a spin echo time $\tau_{\mathrm{NRSE}} = 0.6$ ns ($\widehat{\approx} 1.1$ μeV).

Since no dedicated zero-field shielding for the sample region existed, the latter was at first installed in a guide field instead. This approach results in a 50% loss of polarization in principle and made any measurements difficult, complicated further by the additional depolarization due to a remaining longitudinal field in the coil shielding.

Therefore, further efforts were put into installing a provisional zero-field sample environment from a spare Mu-metal box (originally meant for a third Multi-MIEZE stage) as well as the compensation windings for the shielding (s. section 3.5 and Fig. 3.9). This improved the situation distinctly, Fig. 3.12 shows the resulting spin echo group we recorded ($P \approx 75\%$).

We should note that this scan was performed in an unusual way by altering the RF frequency in the second arm (plotted on the abscissa). Normally the coil position is shifted, thus changing the effective field integral in the second arm. This was not possible at the time, since the motors and encoders could not be delivered in time for the measurements. Although in principle a spin echo group can be obtained in the fashion we did, it will also cause a slight detuning of the coils since we left B_0 unchanged, resulting in a small depolarization left and right of the spin echo point.

For us the recorded spin echo group was encouraging prove that i) the instrumentation that was built is indeed working and ii) that at MIRA, although no dedicated instrument, resonance spin echo measurements are possible in the future. There are still several technical aspects that need to be improved or resolved, and we will list the most important of them in the outlook. With those technical improvements, we also hope to further enhance the resolution of the instrument (higher frequencies, i.e. higher spin echo times) without significant polarization losses.

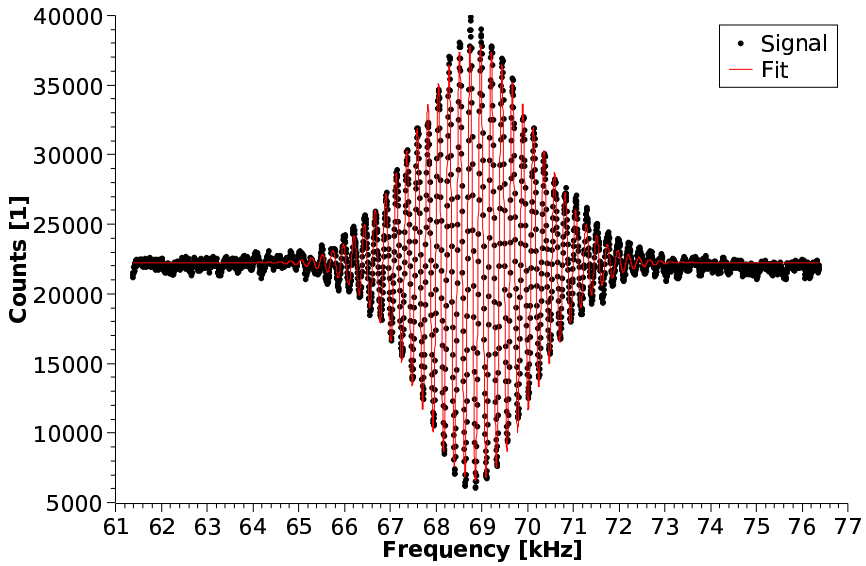

Figure 3.12: First signal from an NRSE setup with provisional zero-field sample environment. The spin echo group has been recorded by altering the RF frequency instead of the coil position.

4

Applications for MIEZE and Multi-MIEZE

This chapter presents a selection of applications and experiments making possible use of the (Multi-)MIEZE technique in neutron science. The presentation of the concepts here is not meant to be complete in every detail of the respective topic, but shall rather give an impression of the possibilities and the potential of MIEZE and Resonance Spin Echo techniques.

4.1 Interferometry Using Wave Packets

We have proven earlier in this thesis that a Multi-MIEZE instrument is capable of producing short neutron pulses like a very fast chopper. By increasing the number of MIEZE levels the pulse width can be narrowed. But unlike a mechanical chopper, the Multi-MIEZE signal is a beat at a specific position, resulting from a properly tuned superposition of time-dependent signals. Thus, the wavelength distribution of the pulse – or, in a qantum-mechanical term, the wave packet – is not defined by the uncertainty relation of momentum and space (the latter being defined by the chopper wheel), but still by the initial wavelength band of the neutron beam, which depends on „external“ factors like the neutron source itself, the neutron guide, etc. Therefore, there is no broadening of the k-vector distribution.

Such a signal is well suited for experiments in fundamental physics. Here we would like to sketch the possibilities of two interferometric applications.

4.1.1 Measuring the Longitudinal Stern-Gerlach Effect

In [33] the author has presented a possibility to directly observe the longitudinal splitting in energy and momentum of the two spin states like it is caused by a resonance flipper. This is known as the longitudinal Stern-Gerlach effect and, as we will show in the following, it can be measured using the signal of a Multi-MIEZE setup.

First we will derive the solution for a Gaussian-shaped wave packet passing a resonance flipper. An initial spinoral wave packet $\psi_\mathsf{i}(y,t)$ whose momentum is centered around k_0 reads

$$\psi_\mathsf{i}(y,t) = \begin{bmatrix} \psi_\mathsf{i}^+ \\ \psi_\mathsf{i}^- \end{bmatrix} = \frac{1}{\sqrt{2\pi}} \int_{-\infty}^{+\infty} a(k-k_0)\, e^{i(ky-\omega t)} \begin{bmatrix} 1 \\ 1 \end{bmatrix} \mathrm{d}k\,, \tag{4.1}$$

where $\omega = \hbar k^2/(2m)$, and $a(k-k_0)$ is a real weight function.

Knowing the solution for an outgoing plane wave after the flipper [13, 33]

$$\psi^{\pm}_{\mathsf{pw}}(y,t) = \frac{-i}{\sqrt{2}}\, e^{\mp i\omega_{\mathsf{L}}\frac{mD}{2\hbar k}}\, e^{i\left[\left(k\pm\frac{m\omega_{\mathsf{L}}}{\hbar k}\right)y-\left(\frac{\hbar k^2}{2m}\pm\omega_{\mathsf{L}}\right)t\right]}\,, \tag{4.2}$$

one can Fourier-transform it to obtain a wave packet representation. This procedure is permissible due to our assumption that the matter wave frequency of the neutron is much larger than the Larmor and RF frequencies $\omega_{\mathsf{L}}, \omega_1$ of the fields of the resonance spin flipper (cp. Eqs. (1.142) and (1.135)). For the two spin components the wave packets are

$$\psi^{\pm}(y,t) = \frac{1}{\sqrt{2\pi}} \int\limits_{-\infty}^{\infty} a(k-k_0)\psi^{\pm}_{\mathsf{pw}}\,\mathrm{d}k\,, \tag{4.3}$$

where $\psi^{\pm}_{\mathsf{pw}}$ is the plane wave solution. In the following we choose Gaussian-shaped amplitudes

$$a(k-k_0) = A\, e^{-(k-k_0)^2 s^2}\,, \tag{4.4}$$

with A being a scale factor. Using the amplitude function Eq. (4.4), the probability amplitude of the initial wave packet Eq. (4.1) yields

$$\psi_{\mathsf{i}}{}^{*}\psi_{\mathsf{i}} = \pi\frac{A^2}{s^2}\, e^{-\frac{y^2}{2s^2}} \tag{4.5}$$

for both spin directions.

If we further make use of the relation $\omega_{\mathsf{L}}\frac{mD}{2\hbar k} = \omega_{\mathsf{L}}\frac{mD}{2\hbar k_0}(1-\frac{k-k_0}{k_0})$, derived from Eq. (2.30) from [34], Eq. (4.3) with the plain wave solution Eq. (4.2) becomes

$$\begin{aligned}\psi^{\pm}(y,t) = \frac{-i}{\sqrt{4\pi}} \int\limits_{-\infty}^{\infty} A\, e^{-(k-k_0)^2 s^2} e^{\mp i\omega_{\mathsf{L}}\frac{mD}{2\hbar k_0}\left(1-\frac{k-k_0}{k_0}\right)}\times \\ e^{i\left\{\left[k\pm\omega_{\mathsf{L}}\frac{m}{\hbar k_0}\left(1-\frac{k-k_0}{k_0}\right)\right]y-\left[\frac{\hbar k^2}{2m}\pm\omega_{\mathsf{L}}\right]t\right\}}\,\mathrm{d}k\,,\end{aligned} \tag{4.6}$$

after passing the flipper coil. The scale factor A has to be determined such that $\int|\psi^{\pm}|^2\,\mathrm{d}y = 1$. The parameter s has the dimension of length and determines the spatial width of the Gaussian-shaped pulse. D is the width of the field region.

After integrating Eq. (4.6), the probability amplitudes of the outgoing wave packets are

$$\begin{aligned}(\psi^{*}\psi)^{\pm} = \frac{A^2 m}{2\sqrt{4m^2s^4+\hbar^2t^2}}\times \\ \exp\left\{\frac{-s^2\left[Dm^2\omega_{\mathsf{L}} \mp 2\hbar^2k_0^3 t \pm 2m\left(\hbar k_0^2 - m\omega_{\mathsf{L}}\right)y\right]^2}{2\hbar^2k_0^4\left(4m^2s^4+\hbar^2t^2\right)}\right\}.\end{aligned} \tag{4.7}$$

To be able to observe the longitudinal splitting of the spin-up and spin-down states predicted by Eq. (4.7), neutron pulses with very good monochromacy must be used. Strong spreading (and hence overlapping) of the wave packets must be avoided to be able to distinguish between them. As shown in [33], a value of $\Delta k_0/k_0 = 1.9\cdot 10^{-3}$ would satisfy this condition, but the preparation of such a pulse is challenging. We demonstrate in the following that preparing the

pulse using an ordinary chopper results in insufficient intensity: we assume a neutron source with a double differential flux of $d^2\Phi/d\lambda d\Omega \approx 10^9\ n/(cm^2\,s\,Å\,sterad)$ at 30 Å (from the „Yellow Book“ of the Institute Laue-Langevin, ILL). A required monochromacy of $\lambda_0\Delta k_0/k_0 = 5.7 \cdot 10^{-2}$ Å (corresponding to $\Delta E = 3.5 \cdot 10^{-7}$ eV) would result in a continuous initial beam of intensity $I_0 = 15 \cdot 10^4\ n/cm^2s$. The usable solid angle can only be a fair fraction of the solid angle from the neutron guide. Here we took $\pm 1.5°$ in both dimensions (certainly an upper estimate of what can be used), corresponding to a solid angle of $2.7 \cdot 10^{-3}$ sterad. The energy width ΔE corresponds (Heisenberg) to a time opening of the chopper of $\Delta t_c = 2 \cdot 10^{-9}$ s. The pulse intensity is $I_p = 3 \cdot 10^{-4}\ n/cm^2\,s$. If we assume a separation in time $t_s \approx 80\ \mu s$ of the pulses at the detector due to the magnetic splitting of the resonance flipper, the chopper may open about 1000 times per second in order to separate individual splittings. With 1 cm^2 of beam area the counting rate will be $Z = 0.3\ n/s$. In reality, the counting rate is certainly down by another factor of 10 to 100 even under very optimistic conditions, which is barely sufficient to conduct the experiment in the former configuration.

We have mentioned in the introduction to this section that a Multi-MIEZE signal with its intensity distribution according to Eqs. (1.170)/(3.1) is able to provide such pulses. The complete setup to demonstrate the longitudinal Stern-Gerlach effect would consist in a Multi-MIEZE with an additional strong resonance flipper directly behind it, acting as a splitter in time for spin-up and spin-down.

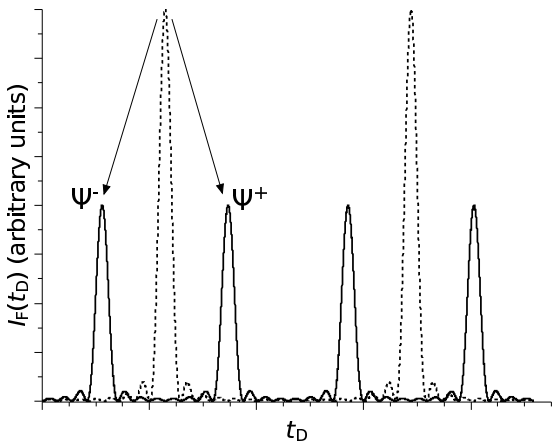

Figure 4.1: Calculated intensity distribution at the detector according to Eqs. (4.7)/(4.8), demonstrating the longitudinal Stern-Gerlach effect. The dashed line represents the initial four-level Multi-MIEZE signal.

Describing the splitting flipper as a scatterer with a scattering function $S(\omega)$, the intensity at the detector changes to $I_F(t_D) = \int I(t_D + \Delta t_D)S(\omega)d\omega$. For a flipper coil $S(\omega)$ has the shape of a delta function, $S(\omega) = 1/2[\delta(\omega - \omega_L) + \delta(\omega + \omega_L)]$. Therefore, the intensity pattern at the detector will appear as

$$\begin{aligned} I_F(t_D) &= \frac{1}{2}\int I(t_D + \frac{\hbar\omega_L L_s}{mv^3})[\delta(\omega - \omega_L) + \delta(\omega + \omega_L)]d\omega \\ &= \frac{I_0}{2}\left[T(t_D + \frac{\hbar\omega_L L_s}{mv^3}) + T(t_D - \frac{\hbar\omega_L L_s}{mv^3})\right], \end{aligned} \tag{4.8}$$

with T being the transmission function from Eqs. (1.166)/(1.170). Fig. 4.1 shows the resulting calculated signal in comparison to the initial four-level Multi-MIEZE signal.

As a configuration example we will assume four levels with a total distance between the first coil C_{A1} and the detector of $L_D = 8$ m. We choose $\omega_{A1} = 0.5$ MHz as the frequency of the first coil. The separations $L_{1\nu}$ between coils A and B of the respective stages may be $L_{11} = 1$ m, $L_{12} = 0.7$ m, $L_{13} = 0.5$ m, and $L_{14} = 0.3$ m. Furthermore, we leave a space of 0.3 m between each coil pair for the analyzers. Due to the geometric defaults the last coil C_{B4} runs at a frequency of 9.3 MHz. This would result in a signal with the main peaks being separated by $\Delta t_D \approx 13$ µs and having a width of $\delta t_p \approx 380$ ns (FWHM).
We now place the additional NRSE flipper after the endmost analyzer, with the DC field of the flipper pointing perpendicularly to the orientation of the analyzer. In this configuration it will

be located $L_s = 4.3$ m upstream the detector. This will shift the spin-up and spin-down states (with respect to the x-direction) and we should see a splitting of the sinusoidal pulses at the detector position. A static flipper field of $B_z = 0.1$ T will in first order lead to a pulse separation of $t_s = 2\hbar\omega_L L_s/mv^3 = 4.3$ μs. The time of arrival t_D is now changed by $\Delta t_D = t_s/2$ for either spin state.

The experimental configuration suggested above makes high demands on the technical implementation but seems possible. To relax the prerequisites for the coil frequencies and fields, the instrument could be stretched, with a long detector distance. A place where such an experiment could be realized is the nn̄ beamline at the Institut Laue-Langevin (ILL) with a total length of about 80 m. However, when enlarging the flight paths considerably, the loss in intensity must be taken into account, which will occur due to the divergence of the beam.

4.1.2 An Interferometer in Time and Space

In [15] Felber et al. proposed the possibility to build a Mach-Zehnder-like interferometer in time and space using the MIEZE technique. An interferometer of this type would require a macroscopic spatial splitting of the two spin states also in the lateral direction with respect to the incoming beam.

The splitting in momentum of the spin-up and spin-down states in the field region is $k_\pm \approx k_0 \pm \frac{m}{\hbar}\omega_z/v_0$ (cp. Eq. (1.139)) and does always happen in the direction perpendicular to the field boundaries [34]. Therefore, to achieve a splitting of the k-vector component of the wave packets that is perpendicular to the intial direction defined by $\boldsymbol{k}_0$, the field boundaries of the resonance flipper coils must be tilted with respect to the beam axis (the same applies to the detector plane). Fig. 4.2 illustrates that situation. The magnitude of the lateral splitting depends on the tilting angle ϑ of the coils, the neutron wavelength, and the exchanged quanta in the field ($\hbar\omega_z$), i.e. on the field intensities and frequencies.

The two separated partial matter waves, as indicated in Fig. 4.2, would therefore undergo a separation in time and space and could then be manipulated in different flight paths like it is possible in the two arms of a Mach-Zehnder interferometer.

According to [15], this could be realized on a very cold beamline ($\lambda_0 \approx 100$ Å), however, the NRSE coil technology would yet have to be enhanced to meet the required precision and field intensities.

On a side note, the k-splitting achieved by tilted coils as described above is the basis for the

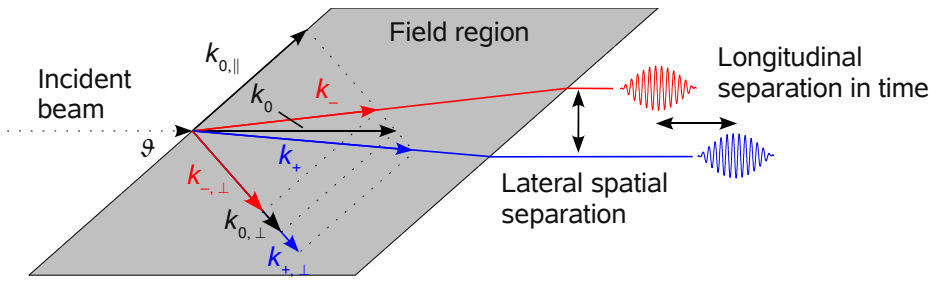

Figure 4.2: Lateral k-splitting of the spin-up and spin-down state in a magnetic field with inclined boundaries.

phonon-focusing technique in N(R)SE that allows for the measurement of dispersive excitations (where the energy transfer $\omega = \omega(q)$ depends on the scattering vector) with spin echo. By inclining the field boundaries, the spin echo phase, which is normally independent of the wavelength distribution, is given the necessary q-dependence [4, 34]. This allows for the resolution of e.g. phonon peak widths by combining the high energy resolution of N(R)SE with a triple axis spectrometer.

4.2 MIEZE in Neutron Science Instrumentation

We like to view MIEZE not as a replacement, but as an addition to the existing well-established spin echo techniques, and in some way as a complementary option. The examples following below shall demonstrate its uses and potential. Another side-effect of the working principle worth mentioning is the fact that since the MIEZE instrument uses only one NRSE arm (two coils and one shielding), the costs are lower compared to NRSE. Also the possibility to build a MIEZE setup in a compact way requiring little space makes it attractive for inclusion as an add-on for existing instruments. MIRA is a good example in this respect.

4.2.1 Non-trivial Sample Environments

In section 3.5 we have demonstrated that spin echo-like quasi-elastic measurements with MIEZE are possible also for samples and sample environments that impose considerable efforts for conventional spin echo or NRSE instruments.

The fact that the signal modulation is prepared at the analyzer means that downstream the signal is insensitive to depolarization. As a consequence the normally required zero-field shielding at the sample region can be omitted. This provides the freedom to apply strong magnetic fields, mount instrumentation with possible electro-magnetic stray fields (like high or low temperatures devices), or measure ferromagnetic and antiferromagnetic samples.

Two examples for such measurements, which are planned for MIRA and/or RESEDA using the MIEZE option, are magnetic phase transitions and the motion of the vortex lattice in type-II superconductors under an external field.

An interesting system, falling under the category of the first example, is the weak itinerant ferromagnet Manganese Silicide (MnSi), which has a complex magnetic phase diagram. Work on the chiral magnetic structure of MnSi, using mostly polarized SANS techniques, has been done e.g. by [35, 36, 37]. The dynamics taking place at phase transitions in this system are little investigated and might be a field of interest where the MIEZE technique could provide adequate instrumental means.

In [38], NSE measurements have been performed on the vortex lattice motion in a Niob Tantalum alloy using the spin echo spectrometer IN15 at the ILL in the „ferromagnetic“ configuration [39]. Normally the flux lines in a type-II superconductor are pinned by disorders. When applying a sufficiently high external magnetic field, the Lorentz force (when exceeding the pinning force) will result in a vortex motion. Investigations of the dynamics can provide insight into e.g. pinning effects, the velocity distribution in the vortex lattice, and practically relevant properties like the critical current. The ferromagnetic spin echo method used in [38] requires a strong magnetic field at the sample region of the NSE spectrometer, resulting in a spin echo signal with a 50% reduced amplitude. In such a configuration MIEZE would in principle operate without loss of contrast.

As another consequence, samples containing elements with a high spin flip probability (like hydrogen) can be used. This makes MIEZE well suited for measurements on protonated samples, as opposed to conventional NSE, where deuterated samples are preferred. Due to the high scattering cross section of H, the samples can be prepared significantly thinner.

4.2.2 Multi-angle Scattering

When planning to equip other scattering techniques with a MIEZE option to obtain the possibility of additional high energy resolution, the effect of an extended sample must be taken into account: at high scattering angles ϑ and momentum transfers $\boldsymbol{q} = \boldsymbol{k}_2 - \boldsymbol{k}_1$, the different path lengths will lead to a decrease in contrast of the MIEZE signal even for elastic scattering. Fig. 4.3 demonstrates the situation for scattering at two different positions separated by $\boldsymbol{r}$. A quantitative estimation can be found in [4].

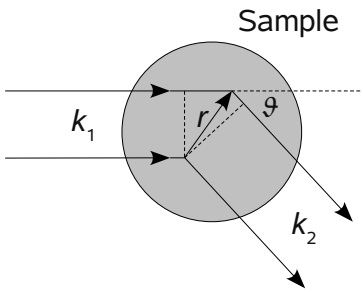

Figure 4.3: For extended samples and high scattering angles ϑ and momentum transfers $\boldsymbol{q} = \boldsymbol{k}_2 - \boldsymbol{k}_1$, the different path lengths lead to a decrease in contrast. For SANS applications (see below) they are usually negligible.

The MIEZE-2 instrument type is a MIEZE variant that uses a third resonance spin flipper (for details see [4] or [29]). To avoid the contrast losses we just described that will happen due to different path lengths in the sample, the necessary polarization modulation is here created after the sample region, where the additional flipper is placed (s. Fig. 4.4).

This instrument principle can be used to realize a scattering geometry that allows for measuring at multiple scattering angles simultaneously by shaping the third coil as a curve and using a multi-detector to cover large angular and q ranges. The setup is shown in Fig. 4.4. For the sample region of a MIEZE-2 instrument the same restrictions apply as for NRSE. An example of a realized NRSE multi-detector setup can by found in [40].

A multi-angle scattering option is planned for the instrument RESEDA at the neutron source FRM-II [41] and a respective curved coil as sketched in Fig. 4.4 is currently under development.

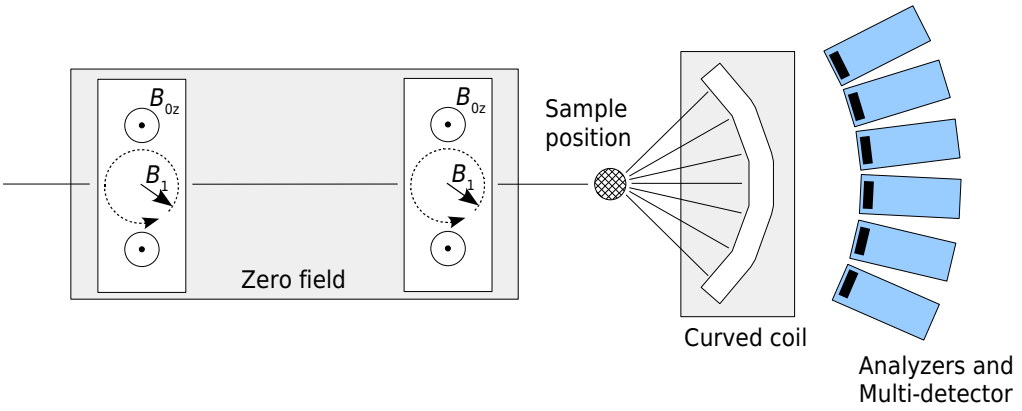

Figure 4.4: Multi-angle scattering geometry using the MIEZE-2 variant (top view).

4.2.3 Long Beam Geometries – High Energy Resolution for SANS (Small Angle Neutron Scattering)

The SANS technique investigates the scattering into very small angles to obtain information about the size, shape, and orientation of particles or components in a sample. By integrating a MIEZE setup into the beam line, the possibility of additional high energy resolution analysis could be obtained. The prerequisites for the detector are a time resolution in the μs range and a 2D spatial resolution.

Due to the coupling of RF frequencies and distances in the MIEZE technique, the instrument configuration can be altered according to the needs. This means that the frequencies can be tuned to match given distances, we have already elaborated on this in section 3.5.

To resolve very small scattering angles, a SANS instrument requires a long sample-detector distance, which means that the frequency difference of the coils of the MIEZE part will be relatively small. Fig. 4.5 shows the principle setup.

The contrast reduction caused by geometry effects as described above in section 4.2.2 is usually negligible here, because only small q transfers are investigated.

The MISANS project in Argonne [42, 43], although still in the testing phase, aims to build a dedicated SANS/MIEZE instrument for the SNS spallation source. However, according to our knowledge the extension of existing SANS machines with MIEZE was seldomly considered.

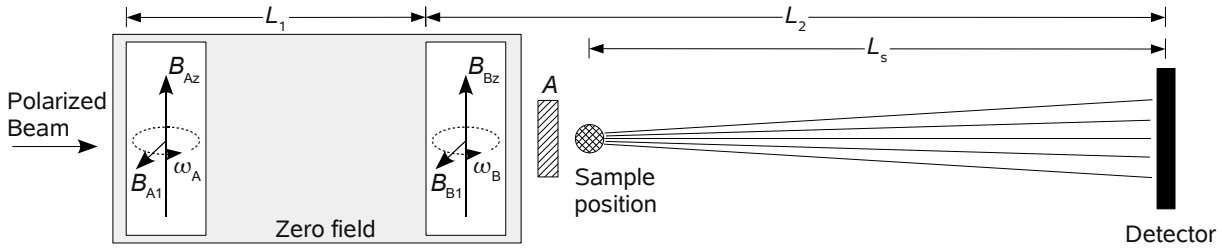

Figure 4.5: MIEZE add-on for a SANS instrument. The detector distance is large and in addition to a time-resolution in the μs range, the detector must provide 2D spatial resolution.

4.2.4 Bunching of Continuous Neutron Beams – Time-modulation of Neutron Beams

In a recent publication [44] Golub et al. proposed the so-called bunching of continuous polychromatic neutron beams, a concept similar to that described above for measuring the longitudinal Stern-Gerlach effect. The technique is based on a MIEZE instrument plus the buncher, which replaces the polarization analyzer. The buncher is another high-power resonance flipper with a B_0 field orientation orthogonal to that of the MIEZE resonance flipper coils. It has relaxed prerequisites with respect to sharp field boundaries and the RF is not phase-locked with the other coils but free-running. Fig. 4.6 shows the principle setup.

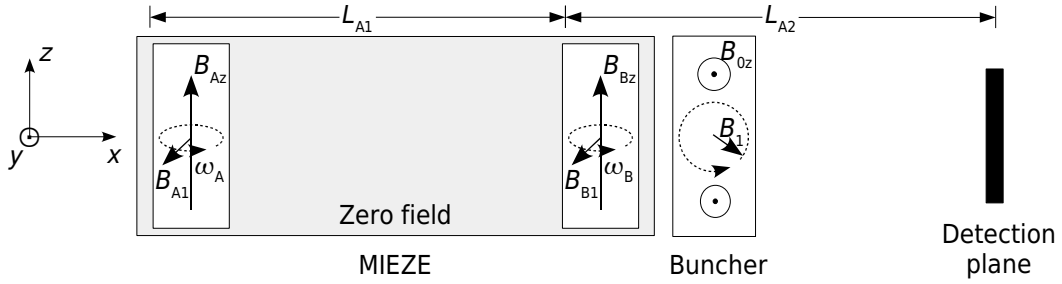

Figure 4.6: Setup of a MIEZE with integrated buncher (side view).

The idea is to not let the analyzer eliminate one spin direction, as it is in the case of MIEZE, where the intensity corresponding to one of the spin states is absorbed. The buncher introduces a new quantization axis (in our notation the y-direction) and hence induces an additional splitting, i.e. a phase shift, of spin-up and spin-down. That alters the velocities of the states in such a way that the intensity modulation at the detector can be achieved by shifting the partial intensities and letting them superpose at the detection plane. This becomes clearer when looking at the diagram for the total energy of the spin states in Fig. 4.7.

In second order the k-vector splitting is not symmetric and the partial waves have therefore slightly different MIEZE conditions, i.e. different velocity focusing positions. The detector is

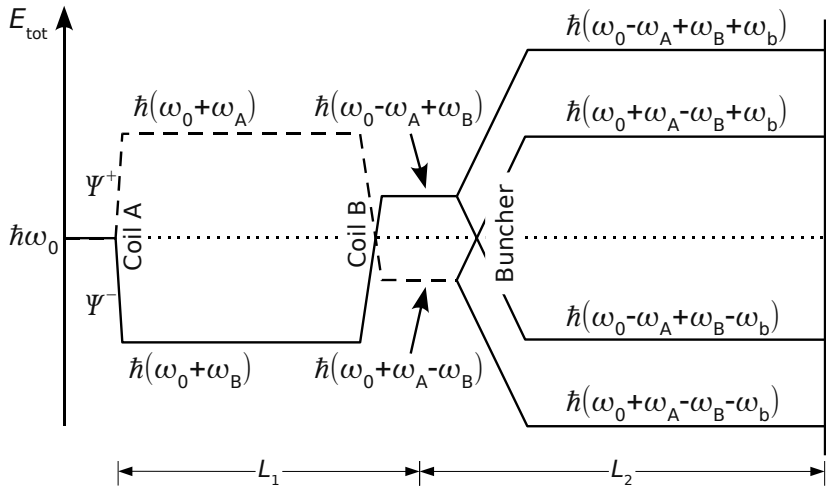

Figure 4.7: Energy diagram for MIEZE with the buncher replacing the analyzer.

placed in between these two positions and the intensity for the MIEZE/buncher system is almost doubled at the detection plane compared to conventional MIEZE. For more details we refer to [44].

This setup can be used like MIEZE as a stand-alone spectrometer, but would also allow for improvements of other instruments in neutron science. It could be included into the beam lines at neutron sources and provide an unsurpassed time-modulation of the beam. To give an impression, possible areas of usage include [45]

- Increase of energy resolution in Time-of-flight (TOF) spectrometry
- Measuring inelastic effects in TOF-diffraction
- Background reduction in Triple axis (TAS) multi angle scattering analysis
- Lock-in techniques for neutron scattering ('stroboscopic' illumination of the sample with the MIEZE modulation frequency)
- Measurement of decay time in neutron-induced reactions (in-beam irradiation by an intensity-modulated signal)
- Small Angle Neutron Scattering (SANS) with high resolution energy analysis

5

Summary and Outlook

In this work we have investigated the MIEZE and Multi-MIEZE techniques both theoretically and experimentally. The quantum mechanical formalism of time-evolution operators has been applied to polarization theory, as well as to resonance spin echo field configurations and, in particular, to the MIEZE instrument. The signal of the latter is a high-frequency, sinusoidal intensity modulation that is, from the quantum mechanical point of view, resulting from the beat of two partial waves (spin-up and spin-down) with different k and ω. In our treatment we consider this splitting in energy and momentum of the spin-up and spin-down states more consistently, which results in a slight dependence of the detector position (determined by the MIEZE condition) from the neutron energy, which does not show in previous classical descriptions.

The Multi-MIEZE principle, predicting that the intensity pattern of subsequently stacked MIEZE setups is resulting from the product of the time-dependent transmission probabilities of each individual stage, has been verified. The intensity distribution function of the expected signal has been fitted and matches the data very well. We proposed the definition of a contrast-like quantity in order to describe the quality of a Multi-MIEZE signal in analogy to the contrast or polarization of a single MIEZE or NRSE instrument, respectively. With a properly tuned two-level Multi-MIEZE setup the sharpening of the main peaks in the high-frequency signal could be observed. The signal of a Multi-MIEZE instrument resembles that of a very fast chopper, which opens the possibilities of TOF measurements with very high resolution, or experiments in interferometry and fundamental physics.

Furthermore, a complete set of NRSE and MIEZE instrumentation has been built and installed at the very cold beam line of the instrument MIRA. Resonance flipper coils have been conceptualized using a new design approach, built and taken into operation. Other components like the RF coils were improved compared to existing designs.

First MIEZE measurements were conducted at MIRA with strong magnetic fields at the sample region, which demonstrated the potential of this technique in terms of the flexibility it provides in realizing various sample environments or long scattering geometries without significant loss of polarization. Drawbacks are arising from the requirements for the detector, which must have a high time resolution and a very well defined detection plane. This decreases the efficiency compared to detector systems with a large detection volume. This deficiency could be reduced significantly once the CASCADE detector is technologically fully developed.

All measurements were performed at MIRA and the instrumentation was built specifically for this instrument. Although MIRA is not a dedicated resonance spin echo spectrometer, it is a flexible instrument and as such has the opportunity to combine different scattering techniques for interesting measurements (e.g. the combination of MIEZE with SANS or reflectivity). In

Shielding	Enhancement of the zero-field shielding factor by a double-layer Mu-metal shielding.
Coils	Installation of magnetic shielding cases for the resonance flipper coils to reduce stray fields. See [29] and [21] for calculations on Mu-metal shieldings and design optimizations. Improving the manufacturing techniques (welding, neutron beam window cutting) for the B_0 coils, thus enhancing the mechanical precision and lowering depolarization. In order to be able to equalize the B_0 fields in all coils (even if they are fed by the same power supply), each one should be equipped with a resistor system allowing for precise current tuning. Installation of compensation conductor stripes to eliminate the resulting (but unwanted) z-component of the DC current.
Cooling System	Implemention of a water cooling system in addition to air cooling.
Sample environment	Design of a proper zero-field sample environment for the NRSE option.
Electronics	Enhancements in device control and instrument tuning automatization.
Detector system	Detector system upgrade, including an easy-to-mount and precise positioning system with large scan ranges. The CASCADE detector appears to be an appropriate choice for MIEZE applications (including 2D resolution).

Table 5.1: Suggested improvements and additions for the MIRA instrument with regard to the MIEZE and NRSE options.

order to improve the NRSE and MIEZE options at MIRA and bring them to a level allowing permanent user operation, we would like to propose possible improvements and additions for the near future, which are listed in Table 5.1.

In chapter 4 we presented some of the possible areas of application for MIEZE and Multi-MIEZE, which amongst others include fundamental physics experiments, the addition of high energy resolution on SANS machines (a current project is covered in [42, 43]), or the possibility of obtaining an unsurpassed time-modulation of the beam at the detector position by integration in beam lines at neutron sources. The opportunities of MIEZE have been pointed out before (e.g. [4, 6, 5] and references therein), but the further development and the usage of this technique, also in conjuction with other scattering methods, evolved only slowly since the years of its invention. We hope that this situation may change and the results of this work can make a contribution.

Appendix

A.1 Polarization Theory

Density matrix for the field configuration of an NRSE flipper coil (general case, cp. section 1.1.4.1):

$$\varrho(t) = U(t,0)\,\varrho(0)\,U^{\dagger}(t,0) = \frac{1}{2}\times$$

$$\begin{pmatrix}
1 + P_{0x}\dfrac{\gamma B_1}{\omega_R}\Big[\sin\omega_R t\sin\varphi + \dfrac{r}{\omega_R}(1-\cos\omega_R t)\cos\varphi\Big] + \\
1 + P_{0y}\dfrac{\gamma B_1}{\omega_R}\Big[\sin\omega_R t\cos\varphi - \dfrac{r}{\omega_R}(1-\cos\omega_R t)\sin\varphi\Big] + \\
1 + P_{0z}\Big[1 - \left(\dfrac{\gamma B_1}{\omega_R}\right)^2(1-\cos\omega_R t)\Big]
& P_{0x}\,e^{-i\omega t}\Big[\left(\dfrac{\gamma B_1}{\omega_R}\right)^2 e^{i2\varphi}\sin^2\dfrac{\omega_R t}{2} + \left(\cos\dfrac{\omega_R t}{2} - i\dfrac{r}{\omega_R}\sin\dfrac{\omega_R t}{2}\right)^2\Big] + \\
& iP_{0y}\,e^{-i\omega t}\Big[\left(\dfrac{\gamma B_1}{\omega_R}\right)^2 e^{i2\varphi}\sin^2\dfrac{\omega_R t}{2} - \left(\cos\dfrac{\omega_R t}{2} - i\dfrac{r}{\omega_R}\sin\dfrac{\omega_R t}{2}\right)^2\Big] + \\
& P_{0z}\dfrac{\gamma B_1}{\omega_R}\,e^{i\varphi}e^{-i\omega t}\Big[i\sin\omega_R t + \dfrac{r}{\omega_R}(1-\cos\omega_R t)\Big] \\
P_{0x}\,e^{i\omega t}\Big[\left(\dfrac{\gamma B_1}{\omega_R}\right)^2 e^{-i2\varphi}\sin^2\dfrac{\omega_R t}{2} + \left(\cos\dfrac{\omega_R t}{2} + i\dfrac{r}{\omega_R}\sin\dfrac{\omega_R t}{2}\right)^2\Big] - \\
iP_{0y}\,e^{i\omega t}\Big[\left(\dfrac{\gamma B_1}{\omega_R}\right)^2 e^{-i2\varphi}\sin^2\dfrac{\omega_R t}{2} - \left(\cos\dfrac{\omega_R t}{2} + i\dfrac{r}{\omega_R}\sin\dfrac{\omega_R t}{2}\right)^2\Big] - \\
P_{0z}\dfrac{\gamma B_1}{\omega_R}\,e^{-i\varphi}e^{i\omega t}\Big[i\sin\omega_R t - \dfrac{r}{\omega_R}(1-\cos\omega_R t)\Big]
& 1 - P_{0x}\dfrac{\gamma B_1}{\omega_R}\Big[\sin\omega_R t\sin\varphi + \dfrac{r}{\omega_R}(1-\cos\omega_R t)\cos\varphi\Big] + \\
& 1 - P_{0y}\dfrac{\gamma B_1}{\omega_R}\Big[\sin\omega_R t\cos\varphi - \dfrac{r}{\omega_R}(1-\cos\omega_R t)\sin\varphi\Big] + \\
& 1 - P_{0z}\Big[1 - \left(\dfrac{\gamma B_1}{\omega_R}\right)^2(1-\cos\omega_R t)\Big]
\end{pmatrix} \tag{A.1}$$

Density matrix for a spatially rotating field (cp. section 1.1.4.2):

$$\varrho_{\mathrm{B}_1}(t) = \begin{pmatrix} 1 - P_{0x}\frac{\gamma B_1}{\omega_R}\frac{\omega_{cc}}{\omega_R}(1-\cos\omega_R t) + \\ 1 + P_{0y}\frac{\gamma B_1}{\omega_R}\sin\omega_R t + \\ 1 + P_{0z}\left[1 - \left(\frac{\gamma B_1}{\omega_R}\right)^2 (1-\cos\omega_R t)\right] \end{pmatrix} \quad \begin{pmatrix} P_{0x}\,\mathrm{e}^{-i\omega_{cc}t}\left[\left(\frac{\gamma B_1}{\omega_R}\right)^2 \sin^2\frac{\omega_R t}{2} + \left(\cos\frac{\omega_R t}{2} + i\frac{\omega_{cc}}{\omega_R}\sin\frac{\omega_R t}{2}\right)^2\right] + \\ iP_{0y}\,\mathrm{e}^{-i\omega_{cc}t}\left[\left(\frac{\gamma B_1}{\omega_R}\right)^2 \sin^2\frac{\omega_R t}{2} - \left(\cos\frac{\omega_R t}{2} + i\frac{\omega_{cc}}{\omega_R}\sin\frac{\omega_R t}{2}\right)^2\right] + \\ P_{0z}\frac{\gamma B_1}{\omega_R}\,\mathrm{e}^{-i\omega_{cc}t}\left[i\sin\omega_R t - \frac{\omega_{cc}}{\omega_R}(1-\cos\omega_R t)\right] \end{pmatrix}$$

$$\begin{pmatrix} P_{0x}\,\mathrm{e}^{i\omega_{cc}t}\left[\left(\frac{\gamma B_1}{\omega_R}\right)^2 \sin^2\frac{\omega_R t}{2} + \left(\cos\frac{\omega_R t}{2} - i\frac{\omega_{cc}}{\omega_R}\sin\frac{\omega_R t}{2}\right)^2\right] - \\ iP_{0y}\,\mathrm{e}^{i\omega_{cc}t}\left[\left(\frac{\gamma B_1}{\omega_R}\right)^2 \sin^2\frac{\omega_R t}{2} - \left(\cos\frac{\omega_R t}{2} - i\frac{\omega_{cc}}{\omega_R}\sin\frac{\omega_R t}{2}\right)^2\right] - \\ P_{0z}\frac{\gamma B_1}{\omega_R}\,\mathrm{e}^{i\omega_{cc}t}\left[i\sin\omega_R t + \frac{\omega_{cc}}{\omega_R}(1-\cos\omega_R t)\right] \end{pmatrix} \quad \begin{pmatrix} 1 + P_{0x}\frac{\gamma B_1}{\omega_R}\frac{\omega_{cc}}{\omega_R}(1-\cos\omega_R t) + \\ 1 - P_{0y}\frac{\gamma B_1}{\omega_R}\sin\omega_R t + \\ 1 - P_{0z}\left[1 - \left(\frac{\gamma B_1}{\omega_R}\right)^2 (1-\cos\omega_R t)\right] \end{pmatrix} \tag{A.2}$$

A.2 Mathematica™ Scripts

The following Mathematica™ notebook scripts were used for calculating the phase accumulation of the spin states in a MIEZE instrument and deriving the MIEZE conditions Eqs. (1.155) and (1.156). The expressions have to be evaluated in the correct order, indicated by the *In[ ]:=* and *Out[ ]=* markers. With the respective definition changes, the calculations for the spin-up state apply likewise to spin-down (the output of which is not listed here).

Times (with respect to the arrival time at the detector, expressed by distances and different velocities)

```
In[29]:= t0Up = tDUp - (DC / v1Up + (L1 - DC) / v12Up + DC / v2Up + (L2 - DC) / vDUp)
         t0Down = tDDown - (DC / v1Down + (L1 - DC) / v12Down + DC / v2Down + (L2 - DC) / vDDown)
```

$$\text{Out[29]=}\quad \text{tDUp} - \frac{-\text{DC} + \text{L1}}{\text{v12Up}} - \frac{\text{DC}}{\text{v1Up}} - \frac{\text{DC}}{\text{v2Up}} - \frac{-\text{DC} + \text{L2}}{\text{vDUp}}$$

$$\text{Out[30]=}\quad \text{tDDown} - \frac{-\text{DC} + \text{L1}}{\text{v12Down}} - \frac{\text{DC}}{\text{v1Down}} - \frac{\text{DC}}{\text{v2Down}} - \frac{-\text{DC} + \text{L2}}{\text{vDDown}}$$

```
In[31]:= t1Up = t0Up + DC / v1Up
         t1Down = t0Down + DC / v1Down
```

$$\text{Out[31]=}\quad \text{tDUp} - \frac{-\text{DC} + \text{L1}}{\text{v12Up}} - \frac{\text{DC}}{\text{v2Up}} - \frac{-\text{DC} + \text{L2}}{\text{vDUp}}$$

$$\text{Out[32]=}\quad \text{tDDown} - \frac{-\text{DC} + \text{L1}}{\text{v12Down}} - \frac{\text{DC}}{\text{v2Down}} - \frac{-\text{DC} + \text{L2}}{\text{vDDown}}$$

```
In[33]:= t12Up = t1Up + (L1 - DC) / v12Up
         t12Down = t1Down + (L1 - DC) / v12Down
```

$$\text{Out[33]=}\quad \text{tDUp} - \frac{\text{DC}}{\text{v2Up}} - \frac{-\text{DC} + \text{L2}}{\text{vDUp}}$$

$$\text{Out[34]=}\quad \text{tDDown} - \frac{\text{DC}}{\text{v2Down}} - \frac{-\text{DC} + \text{L2}}{\text{vDDown}}$$

```
In[35]:= t2Up = t12Up + DC / v2Up
         t2Down = t12Down + DC / v2Down
```

$$\text{Out[35]=}\quad \text{tDUp} - \frac{-\text{DC} + \text{L2}}{\text{vDUp}}$$

$$\text{Out[36]=}\quad \text{tDDown} - \frac{-\text{DC} + \text{L2}}{\text{vDDown}}$$

Velocities (exact and square root approximation)

```
v1Up = Sqrt[1 + (omegaA / 2) / omega0] * v0
v1Down = Sqrt[1 + (-omegaA / 2) / omega0] * v0

v1Up = (1 + (omegaA / 2) / omega0 / 2) * v0
v1Down = (1 + (-omegaA / 2) / omega0 / 2) * v0
```

$$\left(1 + \frac{\text{omegaA}}{4\ \text{omega0}}\right)\ \text{v0}$$

$$\left(1 - \frac{\text{omegaA}}{4\ \text{omega0}}\right)\ \text{v0}$$

```
v12Up = Sqrt[1 + omegaA / omega0] * v0
v12Down = Sqrt[1 + (-omegaA) / omega0] * v0

v12Up = (1 + omegaA / omega0 / 2) * v0
v12Down = (1 + (-omegaA) / omega0 / 2) * v0
```

$$\left(1 + \frac{\text{omegaA}}{2\ \text{omega0}}\right)\ \text{v0}$$

$$\left(1 - \frac{\text{omegaA}}{2\ \text{omega0}}\right)\ \text{v0}$$

```
v2Up = Sqrt[1 + (omegaA - omegaB / 2) / omega0] * v0
v2Down = Sqrt[1 + (-omegaA + omegaB / 2) / omega0] * v0
```

```
v2Up = (1 + (omegaA - omegaB / 2) / omega0 / 2) * v0
v2Down = (1 + (-omegaA + omegaB / 2) / omega0 / 2) * v0
```

$$\left(1 + \frac{\text{omegaA} - \frac{\text{omegaB}}{2}}{2\ \text{omega0}}\right)\ \text{v0}$$

$$\left(1 + \frac{-\text{omegaA} + \frac{\text{omegaB}}{2}}{2\ \text{omega0}}\right)\ \text{v0}$$

```
vDUp = Sqrt[1 + (omegaA - omegaB) / omega0] * v0
vDDown = Sqrt[1 + (-omegaA + omegaB) / omega0] * v0
```

```
vDUp = (1 + (omegaA - omegaB) / omega0 / 2) * v0
vDDown = (1 + (-omegaA + omegaB) / omega0 / 2) * v0
```

$$\left(1 + \frac{\text{omegaA} - \text{omegaB}}{2\ \text{omega0}}\right)\ \text{v0}$$

$$\left(1 + \frac{-\text{omegaA} + \text{omegaB}}{2\ \text{omega0}}\right)\ \text{v0}$$

Energies

```
omega1Up = omega0 + omegaA
omega1Down = omega0 - omegaA
```

omega0 + omegaA

omega0 - omegaA

```
omega12Up = omega0 + omegaA
omega12Down = omega0 - omegaA
```

omega0 + omegaA

omega0 - omegaA

```
omega2Up = omega0 + omegaA - omegaB
omega2Down = omega0 - omegaA + omegaB
```

omega0 + omegaA - omegaB

omega0 - omegaA + omegaB

```
omegaDUp = omega0 + omegaA - omegaB
omegaDDown = omega0 - omegaA + omegaB
```

omega0 + omegaA - omegaB

omega0 - omegaA + omegaB

RF phases

```
In[1]:= phiAUp = -omegaA t0Up
        phiADown = -omegaA t0Down
```

```
Out[1]= -omegaA t0Up
```

```
Out[2]= -omegaA t0Down
```

```
In[5]:= phiBUp = -omegaB t12Up
        phiBDown = -omegaB t12Down
Out[5]= -omegaB t12Up
Out[6]= -omegaB t12Down
```

Initial spinor (here: only spin−up)

```
In[7]:= Psi0 = {Psi0Up, 0}
Out[7]= {Psi0Up, 0}
```

Pi−flip condition first coil

```
In[9]:= omega1A = Pi / (t1Up - t0Up)
```

$$\text{Out[9]}= \frac{\pi}{-\text{t0Up}+\text{t1Up}}$$

Time−evolution operator for and spin state after the first coil

```
In[10]:= U1F = {{1, 0}, {0, 1}}
Out[10]= {{1, 0}, {0, 1}}
```

```
In[12]:= U1R = {{Cos[omega1A / 2 * (t1Up - t0Up)] * Exp[-I * omegaA / 2 * (t1Up - t0Up)],
             -I * Sin[omega1A / 2 * (t1Down - t0Down)] * Exp[-I * omegaA / 2 * (t1Down - t0Down)] *
              Exp[I * phiADown]}, {-I * Sin[omega1A / 2 * (t1Up - t0Up)] *
              Exp[I * omegaA / 2 * (t1Up - t0Up)] * Exp[-I * phiAUp],
             Cos[omega1A / 2 * (t1Down - t0Down)] * Exp[I * omegaA / 2 * (t1Down - t0Down)]]}
```

$$\text{Out[12]}= \left\{\left\{0,\ -i\, e^{-i\,\text{omegaA}\,\text{t0Down}-\frac{1}{2}i\,\text{omegaA}\,(-\text{t0Down}+\text{t1Down})}\,\text{Sin}\left[\frac{\pi\,(-\text{t0Down}+\text{t1Down})}{2\,(-\text{t0Up}+\text{t1Up})}\right]\right\},\right.$$
$$\left.\left\{-i\, e^{i\,\text{omegaA}\,\text{t0Up}+\frac{1}{2}i\,\text{omegaA}\,(-\text{t0Up}+\text{t1Up})},\ e^{\frac{1}{2}i\,\text{omegaA}\,(-\text{t0Down}+\text{t1Down})}\,\text{Cos}\left[\frac{\pi\,(-\text{t0Down}+\text{t1Down})}{2\,(-\text{t0Up}+\text{t1Up})}\right]\right\}\right\}$$

```
In[13]:= U1 = U1F.U1R
```

$$\text{Out[13]}= \left\{\left\{0,\ -i\, e^{-i\,\text{omegaA}\,\text{t0Down}-\frac{1}{2}i\,\text{omegaA}\,(-\text{t0Down}+\text{t1Down})}\,\text{Sin}\left[\frac{\pi\,(-\text{t0Down}+\text{t1Down})}{2\,(-\text{t0Up}+\text{t1Up})}\right]\right\},\right.$$
$$\left.\left\{-i\, e^{i\,\text{omegaA}\,\text{t0Up}+\frac{1}{2}i\,\text{omegaA}\,(-\text{t0Up}+\text{t1Up})},\ e^{\frac{1}{2}i\,\text{omegaA}\,(-\text{t0Down}+\text{t1Down})}\,\text{Cos}\left[\frac{\pi\,(-\text{t0Down}+\text{t1Down})}{2\,(-\text{t0Up}+\text{t1Up})}\right]\right\}\right\}$$

```
In[14]:= Psi1 = FullSimplify[U1.Psi0]
```

$$\text{Out[14]}= \left\{0,\ -i\, e^{\frac{1}{2}i\,\text{omegaA}\,(\text{t0Up}+\text{t1Up})}\,\text{Psi0Up}\right\}$$

Before second coil

```
In[15]:= U12 = {{1, 0}, {0, 1}}
Out[15]= {{1, 0}, {0, 1}}
```

```
In[16]:= Psi12 = FullSimplify[U12.Psi1]

Out[16]= {0, -i e^(1/2 i omegaA (t0Up+t1Up)) Psi0Up}
```

Pi−flip condition second coil

```
In[18]:= omega1B = Pi / (t2Up - t12Up)

Out[18]= Pi / (-t12Up + t2Up)
```

Time−evolution operator for and spin state after the second coil

```
In[19]:= U2F = {{1, 0}, {0, 1}}

Out[19]= {{1, 0}, {0, 1}}

In[21]:= U2R = {{Cos[omega1B / 2 * (t2Down - t12Down)] * Exp[-I * omegaB / 2 * (t2Down - t12Down)],
     -I * Sin[omega1B / 2 * (t2Up - t12Up)] * Exp[-I * omegaB / 2 * (t2Up - t12Up)] *
      Exp[I * phiBUp]}, {-I * Sin[omega1B / 2 * (t2Down - t12Down)] *
      Exp[I * omegaB / 2 * (t2Down - t12Down)] * Exp[-I * phiBDown],
     Cos[omega1B / 2 * (t2Up - t12Up)] * Exp[I * omegaB / 2 * (t2Up - t12Up)]]}

Out[21]= {{e^(-1/2 i omegaB (-t12Down+t2Down)) Cos[Pi (-t12Down + t2Down) / (2 (-t12Up + t2Up))],
    -i e^(-i omegaB t12Up - 1/2 i omegaB (-t12Up+t2Up))},
   {-i e^(i omegaB t12Down + 1/2 i omegaB (-t12Down+t2Down)) Sin[Pi (-t12Down + t2Down) / (2 (-t12Up + t2Up))], 0}}

In[22]:= U2 = U2F.U2R

Out[22]= {{e^(-1/2 i omegaB (-t12Down+t2Down)) Cos[Pi (-t12Down + t2Down) / (2 (-t12Up + t2Up))],
    -i e^(-i omegaB t12Up - 1/2 i omegaB (-t12Up+t2Up))},
   {-i e^(i omegaB t12Down + 1/2 i omegaB (-t12Down+t2Down)) Sin[Pi (-t12Down + t2Down) / (2 (-t12Up + t2Up))], 0}}

In[24]:= Psi2 = FullSimplify[U2.Psi12]

Out[24]= {-e^(1/2 i (omegaA (t0Up+t1Up)-omegaB (t12Up+t2Up))) Psi0Up, 0}
```

At the detector

```
In[25]:= UD = {{1, 0}, {0, 1}}

Out[25]= {{1, 0}, {0, 1}}

In[26]:= PsiD = FullSimplify[UD.Psi2]

Out[26]= {-e^(1/2 i (omegaA (t0Up+t1Up)-omegaB (t12Up+t2Up))) Psi0Up, 0}
```

Times replaced by distances/velocities

```
In[37]:= PsiD = FullSimplify[PsiD]

Out[37]= {-E^(1/2 I (omegaA (2 tDUp + (2 (DC - L1))/v12Up - DC/v1Up - (2 DC)/v2Up + (2 (DC - L2))/vDUp) - omegaB (2 tDUp - DC/v2Up + (2 (DC - L2))/vDUp))) Psi0Up, 0}
```

Accumulated phase of the spin−up state

$$\text{In[38]:=}\quad \texttt{FullSimplify}\left[\frac{1}{2}\left(\texttt{omegaA}\left(2\,\texttt{tDUp}+\frac{2\,(\texttt{DC}-\texttt{L1})}{\texttt{v12Up}}-\frac{\texttt{DC}}{\texttt{v1Up}}-\frac{2\,\texttt{DC}}{\texttt{v2Up}}+\frac{2\,(\texttt{DC}-\texttt{L2})}{\texttt{vDUp}}\right)-\texttt{omegaB}\left(2\,\texttt{tDUp}-\frac{\texttt{DC}}{\texttt{v2Up}}+\frac{2\,(\texttt{DC}-\texttt{L2})}{\texttt{vDUp}}\right)\right)\right]$$

$$\text{Out[38]=}\quad \frac{1}{2}\left(\texttt{omegaA}\left(2\,\texttt{tDUp}+\frac{2\,(\texttt{DC}-\texttt{L1})}{\texttt{v12Up}}-\frac{\texttt{DC}}{\texttt{v1Up}}-\frac{2\,\texttt{DC}}{\texttt{v2Up}}+\frac{2\,(\texttt{DC}-\texttt{L2})}{\texttt{vDUp}}\right)-\texttt{omegaB}\left(2\,\texttt{tDUp}-\frac{\texttt{DC}}{\texttt{v2Up}}+\frac{2\,(\texttt{DC}-\texttt{L2})}{\texttt{vDUp}}\right)\right)$$

Phase difference (results from spin−up/spin−down calculations)

$$\begin{aligned}\text{In[39]:=}\quad \texttt{Dphi} = \texttt{FullSimplify}\Bigg[&\frac{1}{2}\left(\texttt{omegaA}\left(2\,\texttt{tDUp}+\frac{2\,(\texttt{DC}-\texttt{L1})}{\texttt{v12Up}}-\frac{\texttt{DC}}{\texttt{v1Up}}-\frac{2\,\texttt{DC}}{\texttt{v2Up}}+\frac{2\,(\texttt{DC}-\texttt{L2})}{\texttt{vDUp}}\right)-\texttt{omegaB}\left(2\,\texttt{tDUp}-\frac{\texttt{DC}}{\texttt{v2Up}}+\frac{2\,(\texttt{DC}-\texttt{L2})}{\texttt{vDUp}}\right)\right)-\\&\left(-\frac{1}{2}\left(\texttt{omegaA}\left(2\,\texttt{tDDown}+\frac{2\,(\texttt{DC}-\texttt{L1})}{\texttt{v12Down}}-\frac{\texttt{DC}}{\texttt{v1Down}}-\frac{2\,\texttt{DC}}{\texttt{v2Down}}+\frac{2\,(\texttt{DC}-\texttt{L2})}{\texttt{vDDown}}\right)-\texttt{omegaB}\left(2\,\texttt{tDDown}-\frac{\texttt{DC}}{\texttt{v2Down}}+\frac{2\,(\texttt{DC}-\texttt{L2})}{\texttt{vDDown}}\right)\right)\right)\Bigg]\end{aligned}$$

$$\begin{aligned}\text{Out[39]=}\quad \frac{1}{2}\Bigg(&\texttt{omegaA}\left(2\,\texttt{tDDown}+2\,\texttt{tDUp}-\frac{2\,\texttt{L1}\,(\texttt{v12Down}+\texttt{v12Up})}{\texttt{v12Down}\,\texttt{v12Up}}+\right.\\&\left.\texttt{DC}\left(\frac{2}{\texttt{v12Down}}+\frac{2}{\texttt{v12Up}}-\frac{1}{\texttt{v1Down}}-\frac{1}{\texttt{v1Up}}+2\left(-\frac{1}{\texttt{v2Down}}-\frac{1}{\texttt{v2Up}}+\frac{1}{\texttt{vDDown}}+\frac{1}{\texttt{vDUp}}\right)\right)-\right.\\&\left.\frac{2\,\texttt{L2}\,(\texttt{vDDown}+\texttt{vDUp})}{\texttt{vDDown}\,\texttt{vDUp}}\right)+\texttt{omegaB}\\&\left(-2\,\texttt{tDDown}-2\,\texttt{tDUp}+\texttt{DC}\left(\frac{1}{\texttt{v2Down}}+\frac{1}{\texttt{v2Up}}-\frac{2}{\texttt{vDDown}}-\frac{2}{\texttt{vDUp}}\right)+\frac{2\,\texttt{L2}\,(\texttt{vDDown}+\texttt{vDUp})}{\texttt{vDDown}\,\texttt{vDUp}}\right)\Bigg)\end{aligned}$$

Time of arrival at the detector must be equal.

```
In[40]:= tDDown = tDUp = tD
```

$$\text{Out[40]= } tD$$

```
In[41]:= FullSimplify[Dphi]
```

$$\text{Out[41]= } \frac{1}{2}\left(\text{omegaA}\left(4\,tD-\frac{2\,L1\,(v12Down+v12Up)}{v12Down\,v12Up}+DC\left(\frac{2}{v12Down}+\frac{2}{v12Up}-\frac{1}{v1Down}-\frac{1}{v1Up}+2\left(-\frac{1}{v2Down}-\frac{1}{v2Up}+\frac{1}{vDDown}+\frac{1}{vDUp}\right)\right)-\frac{2\,L2\,(vDDown+vDUp)}{vDDown\,vDUp}\right)+\text{omegaB}\left(-4\,tD+DC\left(\frac{1}{v2Down}+\frac{1}{v2Up}-\frac{2}{vDDown}-\frac{2}{vDUp}\right)+\frac{2\,L2\,(vDDown+vDUp)}{vDDown\,vDUp}\right)\right)$$

Restructuring a bit ...

```
In[42]:= 2 (omegaA - omegaB) tD +
          1/2 (omegaA (-(2 L1 (v12Down + v12Up))/(v12Down v12Up) + DC (2/v12Down + 2/v12Up - 1/v1Down - 1/v1Up +
                2 (-1/v2Down - 1/v2Up + 1/vDDown + 1/vDUp)) - (2 L2 (vDDown + vDUp))/(vDDown vDUp)) +
            omegaB (DC (1/v2Down + 1/v2Up - 2/vDDown - 2/vDUp) + (2 L2 (vDDown + vDUp))/(vDDown vDUp)))
```

$$\text{Out[42]= } 2\,(\text{omegaA}-\text{omegaB})\,tD+\frac{1}{2}\left(\text{omegaA}\left(-\frac{2\,L1\,(v12Down+v12Up)}{v12Down\,v12Up}+DC\left(\frac{2}{v12Down}+\frac{2}{v12Up}-\frac{1}{v1Down}-\frac{1}{v1Up}+2\left(-\frac{1}{v2Down}-\frac{1}{v2Up}+\frac{1}{vDDown}+\frac{1}{vDUp}\right)\right)-\frac{2\,L2\,(vDDown+vDUp)}{vDDown\,vDUp}\right)+\text{omegaB}\left(DC\left(\frac{1}{v2Down}+\frac{1}{v2Up}-\frac{2}{vDDown}-\frac{2}{vDUp}\right)+\frac{2\,L2\,(vDDown+vDUp)}{vDDown\,vDUp}\right)\right)$$

Non time−dependent phase must cancel. Solving the equation yields the MIEZE condition.

```
In[43]:= FullSimplify[
          Solve[1/2 (omegaA (-(2 L1 (v12Down + v12Up))/(v12Down v12Up) + DC (2/v12Down + 2/v12Up - 1/v1Down - 1/v1Up +
                2 (-1/v2Down - 1/v2Up + 1/vDDown + 1/vDUp)) - (2 L2 (vDDown + vDUp))/(vDDown vDUp)) +
            omegaB (DC (1/v2Down + 1/v2Up - 2/vDDown - 2/vDUp) + (2 L2 (vDDown + vDUp))/(vDDown vDUp)) == 0, L1]]
```

$$\text{Out[43]= } \left\{\left\{L1\to-\left(v12Down\,v12Up\left(\frac{1}{2}DC\left(\text{omegaA}\left(-\frac{2}{v12Down}-\frac{2}{v12Up}+\frac{1}{v1Down}+\frac{1}{v1Up}+2\left(\frac{1}{v2Down}+\frac{1}{v2Up}-\frac{1}{vDDown}-\frac{1}{vDUp}\right)\right)+\text{omegaB}\left(-\frac{1}{v2Down}-\frac{1}{v2Up}+2\left(\frac{1}{vDDown}+\frac{1}{vDUp}\right)\right)\right)+\frac{L2\,(\text{omegaA}-\text{omegaB})\,(vDDown+vDUp)}{vDDown\,vDUp}\right)\Big/(\text{omegaA}\,(v12Down+v12Up))\right)\right\}\right\}$$

After replacing velocities (square−root approximation)

```
In[52]:= FullSimplify[
           Solve[1/2 (omegaA (-(2 L1 (v12Down + v12Up))/(v12Down v12Up) + DC (2/v12Down + 2/v12Up - 1/v1Down - 1/v1Up +
                 2 (-1/v2Down - 1/v2Up + 1/vDDown + 1/vDUp)) - (2 L2 (vDDown + vDUp))/(vDDown vDUp)) +
             omegaB (DC (1/v2Down + 1/v2Up - 2/vDDown - 2/vDUp) + (2 L2 (vDDown + vDUp))/(vDDown vDUp))) == 0, L1]]
```

$$\text{Out[52]}= \left\{\left\{L1 \to \frac{1}{2}\left(\frac{2\,DC\,(8\,omega0^2+omegaA^2)}{16\,omega0^2-omegaA^2}+\frac{2\,DC\,(-2\,omega0+omegaA)\,(2\,omega0+omegaA)}{omegaA\,(-4\,omega0-2\,omegaA+omegaB)}+\right.\right.$$
$$\frac{2\,DC\,(-4\,omega0^2+omegaA^2)}{omegaA\,(4\,omega0-2\,omegaA+omegaB)}+$$
$$\frac{(DC-L2)\,(2\,omega0-omegaA)\,(2\,omega0+omegaA)}{omegaA\,(-2\,omega0-omegaA+omegaB)}+$$
$$\left.\left.\left.\frac{(DC-L2)\,(2\,omega0-omegaA)\,(2\,omega0+omegaA)}{omegaA\,(2\,omega0-omegaA+omegaB)}\right)\right\}\right\}$$

Sorting and rearranging terms ...

$$L1 == \frac{DC\left(\frac{1}{2}+\frac{omegaA^2}{16\,omega0^2}\right)}{1-\frac{omegaA^2}{16\,omega0^2}}+\frac{DC\left(1-\frac{omegaA^2}{4\,omega0^2}\right)(-2\,omegaA+omegaB)}{omegaA\left(2-\frac{(-2\,omegaA+omegaB)^2}{8\,omega0^2}\right)}+$$
$$\frac{(-DC+L2)\left(1-\frac{omegaA^2}{4\,omega0^2}\right)(-omegaA+omegaB)}{omegaA\left(1-\frac{(-omegaA+omegaB)^2}{4\,omega0^2}\right)}$$

For the approximation of omega0 >> omegaA,B we obtain the classical MIEZE condition

$$L1 == FullSimplify\left[Limit\left[\frac{DC\left(\frac{1}{2}+\frac{omegaA^2}{16\,omega0^2}\right)}{1-\frac{omegaA^2}{16\,omega0^2}}+\frac{DC\left(1-\frac{omegaA^2}{4\,omega0^2}\right)(-2\,omegaA+omegaB)}{omegaA\left(2-\frac{(-2\,omegaA+omegaB)^2}{8\,omega0^2}\right)}+\right.\right.$$
$$\left.\left.\frac{(-DC+L2)\left(1-\frac{omegaA^2}{4\,omega0^2}\right)(-omegaA+omegaB)}{omegaA\left(1-\frac{(-omegaA+omegaB)^2}{4\,omega0^2}\right)},\ omega0 \to Infinity\right]\right]$$

$$\text{Out[41]}= L1 == \frac{(DC-2\,L2)\,(omegaA-omegaB)}{2\,omegaA}$$

Rearranging the terms yields the expression from Eq. (1.156)

$$\frac{L1}{L2-DC/2} == \frac{omegaB}{omegaA}-1$$

A.3 Circuit Diagram MIRA C-Box

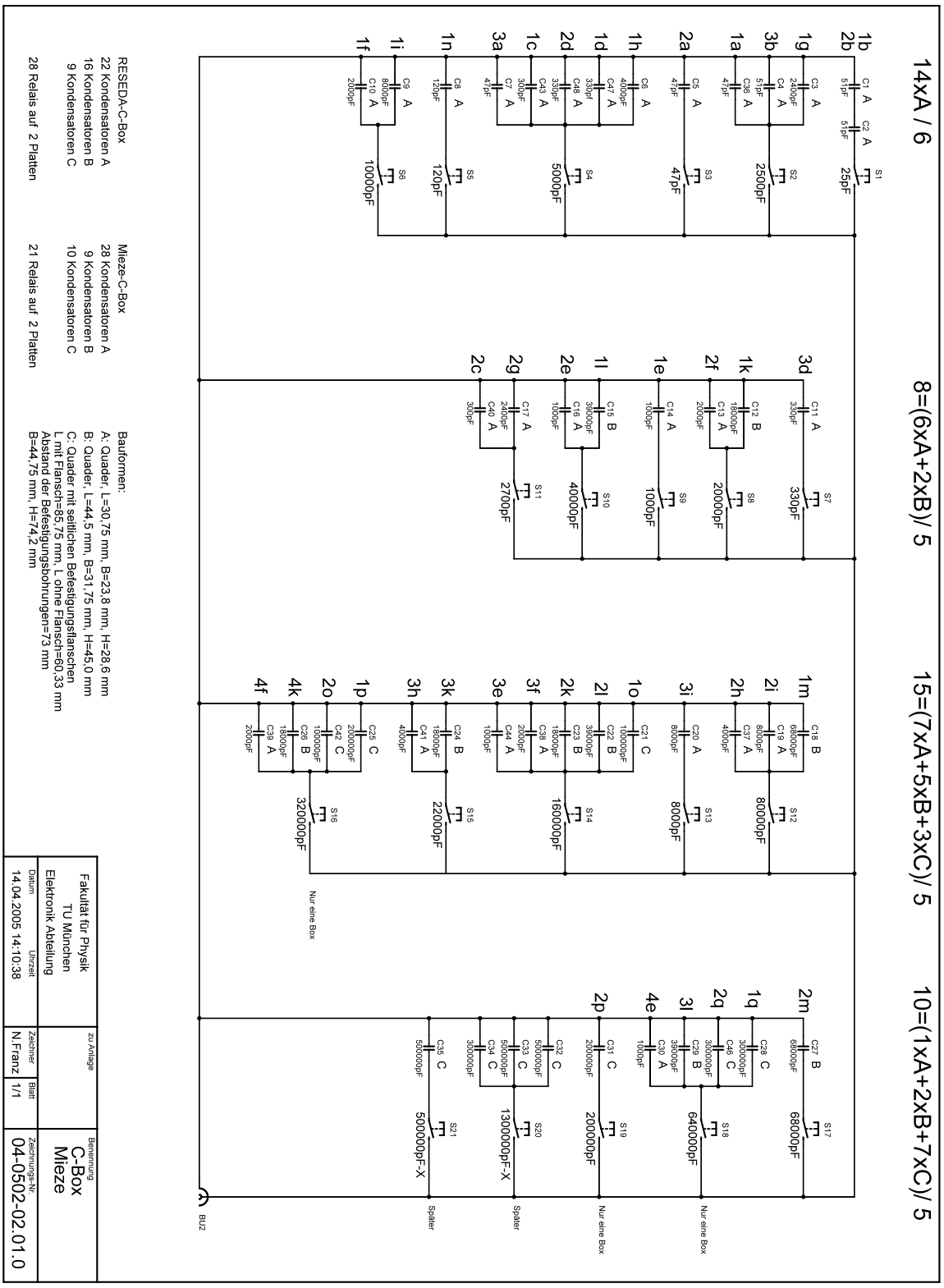

Figure A.1: Circuit diagram of the capacitor wiring in the MIRA C-Boxes. The capacitors are connected in parallel to each other, the RF coils in series to the capacitors.

A.4 Fitting Results MIEZE Measurements

Like for the Multi-MIEZE data, the non-linear fitting for both single MIEZE signals and the detuned Multi-MIEZE signal was done using a scaled Levenberg-Marquardt algorithm without weighting and a tolerance of 10^{-4}. The following table shows the results for the fitting parameters.

Parameter	Fit results		
	MIEZE 1	MIEZE 2	detuned Multi-MIEZE
I_0	39512.1 ± 0.5	40162.3 ± 0.5	78498.7 ± 1.0
C_1	$0.51521 \pm 2 \cdot 10^{-5}$	$0.30362 \pm 2 \cdot 10^{-5}$	$0.51516 \pm 3 \cdot 10^{-5}$
C_2	–	–	$0.30655 \pm 2 \cdot 10^{-5}$
φ_1 [rad]	$2.83347 \pm 3 \cdot 10^{-5}$	$-0.58454 \pm 6 \cdot 10^{-5}$	$2.82407 \pm 3 \cdot 10^{-5}$
φ_2 [rad]	–	–	$2.70762 \pm 6 \cdot 10^{-5}$
R^2	0.999299	0.9963	0.99662
χ^2/doF	44731.4	84968.5	275832

Table A.2: Fitting model parameters and results of the single MIEZE and the detuned Multi-MIEZE data.

Bibliography

[1] F. Mezei. *Z. Phys.*, 255:146, 1972.

[2] R. Gähler and R. Golub. A high resolution neutron spectrometer for quasielastic scattering on the basis of spin-echo and magnetic resonance. *Z. Phys. B - Cond. Matt.*, 65:269–273, 1987.

[3] Thomas Keller, Robert Golub, and Roland Gähler. Neutron spin echo - a technique for high-resolution neutron scattering. In Roy Pike and Pierre Sabatier, editors, *Scattering and Inverse Scattering in Pure and Applied Science*, pages 1264–86. Academic Press, San Diego, CA, 2002.

[4] T. Keller. *Höchstauflösende Neutronenspektrometer auf der Basis von Spinflippern - neue Varianten des Spinecho-Prinzips*. PhD thesis, Fakultät für Physik der Technischen Universität München, Germany, July 1993.

[5] M. C. Köppe. *Aufbau des Hochfrequenz-Spinechos von Saclay und erste Messungen an den Glasbildnern Glyzerin und Kalzium-Rubidium-Nitrat*. PhD thesis, Fakultät für Physik der Technischen Universität München, Germany, July 1998.

[6] P. Hank. *Aufbau des Neutronenresonanz-Spinechospektrometers in Saclay und Erweiterung der Meѕmöglichkeiten durch die MIEZE-Option*. PhD thesis, Fakultät für Physik der Technischen Universität München, Germany, March 1999.

[7] Otto Schärpf. Polarization Elements. In Thomas Brückel and Werner Schweika, editors, *Polarized Neutron Scattering*, volume 12 of *Schriften des Forschungszentrums Jülich, Reihe Materie und Material/Matter and Materials*, chapter 2. Forschungszentrum Jülich GmbH Institut für Festkörperforschung, 2002.

[8] F. Schwabl. *Quantenmechanik für Fortgeschrittene*. Springer, 1997.

[9] W. Nolting. *Quantenmechanik, Teil 1: Grundlagen*, volume 5 of *Grundkurs: Theoretische Physik*. Zimmermann-Neufang, 3rd edition, 1992.

[10] W. Nolting. *Quantenmechanik, Teil 2: Methoden und Anwendungen*, volume 5 of *Grundkurs: Theoretische Physik*. Zimmermann-Neufang, 3rd edition, 1993.

[11] U. Schmidt. *Experimente mit polarisierten Neutronen zu Fragen der höchstauflösenden Spektrometrie und Quantenoptik*. PhD thesis, Fakultät für Physik der Technischen Universität München, Germany, February 1995.

[12] W. Häußler. *Weiterentwicklung, Aufbau und Test eines Resonanzspinecho-Spektrometers zum Einsatz eines Multidetektors*. PhD thesis, Naturwissenschaftlich-Mathematische Gesamtfakultät der Ruprecht-Karls-Universität Heidelberg, Germany, April 1998.

[13] R. Golub, R. Gähler, and T. Keller. A plane wave approach to particle beam magnetic resonance. *Am. J. Phys.*, 62:779–87, 1994.

[14] F. Mezei. Zeeman energy, interference and neutron spin echo: A minimal theory. *Physica B*, 151:74–81, 1988.

[15] J. Felber, R. Gähler, R. Golub, P. Hank, V. Ignatovich, T. Keller, and U. Rauch. Neutron Time Interferometry. *Foundations of Physics*, 29(3):381–396, 1999.

[16] E. Krüger. Acceleration of polarized neutrons by rotating magnetic fields. *Nukleonika*, 25:889–893, 1980.

[17] R. Gähler, R. Golub, and T. Keller. Neutron resonance spin echo – a new tool for high resolution spectroscopy. *Physica B*, 180 & 181:899–902, 1992.

[18] H. Rauch and S. A. Werner. *Neutron Interferometry*. Oxford series on neutron scattering in condensed matter. Oxford University Press, 2000.

[19] M. Born and E. Wolf. *Principles of Optics*. Pergamon, Oxford, 6th edition, 1980.

[20] A. G. Klein, G. I. Opat, and W. A. Hamilton. Longitudinal Coherence in Neutron Interferometry. *Phys. Rev. Letters*, 50(8):563–565, 1983.

[21] S. Prokudaylo, R. Gähler, T. Keller, M. Bleuel, M. Axtner, and A. Selvachev. Calculations on resonance spin-echo coils. *Applied Physics A*, 74 [Suppl.]:S317–S319, 2002.

[22] http://wwwnew.frm2.tum.de/en/science/instruments/spectrometers/reseda.html.

[23] http://www.fkf.mpg.de/keimer/Research/Spectroscopic_methods/Spin-echo/Spin-echo.html.

[24] M. Wahl. Aufbau einer Messanordnung zur Neutronenreflektometrie. Master's thesis, Max-Planck-Institut für Metallforschung, Stuttgart, Germany/Institut für Theoretische und Angewandte Physik, Universität Stuttgart, Germany, February 2003.

[25] *Neutron News*, 3(3):29–37, 1992.

[26] Alexander Ioffe. Private communication.

[27] http://www.integratedsoft.com/products/faraday/.

[28] D. Zheng. Three-dimensional eddy current analysis by the boundary element method. *IEEE Transactions on Magnetics*, 33(2, Part 2):1354–1357, March 1997.

[29] S. Prokudaylo. *Calculations for neutron spin echo*. PhD thesis, Fakultät für Physik der Technischen Universität München, Germany, September 2004.

[30] M. Bleuel. *Aufbau des Neutronen-Resonanz-Spinecho-Spektrometers RESEDA am FRM-II*. PhD thesis, Fakultät für Physik der Technischen Universität München, Germany, February 2003.

[31] *Neutron News*, 17(1):12, 2006.

[32] B. M. Märkisch. Studies on CASCADE Detector Prototypes and Development of its Infrastructure. Master's thesis, Faculty of Physics and Astronomy University of Heidelberg, Germany, 2002.

[33] N. Arend, R. Gähler, T. Keller, R. Georgii, T. Hils, and P. Böni. Classical and quantum-mechanical picture of NRSE - measuring the longitudinal Stern-Gerlach effect by means of TOF methods. *Physics Letters A*, 327/1:21–27, 2004.

[34] R. Gähler, R. Golub, K. Habicht, T. Keller, and J. Felber. Space-time description of neutron spin echo spectrometry. *Physica B*, 229:1–17, 1996.

[35] A. I. Okorokov, S. V. Grigoriev, Yu. O. Chetverikov, R. Georgii, P. Böni, H. Eckerlebe, K. Pranzas, and B. Roessli. The spin chirality in MnSi single crystal probed by small angle scattering with polarized neutrons. *Physica B*, 350:e323–e326, 2004.

[36] A. I. Okorokov, S. V. Grigoriev, Yu. O. Chetverikov, S. V. Maleyev, R. Georgii, P. Böni, D. Lamago, H. Eckerlebe, and K. Pranzas. The effect of the magnetic field on the spiral spin structure in MnSi studied by polarized SANS. *Physica B*, 356:259–263, 2005.

[37] R. Georgii, P. Böni, D. Lamago, S. Stüber, S. V. Grigoriev, S. V. Maleyev, A. I. Okorokov, H. Eckerlebe, P. K. Pranzas, B. Roessli, and W. E. Fischer. Critical small-angle scattering of polarised neutrons in MnSi. *Physica B*, 350:45–47, 2004.

[38] E. M. Forgan, P. G. Kealey, S. T. Johnson, A. Pautrat, Ch. Simon, S. L. Lee, C. M. Aegerter, R. Cubitt, B. Farago, and P. Schleger. Measurement of Vortex Motion in a Type-II Superconductor: A Novel Use of the Neutron Spin-Echo Technique. *Phys. Rev. Letters*, 85(16):3488–3491, 2004.

[39] F. Mezei, editor. *Neutron Spin Echo, Proceedings Grenoble 1979*, volume 128 of *Lecture Notes in Physics*. Springer, 1980.

[40] W. Häußler, U. Schmidt, and D. Dubbers. Increased solid angle in neutron resonance spin echo. *Physica B*, 350:e799–e802, 2004.

[41] W. Häußler, B. Gohla-Neudecker, R. Schwikowski, D. Streibl, and P. Böni. RESEDA - the new Resonance Spin Echo Spectrometer using cold neutrons at the FRM-II. *Physica B*, doi:10.1016/j.physb.2007.02.086, 2007.

[42] M. Bleuel, K. Littrell, R. Gähler, and J. Lal. MISANS, a method for quasi-elastic small angle neutron scattering experiments. *Physica B*, 356(1-4):213–217, 2005.

[43] M. Bleuel, L. B. Lurio, K. Littrell, R. Gähler, and J. Lal. Complementarity of MIEZE-SANS and X-ray photon correlation spectroscopy (XPCS). *Physica B*, 3(1-4):223–228, February 2005.

[44] R. Golub, R. Gähler, K. Habicht, and S. Klimko. Bunching of continuous neutron beams. *Physics Letters A*, 349:59–66, 2006.

[45] Roland Gähler. Private communication.

Acknowledgment

The preparation of this thesis and the realization of the projects involved depended on many people and facilities, and I can only hope to not forget any of them here. If I do, please be forgiving.

First of all I'd like to thank Prof. Dr. Peter Böni and Dr. habil. Roland Gähler, my supervisor and scientific tutor, respectively. Peter allowed me to do my PhD at his institute and always supported my ambitions. He gave me the freedom to try and realize my approaches and ideas, and I much appreciate his valuable input. Working in the field of resonance spin echo, there is hardly a source of greater expertise than Roland. I thank them for their patience and support.

Dr. Robert Georgii, the MIRA instrument responsible, was my direct supervisor at the instrument. I'd like to thank him very much for the practical support, his flexibility, the continual encouragement and his personal interest in the progress of my work.

Special thanks go to Dr. Thomas Keller and in particular Dr. Wolfgang Häußler, the resonance spin echo go-to guys here at the FRM-II, for sharing their knowledge. Wolfgang was more than a colleague to me and, although under no obligation, guided me through this PhD in many respects. His enormous experience in N(R)SE, theoretically and technical-wise, has helped this work and our cooperation so much.

For the large number of components that had to be built, assembled, and installed I could rely on skilled people and facilities. A big thank-you therefore to Guido Langenstück, Heinz Wagensonner, and especially Reinhard Schwikowski and Andreas Mantwill, the former and current MIRA/RESEDA engineers, technicians, and mechanics. Their personal commitment exceeded the normal by far. The technical facilities and workshops at the FRM-II, the central workshop under the direction of Manfred Pfaller, and the electronics lab of the Physics Department usually delivered first class quality. A big thank-you to Jörg Pulz and the FRM-II computer department for the good collaboration and their quick and competent response to any of my requests.

Markus Axtner I have to thank for the huge personal effort he put into the production of the B_0 coil sheets. Among our numerous student trainees, I'd like to distinguish Markus Bröll and Arne Laucht, who were mostly concerned with field simulations. Arne's conscientious and independent way of working was very supportive.

Furthermore, I'd like to express my gratitude to all members of the institute E21 and especially to my fellow PhD students for making my time there a really enjoyable one. I am much obliged to Sebastian Mühlbauer for his moral and practical backup when it was crunch-time during measurements.

Dr. Alexander Ioffe I'd like to thank for inspiring discussions about physics, life, and what both have to do with each other.

A maybe unusual but nonetheless sincere thank-you goes to the Linux and open-source software community. Many people there spend their time and skills to produce excellent software we rely on in science every day.

The PhD work was kindly supported by the EU FP6 project under contract number HII3-CT-2003-505925, project JRA5/PNT.

Last not least I owe so much to my friends, my parents, and my own family. Their support, not only but most importantly as a constant motivation, has helped me over dry spells more than once.

This work is dedicated to Tamara and Linus. You're the light of my life.